공학박사 학위논문

Structural Evolution of Block Copolymer Micelles and Micelle-Inorganic Hybrids

블록공중합체 마이셀과 마이셀-무기 조합체의 구조 및 그 변화

2020 년 7 월

서울대학교 대학원

화학생물공학부

김 세 영

Structural Evolution of Block Copolymer Micelles and Micelle-Inorganic Hybrids

블록공중합체 마이셀과 마이셀-무기 조합체의 구조 및 그 변화

지도교수 차 국 헌

이 논문을 공학박사 학위논문으로 제출함

2019 년 12 월

서울대학교 대학원
화학생물공학부
김 세 영

김세영의 박사학위논문을 인준함
2020 년 1 월

위 원 장 _____ (인)

부 위 원 장 _____ (인)

위 원 _____ (인)

위 원 _____ (인)

위 원 _____ (인)

Abstract

Structural Evolution of Block Copolymer Micelles and Micelle-Inorganic Hybrids

Seyoung Kim

School of Chemical & Biological Engineering

The Graduate School

Seoul National University

Self-assembly of block copolymer micelles (BCMs) in selective solvents is well-understood phenomenon after decades of fundamental researches, and yet recent studies with novel block copolymer designs have demonstrated structural and dynamic behaviors of BCMs beyond the classical understanding. Simultaneously, strategies that use BCMs as building blocks for hybrid structures or nanocomposites has received great attention in a couple of decades for the purpose of extraordinary material properties, mimicking the protein-inorganic hybrids ubiquitous in nature. Therefore, it is essential to make

connections between the fundamentals of BCM assembly and the design principles of hybrid structures involving BCMs. This dissertation addresses impact of a distinct molecular motif at block copolymers on the structures and dynamics of self-assembled micelles and an illustrative hybrid structure made from the interactions between BCMs and inorganic materials. The underlying theme across the studies is to emphasize the importance of knowledge on the structural evolution of BCMs in making precisely engineered nanomaterials.

The first part of this dissertation presents characterization and interpretation of the micellar structures and the relaxation dynamics using diblock copolymers where long fluoroalkyl side-chains are attached to a specific block. The "bottlebrush" chain architecture causes large stiffness on the fluoroalkyl block, forcing it to be strongly stretched within the core of spherical micelles in a solvent selective to the non-fluoroalkyl block. Unconventional scaling relationships between sizes of the core and the corona and the length of fluoroalkyl block are found, suggesting that this notable stiffness of the core block induces deviation from the classical thermodynamic theory of BCMs. Another consequence of the bottlebrush architecture is the absence of entanglement and the abundance of free volume within the core domain, which facilitates the internal relaxation of chain within the core. As a result, equilibration of the model diblock copolymer is substantially fast, which leads to the rapid preparation of highly monodispersed BCMs. A quantitative measurement of the relaxation kinetics was made using contrast matched small-angle neutron scattering technique, which proves fast chain exchange between

BCMs with bottlebrush core block. Hence, the impact of bottlebrush architecture at the core block is found to be significant in that the dependence of BCM structures on its length and the relaxation kinetics are quite different from those of linear, flexible block copolymers.

The second part presents hybrid structures involving BCMs, namely, bio-mimicking nanocomposite of BCMs and mineral crystals. Herein, BCMs are allowed to adsorb at the surface of inorganic materials via electrostatic interaction. Such adsorption brings about the occlusion of BCMs in growing mineral crystals, where the occlusion density appears to be important in determining resultant toughening effect of the occluded minerals. Charge density of the corona affects the strength of the BCM adsorption at the mineral surface, whereas Brownian diffusion of BCMs affects the collision frequency at the growing mineral crystals. Thus, by controlling pH and hydrodynamic size of BCMs, the crystals experience from unperturbed growth to partial blockage of growing site (occlusion) to adsorption-induced growth inhibition in the order of increasing adsorption density. These results indicate that BCMs with precisely controlled structure could serve as versatile building blocks for hierarchical nanostructures with unprecedented mechanical properties.

Keywords : Block copolymer micelles • Chain architecture • Relaxation kinetics • Micelle adsorption • Micelle-inorganic hybrids

Student Number : 2014-21582

Contents

List of Tables

List of Figures

Chapter 1. Introduction

1.1. Historical Background

Self-assembly of macromolecules is the supreme strategy that life has developed over billions of years of evolution to build its form, run its metabolic cycles, and survive harsh environments. At the heart of such creativity and complexity of biological functions lies deliberately sequenced chains of amino acids, i.e., proteins. Progresses in modern science discovered that these proteins fold themselves in multi-dimensional structures and further self-organize, sometimes incorporating inorganic elements, into distinct structures with desired properties on life's demand. The lessons from nature have driven polymer scientists towards studying the principles of self-assembly and making self-assembled materials for various purposes starting from synthetic polymers with designed sequences.[1]

Block copolymers (BCPs) are polymers that consist of linearly linked sub-chains (i.e., blocks) with distinct repeat units, thus holding minimal concept of the sequential design. BCPs spontaneously build patterns dictated by its sequence and the lengths of individual blocks, where the interactions between unlike repeat units drive such self-assembly. For example, diblock copolymers, of the simplest sequence, can self-assemble into spherical, cylindrical, or planar domains depending on their composition, which further lead to patterns such as the body-centered cubic, hexagonal, or lamellar.[2] Such versatility of self-assembly is even intensified when solvent molecules are included in the system.

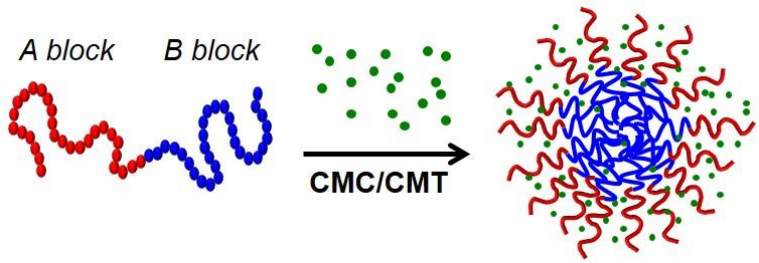

Figure 1.1. Association of A-B diblock copolymers in A-selective solvent into self-assembled micelles. Such micellization occurs at the concentration greater than the critical micelle concentration (CMC) and/or at the temperature lower/higher than the critical micelle temperature (CMT).

The interactions between solvent and blocks interfere in the statistical conformation of each block and the curvature of the interface. Even though BCPs are rather (over-)simplified version of the sequenced chains, the interplay of mutual interactions and its effect on how the self-assembled structures evolve in BCP solutions have profound meanings for understanding what happens in real nature.

A short summary is made to sketch out how self-assembly of BCPs determines the structure of spherical micelles and other forms of the aggregates. The insoluble block segregates from the solvent when dissolved, forming the "core" domain, and the soluble blocks are tethered at its interface, hence forming the outer "corona" domain surrounding the core (Figure 1.1). From the thermodynamic perspective, the resulting structure is an outcome of counterbalancing between the interfacial energy, the elastic energies

accompanied with the stretching of core and corona blocks, and the excluded volume interactions for corona block (especially in good solvent).[3] When the corona block is sufficiently longer than the core block, the thermodynamics is dominated by the elastic energy and/or excluded volume interactions for corona block. Thus, self-assembled aggregates morph into spheres with large interfacial curvature and thick corona (the "hairy" micelles), which is favored due to lower free energy of corona block. In contrast, when the corona block is sufficiently shorter than the core block, the thermodynamics is dominated by the interfacial energy and the elastic energy for core block. Then, aggregates morph into spheres with small interfacial curvature and thin corona (the "crew-cut" micelles) which are favored due to lower interfacial energy or even different geometries (e.g., the "worm-like" aggregates and vesicles) due to lower elastic energy of corona block.

Such richness of structural degree of freedom in BCP assemblies associated with system parameters (e.g., block copolymer and solvent properties) has motivated fundamental studies on the self-assembly of block copolymers for decades, which now enabled quite accurate description and/or prediction of aggregate structures and dynamics in given systems.[4] The structural properties of block copolymer micelles at equilibrium can be predicted by minimization of the total free energy of a given system. Many approaches have been suggested to develop expressions for the free energy of micellar system and optimize the system within vast parameter space. Among these, scaling approach has become the most straightforward way to assess trends of the structural properties with respect to the numbers of repeat units of the core and corona block (N_{core} and N_{corona}, respectively), by taking simplicity at the cost of numerical accuracy.

The first successful scaling prediction was made by de Gennes for the limiting case of crew-cut micelles,[5] where the contributions from corona block can be neglected. Also, strong segregation of the core block is assumed, i.e., the solvent is impenetrable to the core domain. Here, the free energy per chain F_{chain} is represented as a sum of the interfacial energy F_{int} and the elastic free energy of core block F_{core},

$$F_{chain} \simeq F_{int} + F_{core} \quad (1.1),$$

where

$$F_{int} = \gamma s \sim \gamma p^{-1/3}(N_{core}a^3)^{2/3} \quad (1.2)$$

$$F_{core}/k_BT \sim R_{core}^2/N_{core}a^2 \sim p^{2/3}N_{core}^{-1/3} \quad (1.3),$$

and γ is the interfacial tension of the core-corona interface, s the area per chain, p the aggregation number, a the size of repeat unit, k_B the Boltzmann constant, T the temperature, R_{core} the core radius. Numerical factors are omitted. The only adjustable parameter is p, thus minimizing F_{chain} with respect to p results in $p \sim \gamma N_{core}a^2/k_BT$. The scaling law for the size of micelles follows that $R_{core} \sim \gamma^{1/3}N_{core}^{2/3}$. The exponent of 2/3 appeared to be in good agreement with experiments using block copolymers with short corona block (hence, crew-cut micelles are formed), however, as the length of corona block increases relative to the core block, the neglect of contributions from the corona block becomes detrimental.

On the other hand, scaling approach for the limiting case of hairy micelles was initiated by Daoud and Cotton using the concept of correlation blob to exclusively consider the free energy of corona block F_{corona}.[6] The interaction free energy $\simeq k_BT$ is accumulated for each correlation blob with size ξ since the conformation of chain deviates from being unperturbed at length scales larger than ξ, triggered by either dense packing of the corona chains and/or the excluded volume effect. The spherical geometry demands that $\xi(r)$ expands

with distance r from the center of micelle as $\xi(r) \sim r^{-1/2}$, and through the mass conservation condition of polymer chains in the corona domain, the resulting corona thickness L_{corona} is scaled as $L_{corona} \sim N_{corona}^{\nu}$, where ν is the Flory exponent for the corona block. Extending the theory of Daoud and Cotton, Halperin suggested the scaling law for core radius, $R_{core} \sim N_{corona}^{-4/25} N_{core}^{3/5}$.[7] Again, the exponent of 3/5 agrees well with experiments using block copolymers with long corona block, which form hairy micelles.

Despite the success of such scaling laws in predicting the experiments performed at either crew-cut or hairy regime, both lack qualitative accuracy at the crossover regime where many of the practical block copolymer systems reside. Therefore, many attempts were made to improve the quality of prediction by taking all contributions (F_{int}, F_{core}, and F_{corona}) into consideration. For example, Zhulina and Borisov numerically solved the fully equipped equation and correctly recovered behavior of block copolymers at the crossover regime as well as the stability limit of different morphologies.[8] Nagarajan and Ganesh even extended the framework of free energy by incorporating the solubilization effect of polymer chains into solvent and succeeded in obtaining the structural properties of micelles by multivariable minimization with respect to explicit parameters.[9]

However, it has been found that the behavior of block copolymer micelles (BCMs) can significantly deviate from that of classical theories if the stiffness of chain backbone or the interfacial constraints at the core-corona interface are altered from ordinary situations. Recent advances in polymer chemistry enabled diverse strategies to induce such changes via incorporation of some novel structural or chemical motifs into BCPs, which opened new opportunities to explore the relationship between the modification of BCPs and the resulting self-assembled structures.

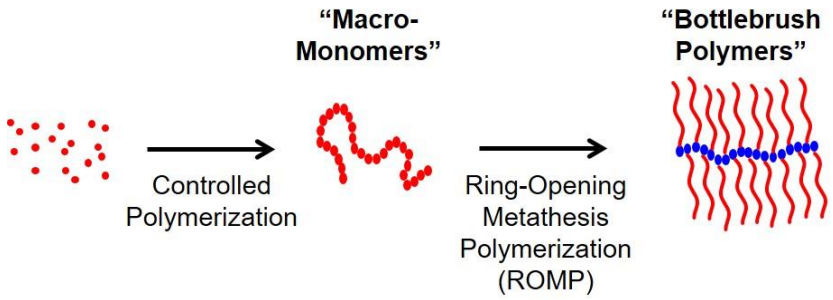

Figure 1.2. Bottlebrush polymers synthesized through sequential polymerizations via macromonomers.

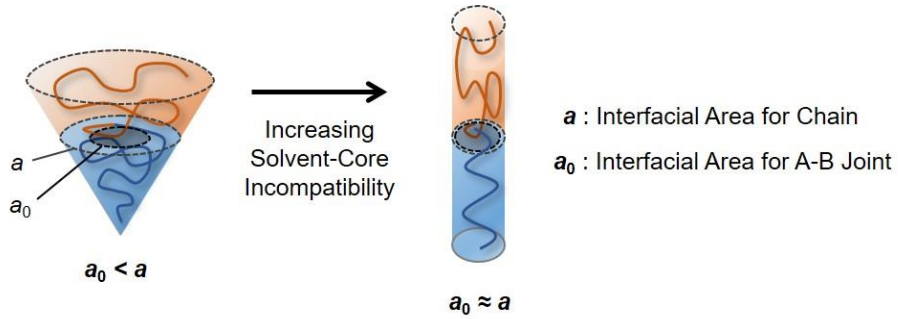

Figure 1.3. Deformation of the packing geometry of block copolymer micelles induced by super-strong stretching of the core block (blue) under extreme incompatibility between the core block and the solvent.

For instance, developments in ring-opening metathesis polymerization (ROMP) promoted synthesis of "bottlebrush" polymers and BCPs, which consist of repeat units with a polymeric side-chain (Figure 1.2).[10] Due to their inherent strong excluded volume interactions between adjacent repeat units, the backbone of bottlebrush polymer is a lot stiffer than linear polymers. On the other hand, studies on fluorinated BCPs have found that they are capable of forming unconventional flattened micelles as a result of the super-strong segregation,[11, 12] that is, the overcrowding of BCP joints at the interface triggered by huge incompatibility between the fluorinated block and the solvent (Figure 1.3).

Furthermore, BCMs can participate as building blocks in making hybrid structures or nanocomposites with different types of materials by the adsorption of the BCMs at the surface of exterior objects. In a similar way that proteins incorporate inorganic elements to construct natural nanocomposites with emergent mechanical or optical properties, BCMs can behave as functional components controlling the arrangement, the order formation, and the growth kinetics of inorganic particles, which leads to unprecedented material characteristics.[13] There are numerous examples demonstrating how diverse BCMs can interact with inorganic materials (Figure 1.4). For example, BCMs can incorporate silica nanoparticles (NPs) of sizes smaller than the core and act as structural template, leading to the ordering of silica NPs.[14] However, the reverse also can happen, where BCMs are incorporated in the inorganic domains mimicking bone structure, a collagen-hydroxyapatite composite, for the purpose of enhancing fracture hardness.[15]

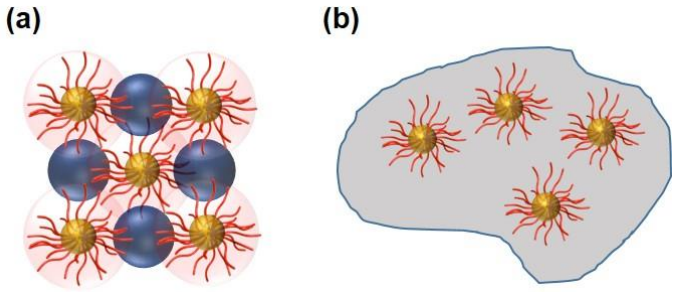

Figure 1.4. Design of hybrid materials from block copolymer micelles and inorganic phases. (a) Structurally controlled association through interactions between micelles and inorganic nanoparticles. (b) Incorporation of micelles in in mineral phases (occlusion).

1.2. Motivation of Research

Given this background, there is ultimate importance in making connections between the fundamentals of BCM formation and the design principles of hybrid structures involving BCMs. That is, a careful design of hybrids always requires precisely controlled, well-defined BCMs that serve as building blocks to fully realize its anticipated properties, while the structural control of BCMs calls for the knowledge over thermodynamics and kinetics of BCM formation with consideration of distinct features of the block copolymers in usage.

The first part of this dissertation (Chapters 2–3) deals with BCMs assembled from diblock copolymers with long fluoroalkyl side-chains attached to a specific block. The ROMP chemistry allowed convenient synthesis of such BCPs with the "bottlebrush" chain architecture, causing large stiffness and the abundance of free volume for the fluoroalkyl block. In chapter 2, a strong stretching of such fluoroalkyl block in the core as well as an unconventional scaling relationship between the core size and the length of fluoroalkyl block are investigated. In chapter 3, the chain dynamics of the fluoroalkyl block within the core and the relaxation kinetics of such BCMs are characterized. For both studies, small-angle X-ray and neutron scattering techniques provides rich information of the structure and dynamics, promoting quantitative analyses on the structural evolution of the fluoroalkyl BCMs.

The second part (Chapter 4) investigates nanocomposite of BCMs in CaSO4 mineral crystals as representative examples of BCM-inorganic hybrids. It is shown that BCMs interfere with growing $CaSO_4$ crystals via adsorption at the growth site of the crystals. There is dynamic competition between the crystal growth and the diffusion of adsorbing materials (i.e., diffusion-limited

adsorption), and formulation on the dynamical model leads to precise control of the occlusion density of BCMs and/or growth inhibition, which are accompanied by striking difference of the resultant crystal habit.

Chapter 2. Structures of Bottlebrush Fluoroalkyl Block Copolymer Micelles

2.1. Introduction

Self-assembly of block copolymers having bottlebrush architecture where a long, typically polymeric, side-chain is tethered to each repeat unit have drawn continuing interests because of its potential in achieving well-defined domains with extraordinary large spacing which is relevant to photonic applications.[16, 17] Owing to the strong steric or excluded volume interactions between adjacent side-chains, the backbone of bottlebrush polymers tend to be stiffer, which perturbs the chain conformation from being Gaussian.[18-20] Depending on the length and the grafting density of side-chains, bottlebrush polymers can possess a range of stiffness from virtually zero (e.g., flexible polymers) to infinite (e.g., rigid rod). In perspective of the block copolymer self-assembly, the stiffness of bottlebrush copolymers induces significant stretching inside the domain, which has been manifested in both experiments and theoretical works. For instances, it was shown that bottlebrush block copolymers have extraordinary strong dependence of the domain spacing (L) to the number of repeat units (N), $L \sim N^{0.9}$, whereas linear flexible block copolymers have yielded $L \sim N^{0.67}$.[21] Furthermore, a gradual increase of the side-chain grafting density could enhance chain stiffness, leading to increasingly stretched chains and therefore stronger power-law dependence of self-assembled domains ($L \sim N^{\alpha}$, $0.67 < \alpha < 1.0$).[22, 23]

An analogy can be set for bottlebrush block copolymers in selective solvents, where the chain stiffness of the insoluble block could bring expansion of the segregated core domain. Several works have already demonstrated that micelles assembled from bottlebrush block copolymers have elongated core dimensions,[24-26] including ones with fully stretched core block when the copolymers are densely grafted with long side-chains.[27-29] This intuitive behavior can also be rationalized by means of the free energy formalism. The stiffness of the core block reduces entropic elasticity, which can lead to pronounced expansion of the core without triggering morphological transition from sphere to other geometries.[8] However, there is still lack of systematic studies on the structures derived from bottlebrush block copolymers in solutions, thus, a comprehensive description of the effect of bottlebrush chain stiffness on the micelle structures still awaits to be conducted.

In the present study, we demonstrate spherical micelles self-assembled from bottlebrush-type block copolymers in a selective solvent at equilibrium (Fig. 2.1). Here the insoluble (core) block is grafted with $-C_8F_{17}$ fluoroalkyl side-chain, and we have assured that this side-chain is sufficiently long to impose a modest chain stiffness on the core block. Such block copolymers were prepared through highly controlled ring-opening metathesis polymerization (ROMP) and allowed to form micelles in tetrahydrofuran (THF). Using a series of block copolymers with different block lengths, we obtained various structural information of the micelles from small-angle X-ray scattering (SAXS) as well as complementary small-angle neutron scattering (SANS) and dynamic light scattering (DLS) experiments. It was found that spherical micelles with highly stretched core block were thermodynamically stable for all polymer samples. Also, the core radius and the corona thickness had stronger dependence on the core block length than any theoretical prediction constructed

for linear, flexible block copolymers, except ones at so-called super-strong segregation regime.[30] We present reasoning of such strong effects of the core block with a simple scaling model which permits the conformational stiffness as a variable. Unlike several scaling studies dealt with bottlebrush copolymers in bulk phases, this study is the first scaling analysis performed using bottlebrush-type copolymers in solution phase, which highlights the importance of core-block architecture on the structure of block copolymer micelles. As one can easily control the stiffness of bottlebrush polymers through the length and/or grafting density of the side-chains, this study may help extending structural degrees of freedom in solution-phase self-assembly using block copolymers.

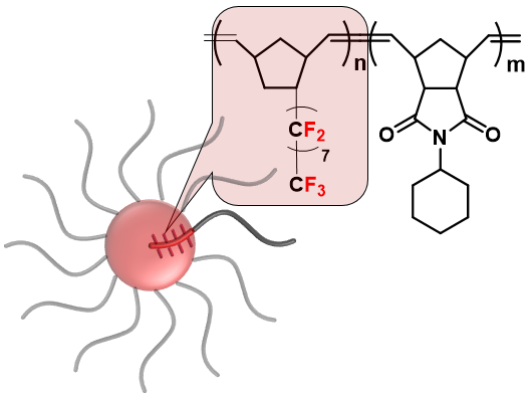

Figure 2.1. Molecular structure of the model polymer poly(5-perfluorooctyl norbornene)-block-poly(*N*-Cyclohexyl-exo-norbor-nene-5,6-dicarboxyimide) (PF_n-*b*-PC_m). PF block forms the core domain of spherical micelles in THF.

2.2. Experimental Section

Materials. Grubbs 3rd generation catalyst, N-Cyclohexyl-exo-norbornene-5,6-dicarboxyimide (ChNDI), and 5-(perfluorooctyl)norbornene (NB8F) were synthesized using previously established procedures.[1] Anhydrous dichloromethane (DCM) and *α,α,α*-trifluorotoluene (TFT) were purchased from Sigma-Aldrich and degassed through three freeze-pump-thaw cycles directly before use. All homopolymers and diblock copolymers pNB8F-*block*-pChNDI (hereafter noted as PF-*b*-PC) were prepared using previously reported ring-opening metathesis polymerization (ROMP) technique, with the exception of PF homopolymers of which polymerization reaction was carried out in TFT. Tetrahydrofuran (THF) was purchased from Sigma-Aldrich and used without further purification.

Characterization. The polymers were characterized by size exclusion chromatography (SEC), matrix-assisted laser desorption/ionization (MALDI), and elemental analysis (EA). Molecular weight and polydispersity (M_w/M_n) of PC homopolymers were estimated by SEC (YL9100 HPLC, YL Instrument) using THF as an eluent. Molecular weight and polydispersity of PF homopolymer with $N = 26$ were estimated by MALDI (Voyager DE-STR mass spectrometer, Applied Biosystems) using 2,5-dihydroxybenzoic acid (DHB) as a matrix substance. The complete conversion of ROMP for both kinds of homopolymers, as well as for the block copolymers, was confirmed by ^{1}H NMR spectroscopy. All PF-*b*-PC block copolymers were repeatedly precipitated in mixture of toluene and petroleum ether (3:1 by volume) and re-dissolved several times before characterization and sample preparation in order to eliminate small portions of "dead" PC homopolymers (at which the propagation of the PF block was not carried out) from the copolymers. After purification,

elemental weight fractions of carbon and hydrogen was measured for aliquots of PF-*b*-PC by EA (TruSpec Micro elemental analyzer, LECO), which were used for calculation of the molecular weights of PF block grown at the PC "mother" polymers with known molecular weights. Since the molecular weight distribution of PF-*b*-PC block copolymers could not be directly measured by either SEC or MALDI, hereafter we assumed that PF-*b*-PC has similar polydispersity (M_w/M_n) with those of PF (M_w/M_n = 1.05, from MALDI measurement; see Figure 2.2) or PC homopolymers (M_w/M_n = 1.05, from SEC measurement; see Figure 2.3) of which molecular weight distributions were very narrow.

Surface energy of PF was characterized by contact angle analysis. Silicon wafer substrates were sonicated in ethanol for 10 minutes, and glass substrates were cleaned by submerging in Piranha solution for 20 minutes prior to use. 5 w/v % solution of PF (N = 500) in TFT was spin coated at 3000 rpm for 60 seconds to render a PF film with flat surface on substrate and annealed overnight in vacuum oven. Sessile droplets of test liquids deionized water and diiodomethane (of which volumes were 5 and 2 μL, respectively) were carefully loaded on the annealed PF films, and the contact angles were measured using drop shape analyzer (DSA 100, Kruss). Polar and apolar surface energies of PF was calculated from measured contact angles using the method according to Wu *et al.*[2] Then, Hildebrand solubility parameter (δ) for PF was estimated using the surface energy values. Finally, Flory-Huggins interaction parameter between PF and THF was calculated using

$$\chi = 0.34 + \frac{v_0}{RT}(\delta_{\text{polymer}} - \delta_{\text{solvent}})^2 \tag{2.1}$$

where v_o is the reference volume and R is the ideal gas constant. The results are summarized in Table 2.1.

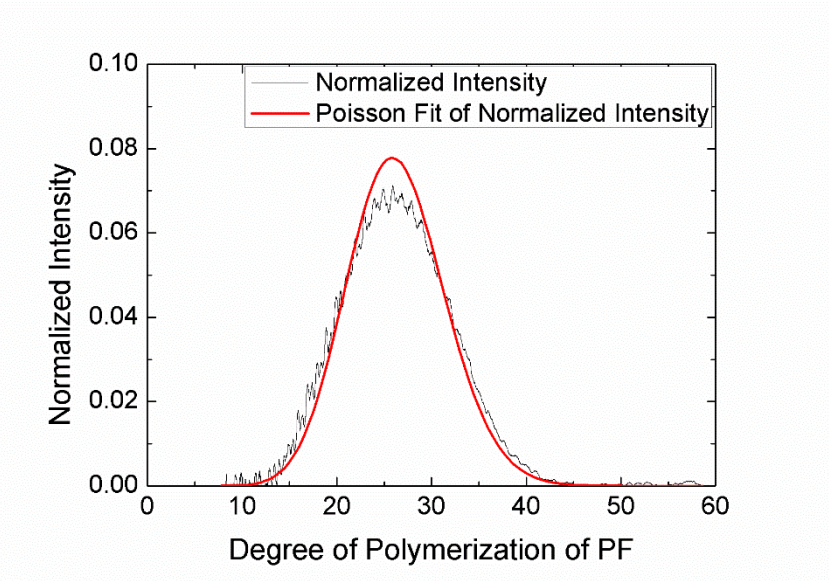

Figure 2.2. Chain length distribution of PF homopolymer ($DP_n = 26$) acquired from MALDI analysis. The line fit is according to the Poisson distribution with $M_w/M_n = 1.05$.

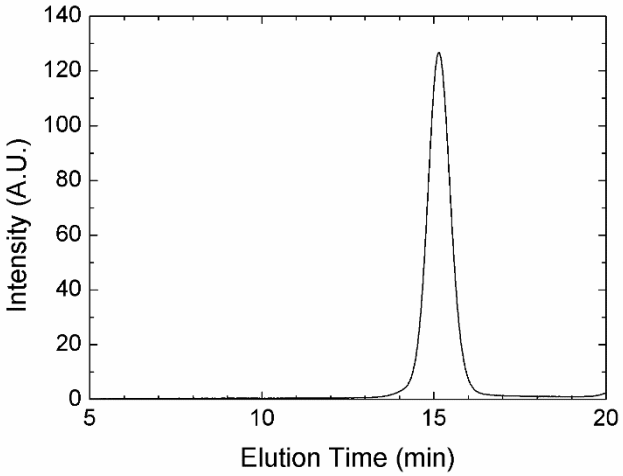

Figure 2.3. Chromatogram of PC homopolymer ($DP_n = 50$) acquired from GPC analysis, from which $M_w/M_n = 1.05$ is obtained.

Table 2.1. Thermodynamic parameters of PF homopolymer determined from contact angle analysis.

Contact Angle[a] [°]	
- Water	118.3
- Diiodomethane	91.3
Total Surface energy [mN/m]	16.6
- Non-polar surface energy	16.3
- Polar surface energy	0.3
Solubility Parameter[b] [$(J\ cm^3)^{0.5}$]	14.9
$\gamma_{PF\text{-}THF}$[c] [mN/m]	3.08
$\chi_{PF\text{-}THF}$ [-]	1.03

[a] Measured at 25 °C. [b] Reference 4. [c] Reference 2.

Small-Angle X-ray Scattering (SAXS). 1 wt% polymer solutions of PF-*b*-PC were prepared by dissolving the polymers in THF, which is a selective solvent for PC block. The polymer solutions were annealed for 24 hr at 60 °C in tightly sealed vials to bring the block copolymer micelles into the equilibrium state. The polymer solutions were then cooled down and syringe filtered before use. SAXS experiments were conducted using 9A beamline at Pohang Accelerator Laboratory (S. Korea). Radiation of 20 keV, corresponding to a wavelength λ = 0.620 Å, was selected from an undulator beam using a double-crystal monochromator, and the sample-to-detector distance (SDD) was 6.5 m. Samples were loaded in quartz capillaries and mounted in a thermostat stage at 25 °C, followed by X-ray exposure for 30 s. 2-D SAXS images were collected and azimuthally averaged using the data reduction software SAXSLee to provide one-dimensional plot of intensity I versus scattering wave vector magnitude $|q| = 4\pi\lambda^{-1} \sin(\theta/2)$, where θ is the scattering angle. The solvent

background was also collected and subtracted from the solution data. The resulting data were calibrated using a glassy carbon reference sample.

Dynamic Light Scattering (DLS). Samples with different concentrations (0.67–2.0 mg/mL) were prepared with the identical composition and procedure with those for SAXS experiments. DLS experiments were conducted using Zetasizer Nano ZS90 (Malvern Instruments). Scattering data with a wavelength λ = 532 nm and a scattering angle of 90^{o} was collected and the resulting time correlation functions were analyzed by the cumulant method.

Measurements of Neutron and X-ray Scattering Length Densities (SLDs) Using Small-Angle Neutron Scattering (SANS). Knowing neutron or X-ray SLDs (ρ_n and ρ_x, respectively) is necessary in any analysis for bi-component structures dispersed in the media. It is possible to calculate ρ_n or ρ_x for any materials when the gravimetric density (ρ_g) is known. Still, accurate determination of ρ_g for powdery or highly viscous polymer is not a trivial task, which is the case for our newly synthesized PF and PC polymers. Thus, we directly measured ρ_n of the materials using SANS with the solvent contrast variation method.

SANS experiments were performed at 40mSANS beamline at HANARO Facility, Korea Atomic Energy Research Institute (S. Korea) to estimate neutron and X-ray scattering length density (SLD) for individual PF and PF blocks. Samples of PC_{500} and PF_{180}-*b*-PC_{300} were examined at HANARO, where an instrument configuration with a wavelength λ = 6 Å, a wavelength spread ($\Delta\lambda/\lambda$) of 0.12, a SDD of 11.5 m was chosen. Samples were loaded in the 2 mm demountable cells and placed in a temperature-controlled heating block at 25 ^{o}C. Subsequently, scattering intensities were collected by a 2-D detector for 30 min. The 2-D scattering images were azimuthally averaged, reduced to an

absolute scale, and background subtracted using the package provided by HANARO based on IGOR Pro.

First, PC homopolymer (N = 500) was synthesized and diluted in mixture of (hydrogenated) h-toluene and (deuterated) d-toluene to yield 5 wt% solutions with 4 different solvent SLDs ($\rho_{n,s}$). The SLD of PC ($\rho_{n,PC}$) could be determined from the fact that the scattering intensity, $I(q)$, is proportional to $(\Delta\rho_{hPC})^2$ where q is the scattering vector and $\Delta\rho_i$ is the residual SLD for i-th phase ($\Delta\rho_i = \rho_{n,i} - \rho_{n,s}$). A linear plot of $[I_{q\to0}]^{1/2}$ vs $\rho_{n,s}$ was constructed to visualize the relationship where $I_{q\to0}$ is the scattering intensity at the limit of zero angle ($q \to 0$) (Figure 2.4.a). It is easily noticed that $\rho_{n,PC}$ should be same with $\rho_{n,s}$ at the x-intercept (i.e., $\Delta\rho_i = 0$).

Knowing $\rho_{n,PF}$ is trickier because PF homopolymer is not soluble in organic solvents with high hydrogen content (e.g., hexane, toluene), which does not allow simple solvent contrast variation experiment. Therefore, we instead used PF_{180}-*b*-PC_{300} block copolymers diluted in mixture of h-THF and d-THF to yield 1 wt% solutions with 5 different $\rho_{n,s}$. The scattering models for such micelles are discussed in detail in the following section. For the simplicity, only I_0 for different $\rho_{n,s}$ was evaluated and analyzed by the fact that

$$I_{q\to0} \sim (f_{PF}\,\Delta\rho_{PF} + f_{PC}\,\Delta\rho_{PC})^2 \qquad (2.2)$$

where f_i is the volume composition of i-th block in whole block copolymer Again, a linear plot of $[I_{q\to0}]^{1/2}$ vs $\rho_{n,s}$ was constructed (Figure 2.4.b). From the $\rho_{n,s}$ value at the x-intercept, $\rho_{n,PF}$ was determined by the following equation:

$$\rho_{n,PF} = f_{PF}^{-1}(\rho_{n,s} - f_{PC}\,\rho_{PC}). \qquad (2.3)$$

f_i was calculated from the knowledge of the number of repeat units and gravimetric density of each block. In fact, the analysis using eq. 2 retains some self-consistent fashion because only presumed $\rho_{n,PF}$ enables the calculation of $\rho_{g,PF}$ and f_{PF} further. Through such analysis, every information was obtained

Table 2.2. Neutron SLDs, X-ray SLDs, and gravimetric densities

Component	ρ_n [10^{-6} Å^{-2}]	ρ_x [10^{-6} Å^{-2}]	ρ_g [g/ml]
PF	3.24	14.2	1.70
PC	1.61	12.1	1.32

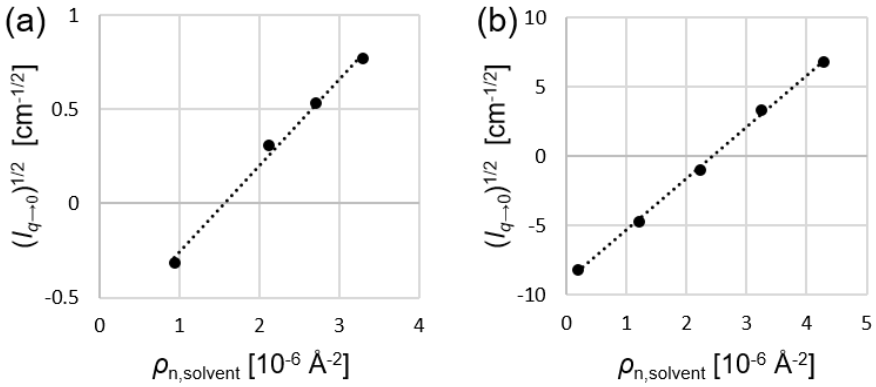

Figure 2.4. SANS intensities extrapolated to the zero angle ($q \to 0$) plotted as functions of solvent SLDs. The dotted lines are linear fits. (a) 5 wt% solutions of PC_{500} homopolymer and (b) 1 wt% solutions of PF_{180}-*b*-PC_{300} block copolymer were used, respectively.

from the solvent contrast variation studies and listed on Table 2.2. It is noted that separate density measurement using mercury intrusion porosimetry gives $\rho_{g,PF} \simeq 1.7$, which agrees well with the results from SLD measurement.

SAXS Model Fit. The SAXS profiles of PF-*b*-PC micelles were adjusted by the detailed fitting model given by Federsen *et al.*,[31] where the micelles are modelled as spherical cores and polymer brushes attached to the core surface. All contributions from the core and the corona chains which give rise to the scattering from a single micelle are considered to model the scattering form factor for a micelle, $P_{mic}(q)$, which gives

$$P_{mic}(q) = [N_{agg}\beta_{corona}A_{core}(q)]^2 + 2N_{agg}{}^2\beta_{core}\beta_{corona}A_{core}(q)A_{corona}(q) + N_{agg}\beta_{corona}{}^2P_{corona}(q) + N_{agg}(N_{agg} - 1)[\beta_{corona}A_{corona}(q)]^2 \quad (2.4)$$

where q is the scattering vector, N_{agg} the aggregation number, and β_i total excess scattering length of species i (i denotes either the core or the corona block) defined as $\beta_i = v_i(\rho_i - \rho_{solvent})$. Here, v_i is the molecular volume of the chain i and ρ_i is the scattering length densities (SLDs) of species i.

The first term in eq 2.4 is the self-correlation of the spherical core with radius R_{core} and width of the core-corona interface σ_{int} at which SLD smoothly decays. The normalized form factor of the core, $A_{core}(q)^2$, is given as

$$A_{core}(q)^2 = \Phi(qR_{core})^2 \exp(-q^2\sigma_{int}{}^2) \quad (2.5)$$

where $\Phi(x) = 3x^{-3}(\sin x - x\cos x)$, the Fourier transformed density function. The second term in eq 2.4 is the cross-correlation between the core and the corona chains, where the normalized Fourier transform of the radial density distribution function of the corona ($\phi_{corona}(r)$) is given as

$$A_{corona}(q) = \frac{4\pi\int \phi_{corona}(r)\frac{\sin(qr)}{qr}r^2dr}{4\pi\int \phi_{corona}(r)r^2dr} \exp(-q^2\sigma_{int}{}^2/2) \quad (2.6)$$

assuming radial symmetry of the corona density profile. A number of models for $\phi_{corona}(r)$ have been proposed to describe the real behavior of micelles under various conditions. Here, a linear combination of two cubic b spline functions with two fitting parameters was chosen, following the works by Pedersen *et al.*[xx] The last two terms in eq 2.4 are the self- and cross-correlations within the corona domain, where the chain form factor, $P_{corona}(q)$, is approximated by the Debye function for a Gaussian chain with radius of gyration R_g,

$$P_{corona}(q) = 2x^{-2}(\exp(-x) - 1 + x) \quad (2.7)$$

with $x = q^2R_g{}^2$.

The total scattering intensity is obtained using the form factor of micelle and the hard-sphere structure factor ($S(q)$),

$$I(q) = P_{mic}(q) + A_{mic}(q)^2[S(q) - 1] \quad (2.8)$$

where $A_{mic}(q)$ is the form factor amplitude of the radial scattering length distribution given by

$$A_{mic}(q) = N_{agg}[\beta_{core}A_{core}(q) + \beta_{corona}A_{corona}(q)]. \quad (2.9)$$

It is noted that the structure factor brings two additional fitting parameters, namely, the hard sphere radius (R_{hs}) and volume fraction (η_{hs}). Furthermore, a Gaussian distribution for the core radius, $D(R_{core})$, is employed to account for polydispersity in micelle size. The total scattering intensity for the polydisperse model is given as

$$I(q) = \int D(R_{core})\{P_{mic}(q) + A_{mic}(q)^2[S(q) - 1]\}dR_{core} \quad (2.10)$$

where the Gaussian distribution $D(R_{core})$ is parameterized with the average radius $\langle R_{core} \rangle$ and the standard deviation σ_R and truncated at $R_{core} = 0$ for the calculation. Eq 2.10 was used to fit the absolute-scaled SAXS data using IGOR Pro.

2.3. Results and Discussion

2.3.1. Preparation and Characterization of PF-*b*-PC Block Copolymer Micelles

We have investigated the structure of block copolymer micelle formed with a bottlebrush core of poly(5-perfluorooctyl norbornene) (PF) and a linear, flexible corona of poly(*N*-Cyclohexyl-*exo*-norbornene-5,6-dicarboxyimide) (PC) in THF, a selective solvent to PC block, as described in Figure 2.1. PF-*b*-PC block copolymers were synthesized through ROMP where PC block was synthesized and followed by PF block sequentially in dichloromethane using the Grubbs 3rd generation catalyst at 0 ºC. The molecular characteristics, determined by size exclusion chromatography, ^{1}H NMR spectroscopy, and elemental analysis (EA), are shown in Table 2.3. Polymer solutions containing 1 wt% block copolymer were prepared by dissolving PF-*b*-PC block copolymers in THF and followed by annealing at 60 ºC for at least 24 hr and cooling down to room temperature slowly.

Figure 2.5 displays SAXS patterns for all 1 wt% PF-*b*-PC block copolymer solutions in THF at 25 ºC. All polymer solutions show a considerable fluctuation which reflects that the micelles show relatively sharp interface between the core and the corona. In addition, the first minimum in the fluctuation progressively shifts toward lower q as the core block length increases with the same corona block length, which indicates that the core dimension increases as does the core block length. The solid curves shown in Figure 2.5 represent the best fit to the detailed model, and the fitting results are summarized in Table 2.4.

Table 2.3. Molecular Characteristics of PF-*b*-PC used in this study.

Sample code	N_{PF}[a]	N_{PC}[b]	f_{PF}[c]	M_w/M_n[d]
PC_{50}	-	50	0	1.05
PF_{35}-*b*-PC_{50}	35	50	0.53	1.05[e]
PF_{56}-*b*-PC_{50}	56	50	0.65	
PF_{79}-*b*-PC_{50}	79	50	0.73	
PC_{300}	-	300	0	1.05
PF_{90}-*b*-PC_{300}H	85	300	0.32	1.05[e]
PF_{90}-*b*-PC_{300}D	90	300	0.33	
PF_{120}-*b*-PC_{300}H	120	300	0.39	
PF_{120}-*b*-PC_{300}D	122	300	0.40	
PF_{180}-*b*-PC_{300}H	186	300	0.50	
PF_{180}-*b*-PC_{300}D	180	300	0.49	

[a] Number-average repeat unit of PF block was estimated using EA. [b] Number-average repeat unit of PC block was estimated using ^{1}H NMR. [c] Weight fraction of PF block from PF-*b*-PC copolymer. [d] Polydispersity of polymer was measured using SEC. [e] Average between M_w/M_n of PF and PC homopolymers.

Prior to the structural analysis, it should be addressed whether the micelles are at equilibrium under the SAXS measurement. Molecular exchange between micelles is the fundamental process to achieve thermodynamic equilibrium structure.[32, 33] Recently, non-ergodicity of block copolymer micelles has been observed,[34] which is mainly attributed to slow or hindered exchange process due to both/either a glassy core and/or a high incompatibility between the core block and the medium. In our system, the incompatibility between PF block and THF is significantly large as $\chi_{PF\text{-}THF} \approx 1.03$ at 25 ºC, which is estimated by

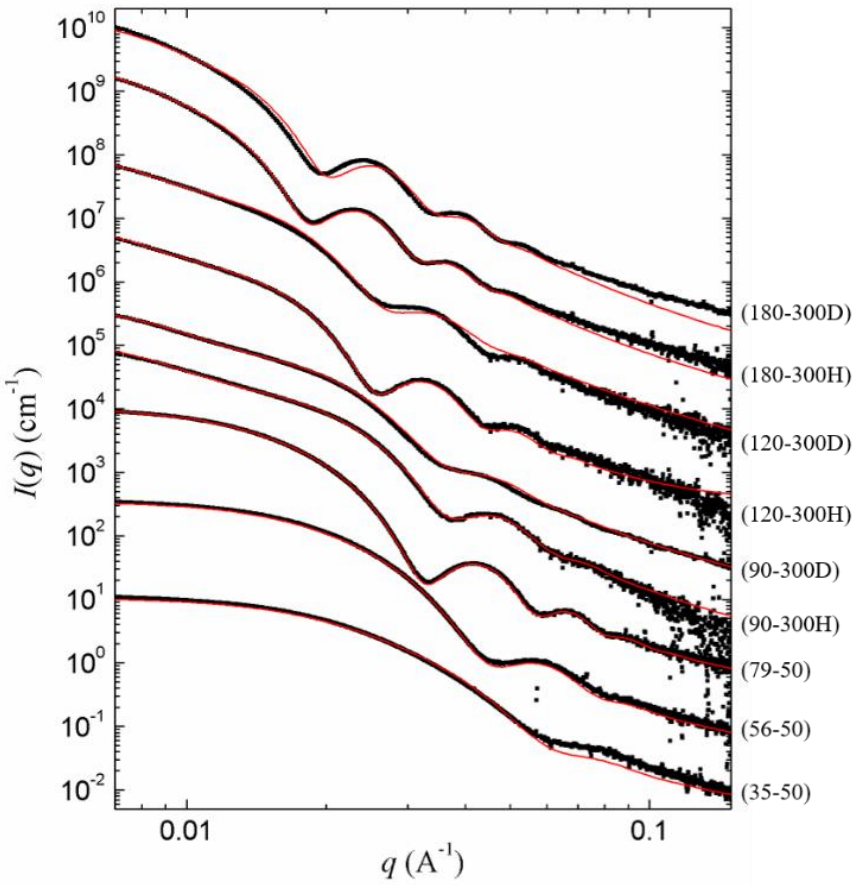

Figure 2.5. SAXS intensity curves for PF_n-*b*-PC_m (the numbers in parentheses denotes n and m, the numbers of repeat units, respectively) at 1 wt% and 25 °C. For clarity, data were scaled by factors of 10. The red solid lines are best fits to the spherical micelle model.

Table 2.4. SAXS fitting results of PF-b-PC micelles.

Sample code	p^a	R_{core} [nm]	$\sigma_R{}^b$ [nm]	$\Phi_{solvent}{}^c$	$R_h{}^d$ [nm]	L_{corona} [nm]
PF_{35}-*b*-PC_{50}	78	7.7	1.0	0.275	17.4	9.7
PF_{56}-*b*-PC_{50}	126	10.1	1.1	0.190	20.1	10.0
PF_{79}-*b*-PC_{50}	224	13.8	1.1	0.201	20.7	6.9
PF_{90}-*b*-PC_{300}H	155	12.7	1.3	0.180	38.2	25.5
PF_{90}-*b*-PC_{300}D	180	13.4	1.8	0.189	41.2	27.8
PF_{120}-*b*-PC_{300}H	340	18.0	1.6	0.169	50.0	32.0
PF_{120}-*b*-PC_{300}D	346	18.1	2.2	0.163	50.0	31.9
PF_{180}-*b*-PC_{300}H	640	25.1	2.3	0.157	58.2	33.1
PF_{180}-*b*-PC_{300}D	531	23.9	2.3	0.165	57.8	33.9

[a] Aggregation number. [b] Standard deviation of R_{core}, the core radius. [c] Volume fraction of solvent inside the micellar core. [d] Hydrodynamic radius obtained using DLS.

the surface energy analysis of PF homopolymer. Our preliminary results on chain exchange dynamics between PF_{90}-*b*-PC_{300} micelles in THF showed that chain exchange rate is quite fast at 50 ºC,[35] which is consistent with the previous observation.[36] The enthalpic barrier of chain pull-out is partially attenuated by the effect of corona block, and thus appreciable chain exchange rate is achieved even with high χ system. Although the appreciable chain exchange rate does not guarantee the equilibrium, consistent micelle preparation by annealing at 60 ºC for 24 hr and slowly cooling down warrants the application of equilibrium theory. Furthermore, all PF-*b*-PC micelles are nearly monodispersed ($\sigma_R/R_{core} \simeq 0.1$) at room temperature, and negligibly temperature-dependent between room temperature and 60 ºC.

2.3.2. Effect of PF Core Block Stiffness on the Structure of Block Copolymer Micelles

Figure 2.6.a shows that R_{core} of PF_n-*b*-PC_{300} micelles are scaled on the number of repeat units in the PF core block (N_{core}) as $R_{core} \sim N_{core}^{0.84 \pm 0.04}$. It is noted that incorporation of data from PF_n-*b*-PC_{50}, copolymers with different corona block length, into consideration does not change its scaling behavior. In Figure 2.6.b, a global fit results in $R_{core} \sim N_{core}^{0.85 \pm 0.03}$, almost the same scaling with previous one. Furthermore, it can be deduced that R_{core} depends on N_{corona} approximately as $R_{core} \sim N_{corona}^{-0.1}$, which is in good agreement with reported scaling exponent (from -0.17 to 0) in the literature.[6] It is noteworthy that the exponent for N_{core} is considerably larger than either values predicted from the scaling arguments, where the exponents 0.6 and 0.67 are expected for hairy micelles ($N_{core} \ll N_{corona}$) and crew-cut micelles ($N_{core} \gg N_{corona}$), respectively, or from the more realistic theories, such as self-consistent field theory and comprehensive mean-field theory which expect the exponents to be 0.67–0.76 and 0.70–0.73, respectively.[9, 37] In the present study, the exponent of 0.84 ± 0.04 indicates that the bottlebrush core blocks are significantly stretched in the core, which is mainly attributed to the steric repulsion between the densely grafted side chains of the PF core blocks.

Compared to linear Gaussian chains, the chain stiffness of the bottlebrush polymers can be related to the inherent stiffness of norbornene backbone and the conformational change due to side chain overlap. Lin et al. reported that norbornene-containing polymers behaves nearly like a flexible Gaussian chains, resulting in negligible effect of norbornene backbone.[23] Moreover, the side chain overlap is estimated by the comparison between the radius of gyration of the PF side chain, $R_{g,SC}$, and the distance of the side chains. Due to the inherent rigidity of helical C_8F_{17} side chain,[38] $R_{g,SC}$ is estimated as the radius of rotating

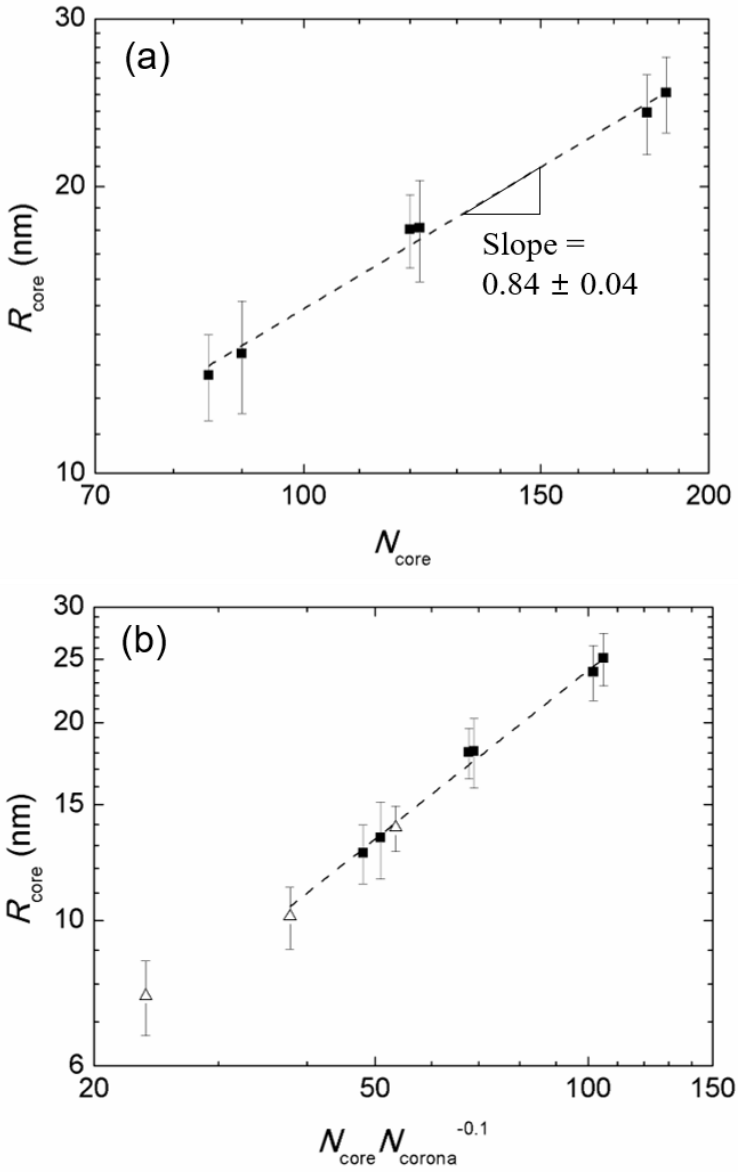

Figure 2.6. Double logarithmic plots of the core radius (R_{core}) with respect to N_{core}, where N_{core} is the number of repeat units of PF blocks. In (a), data from only PF_n-*b*-PC_{300} samples are displayed. In (b), data from only PF_n-*b*-PC_{300} samples are displayed.

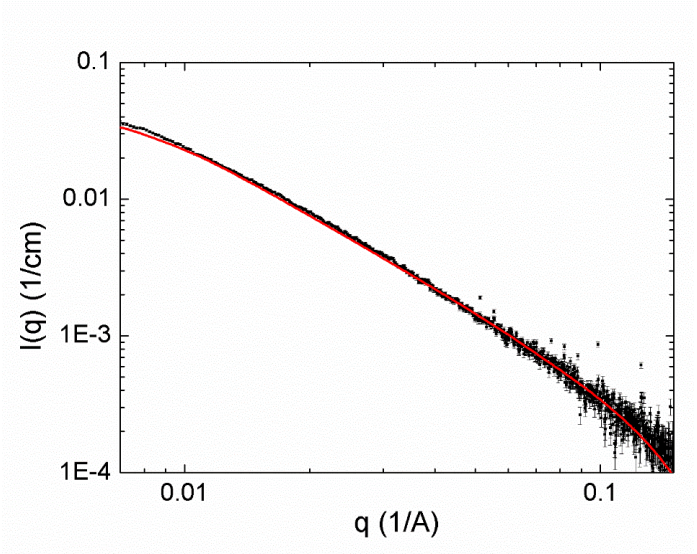

Figure 2.7. SAXS intensity curve of 2.5 mg/ml PF homopolymers (N = 500) solution with nearly theta solvent α,α,α-trifluorotoluene. The solid line indicates fit using worm-like chain model.

helical rod about the axis of connecting bond, $R_{g,SC} = l_{SC}|\cos\theta| = 1.08$ nm, where l_{SC} is the length of side chain (l_{SC} = 1.15 nm) and θ is the bond angle (θ = 109.5°).[39] Assuming the distance between side chains as 0.62 nm that is considerably smaller than $2\times R_{g,SC}$,[40] the backbone is expected to stretch to reduce the side chain overlap.

Furthermore, complementary SAXS study on PF homopolymers (DP = 500) revealed that the conformation of PF in theta solvent α,α,α-trifluorotoluene is well-described with a worm-like chain (WLC) model, rather than Debye function which represents a Gaussian chain. Figure 2.7 shows good quality of fit by the WLC model with the known contour length (Nb = 31 nm), which gave the Kuhn length, l_K, of 4.47 nm and subsequently the radius of gyration of the PF core block, $R_{g,PF}$, of 6.24 nm and 9.08 nm for DP = 90 and 180, respectively.

Since l_K is comparable to $R_{g,PF}$ in our experimental condition, PF core blocks are expected to stretch, resulting in deviation from flexible Gaussian chains.

Solvent volume fraction inside the core, φ_{solv}, estimated by $(1 - \varphi_{solv})(4/3)\pi R_{core}^3 = p\, \upsilon_{core}$, where υ_{core} is the core block volume per chain, is relatively small between 0.16 and 0.28 as shown in Table 2. As the incompatibility between the core blocks and the medium increases, φ_{solv} decreases. Bearing in mind that $\chi_{PF\text{-}THF} \approx 1.03$, the estimated φ_{solv} values are in good agreement with Seitz et al. who estimated using the self-consistent field theory that φ_{solv} decreases from 0.6 to 0.25 as $\chi_{core\text{-}solvent}$ increases from 0.7 to 1.1.[41] Non-trivial value of the solvent fraction in the core area implies that the strong segregation condition is not fulfilled, which provides the relaxation of the chain stretching. It is unlike previous studies on perfluorinated block copolymers where super-strong segregation limit was reached due to enormous incompatibility between perfluorinated block and solvents.[12] Thus, such stronger dependence of R_{core} on PF block length than the previous results is accounted for the stiffness of PF block, not for its incompatibility to solvent.

It is apparent that the bottlebrush core block favors in larger R_{core} than what would be made from linear core block. For instance, R_{core} from PF_{180}-*b*-PC_{300} is 24.5 nm, which far exceeds the end-to-end distance of the PF core, $R_o = 8.7$ nm, if PF block were instead a Gaussian polymer. This characteristic of large R_{core} is due to the smaller cost of free energy from entropic elasticity in stretching such stiff chains. Also, the stronger dependence of R_{core} on N_{core} is closely related with such reduction in the elastic free energy of core block, which can be analyzed by simple generalization of the pre-existing scaling model. We chose the classical model for the crew-cut regime as the reference, which considers only the interfacial energy per chain, F_{int}, and the free energy per chain from entropic elasticity of the core, $F_{el,core}$. Following de Gennes,[5] $F_{int} \sim$

$R_{core}^2/p \sim p^{-1/3}N^{2/3}$ and $F_{el,core} \sim R_{core}^2/R_o^2$, where p is the aggregation number of micelle and R_o the end-to-end distance of core block. For real chains with finite contour length, R_o depends on N as $R_o(N) \sim N^v$ where v ranges from 0.5 (ideal flexible polymers) to 1.0 (infinitely stiff polymers). Actual v value is determined regarding to the persistence length and contour length of chain, as demonstrated in recent computational studies.[19, 42] A generalization with respect to v gives $F_{el,core} \sim p^{2/3}N^{(2/3-2v)}$, and upon minimizing ($F_{int} + F_{el,core}$) with respect to p, one obtains the scaling behavior $p \sim N^{2v}$ and consequently $R_{core} \sim N^{\alpha}$ with $\alpha = (2v + 1)/3$ for crew-cut micelles, which ranges from 2/3 ($v = 0.5$) to 1 ($v = 1$).

We estimate $v \simeq 0.6$ for PF block by applying ref. 31 and characteristics of the PF block, where $2\times R_{g,SC} = 2.16$ nm being the diameter of the effective "blob", which brings about $\alpha \simeq 0.73$. This is a slight increase than the original exponent of 2/3 but still lower than that from the experiment ($\alpha = 0.84$). Such discrepancy may stem from the neglect of the corona elastic free energy, as is the main drawback of the scaling approaches. As many authors have pointed out, many of the real systems (including the present one) lie at the intermediate between the hairy and crew-cut regime, where the elastic free energy of corona is appreciable as well as that of the core.[8] Consequently, the scaling theory always underestimates the exponent ($\Delta\alpha \sim 0.1$) compared to more realistic self-consistent field and mean-field theories.[9, 37, 43] Likewise, many experimental scaling works on flexible diblock copolymers in the intermediate-to-crew-cut regime support such deviation, as exponents exceeding 0.7 are frequently observed from literature.[36, 44, 45] In this perspective, the discrepancy ($\Delta\alpha = 0.11$) obtained from our scaling result seems plausible, suggesting the validity of the present model in describing changes in the scaling of R_{core} caused by the stiffness of the core block.

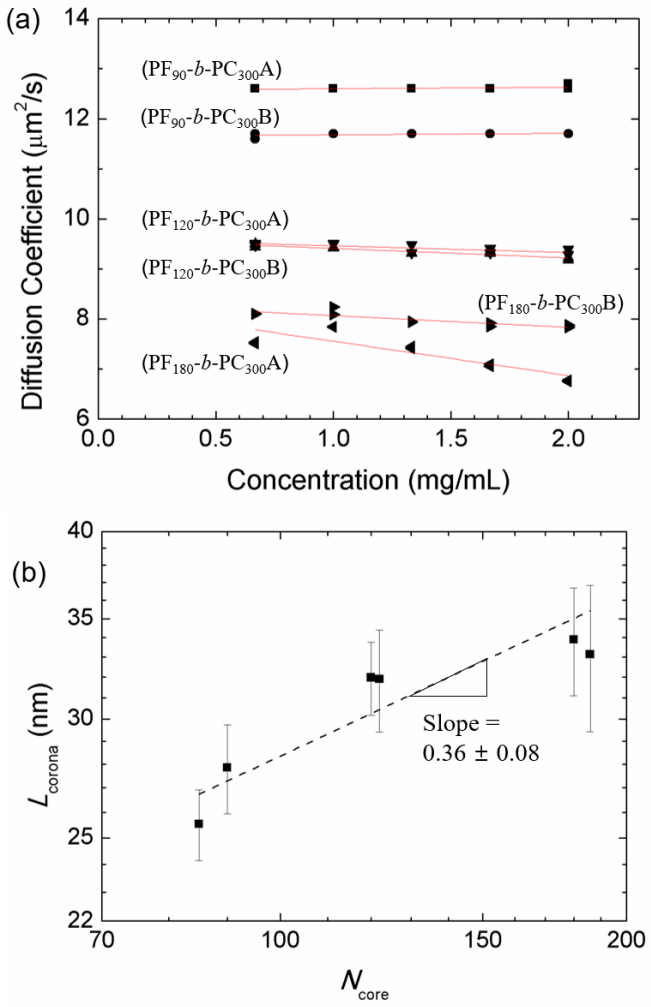

Figure 2.8. Effect of N_{core} on the corona thickness (L_{corona}). (a) Diffusion coefficients (D) measured from DLS experiments with varying polymer concentrations. Each datapoint is determined with cumulant method. The solid lines are linear fits from which the zero-concentration diffusion coefficient (D_0) was determined and used for the calculation of the hydrodynamic radius (R_h) using the Stokes-Einstein relation, $D_0 = k_B T/6\pi\eta R_h$, where k_B is the Boltzmann constant, T the temperature, and η the viscosity of solvent. (b) Double logarithmic plots of L_{corona} with respect to N_{core}, where N_{core} is the number of repeat units of PF blocks. Data are from PF_n-*b*-PC_{300} and power-law fits are displayed.

Figure 2.8 shows clear dependence of the corona thickness, defined as $L_{corona} = R_h - R_{core}$ where R_h is hydrodynamic radius determined from DLS, on N_{core} as $L_{corona} \sim N_{core}^{0.36 \pm 0.08}$. In contrast, the scaling theory for linear block copolymers predicts $L_{corona} \sim N_{corona}^{0.16–0.20}$ for the hairy regime and negligible dependence ($L_{corona} \sim N_{corona}^{0}$) for the crew-cut regime. However, since L_{corona} is sufficiently larger than R_{core} in this study, this stronger dependence turns out to be consistent with the pre-existing model for the hairy micelles. From the classical theory developed by Daoud and Cotton,[6] the radius of a star polymer (or, a hairy micelle) is scaled as $R_{star} \sim N_{corona}^{0.6} p^{0.2}$, where p is the number of arms (or, the aggregation number of micelle). We could formulate a scaling of $p \sim N_{core}^{1.68}$ from the SAXS data of PF$_n$-*b*-PC$_{300}$ series, which turns into $L_{corona} \sim p^{0.2} \sim N_{core}^{0.34}$, revealing a good agreement between the model and the experimental scaling. This correspondence demonstrates that stiff bottlebrush core block significantly stretches the corona, even when the corona block itself is flexible, by constructing a larger micelle compared to one with the linear core block.

2.4. Summary

In the present study, the structures of the micelles from self-assembly of the model block copolymers, PF-*b*-PC, in THF solutions were studied. Due to the long fluoroalkyl side-chain on every repeat unit, bottlebrush PF core block gains appreciable chain stiffness. It was found that this stiffness causes the core block as well as the corona block to be stretched more strongly than what has been predicted from linear flexible block copolymers. The reduction in elastic entropy of the core block with increasing chain stiffness is responsible for both characteristic behavior, which was rationalized by an appropriate scaling model. This study directs to the rational assembly of the block copolymer micelles with desired geometry and dimensions through the control over the length and grafting density of the side-chains of the core block, which will be beneficial for applications such as solution-phase photonics, smart delivery vehicles, and ordered soft templates.

Chapter 3. Chain Exchange Kinetics of Block Copolymer Micelles with Bottlebrush Core Block

3.1. Introduction

Self-assembly of block copolymers in solutions finds many applications including multifunctional nanoreactors and highly ordered soft templates, where the performance is closely related to the uniformity of the self-assembled structures. Therefore, exchange dynamics of block copolymer chains between self-assembled aggregates needs to be sufficiently fast to achieve well-defined equilibrium states in block copolymer systems. However, owing to the slower chain relaxation ($\tau \sim N^{2-3}$, where N is the number of repeat units) and the larger incompatibility ($\sim \chi N$, where χ is the Flory-Huggins interaction parameter) between solvent and the insoluble "core" block with increasing core block length,[33, 46] kinetic retardation (or, non-ergodicity) is a typical problem for block copolymers of high molecular weight (MW).[47]

Introducing bottlebrush architecture to the core block provides an opportunity to accelerate relaxation of the chain. Bottlebrush polymers are characterized with ultra-high entanglement molecular weight (M_e) and reduced molecular friction since strong steric and/or excluded volume interactions between adjacent lengthy side-chains increase the stiffness of backbone and the distance between adjacent backbones belonging to different chains.[48-50] Therefore, bottlebrush architecture has been considered advantageous to the self-assembly of high MW block copolymers as its accelerating effect on the chain dynamics can resolve the kinetic retardation.[10, 51] However, no direct

evidence and/or quantification of such acceleration in self-assembly kinetics was observed either in melts or in solutions so far.

We demonstrate an idealized kinetic experiment using a pair of differently labeled block copolymers with nearly identical molecular characteristics to quantify the single chain exchange kinetics between aggregates self-assembled from bottlebrush core block in a selective solution. We recently developed diblock copolymers of poly(5-perfluorooctyl norbornene) (PF) and poly(*N*-Cyclohexyl-*exo*-norbornene-5,6-dicarboxyimide) (PC), PF-*b*-PC, where long fluoroalkyl side-chains tethered to backbone brings considerable stiffness in PF block.[52] Herein, we investigate the relaxation kinetics of PF block in bulk and in spherical micelles and discuss the impact of bottlebrush architecture on the dynamics of self-assembly. First, we characterize zero-shear viscosities (η_0) of PF homopolymer melts with different N and temperature (T), from which the fractional free volume (f) and the apparent flow activation energy (E_{flow}) are deduced. The absence of entanglements within experimental MW range ensures validity of the Rouse model, from which the monomeric friction coefficient (ζ) of PF block is determined. Second, we directly measure the chain exchange kinetics within PF-*b*-PC spherical micelles formed in THF, a solvent selective to PC block, using time-resolved small-angle neutron scattering (TR-SANS) experiments. We prepared an isotopic pair of deuterated and protonated block copolymers for TR-SANS experiments in order to quantify the time-dependent extent of chain exchange in quasi-equilibrium situation. The kinetic data from TR-SANS is analyzed with the polydispersed chain length model,[33] from which the monomeric friction coefficient inside the core and the energy barrier for chain extraction are obtained. It is shown that the relaxation of PF-*b*-PC micelles is significantly faster than that of linear block copolymer micelles with similar repeat unit chemistry and/or solvent-core incompatibility.

Along with our previous finding that bottlebrush architecture at the core blocks lead to significantly larger aggregates, the present study suggests that the bottlebrush architecture provides rapid equilibration and therefore uniform structures of large self-assembled domains from high MW block copolymers.

3.2. Experimental Section

Materials. Grubbs 3rd generation catalyst, N-Cyclohexyl-exo-norbornene-5,6-dicarboxyimide (ChNDI), and 5-(perfluorooctyl)norbornene (NB8F) were synthesized using previously established procedures[52, 53]. For the preparation of deuterium-labeled polymers, deuterated ChNDI (dChNDI) was synthesized using cyclohexyl-d_{11}-amine (98 atom % deuterated, purchased from C/D/N Isotopes). Comparison of ^{1}H NMR spectra of ChNDI and dChNDI in Figure 3.1 informs that 9.5 hydrogens among total 11 hydrogens (86 atom %) at cyclohexylamine group of dChNDI are deuterium-substituted, rather than all 11 hydrogens. Anhydrous dichloromethane (DCM) and α,α,α-trifluorotoluene (TFT) were purchased from Sigma-Aldrich and degassed through three freeze-pump-thaw cycles directly before use. All homopolymers and diblock copolymers pNB8F-*b*-pChNDI (hereafter noted as PF-*b*-PC) were prepared using previously reported ring-opening metathesis polymerization (ROMP) technique[52], with the exception of NB8F homopolymers of which polymerization reaction was carried out in TFT. Protonated tetrahydrofuran (h-THF) and perdeuterated THF (d-THF) were purchased from Sigma-Aldrich and used without further purification.

Molecular Characterization. The polymers were characterized by size exclusion chromatography (SEC), matrix-assisted laser desorption/ionization (MALDI), and elemental analysis (EA). Molecular weight and polydispersity (M_w/M_n) of ChNDI "mother" polymer (PC) were estimated by SEC (YL9100 HPLC, YL Instrument) using THF as an eluent. Molecular weight and polydispersity of NB8F homopolymers (PF) were estimated by MALDI (Voyager DE-STR mass spectrometer, Applied Biosystems) using 2,5-dihydroxybenzoic acid (DHB) as a matrix substance. The complete conversion

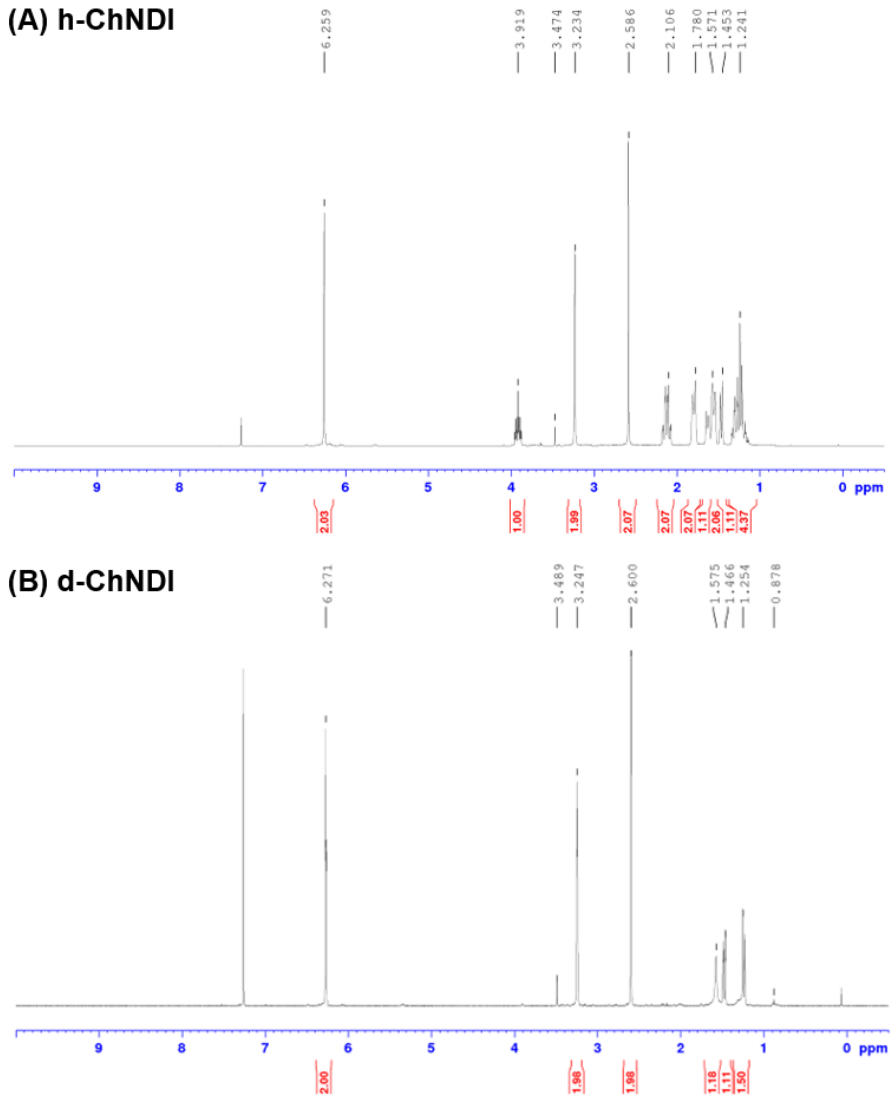

Figure 3.1. ^{1}H NMR spectra of (A) ChNDI and (B) dChNDI. In (B), peak area between 1.2–1.3 ppm shows that ca. 1.5 protons remain at cyclohexylamine group of dChNDI.

of ROMP for both kinds of homopolymers, as well as for the block copolymers, was confirmed by ^{1}H NMR spectroscopy. All PF-*b*-PC block copolymers were repeatedly precipitated in mixture of toluene and petroleum ether (3:1 by volume) and re-dissolved several times before characterization and sample preparation in order to eliminate small portions of "dead" PC homopolymers (at which the propagation of the PF block did not occurred) from the copolymers. After purification, elemental weight fractions of carbon and hydrogen was measured for aliquots of PF-*b*-PC by EA (TruSpec Micro elemental analyzer, LECO), which were used for calculation of the molecular weights of PF block grown at the PC "mother" polymers with known molecular weights. The molecular characteristics are summarized in Table 3.1.

Differential Scanning Calorimetry. Thermal analysis of PF homopolymer (N = 500) was performed using PerkinElmer DSC 4000 apparatus. Samples were repeatedly heated and cooled between 20 – 100 °C with ramping speed of 5 °C/min, and profile from the second heating was used to estimate the glass transition temperature, T_g. For the measurement of T_g depression upon THF swelling in PF, polymer samples placed in aluminum DSC cups were saturated with THF vapor in a closed chamber for 3 h before sealing of specimen. After gravimetric measurement for THF weight fraction, samples were repeatedly heated and cooled between –50 – 30 °C.

Rheological characterization of PF melts with different molecular weights were conducted using oscillatory shear rheometer (MCR 302, Anton Paar). Samples were analyzed under nitrogen flow on 25 mm diameter parallel plates. Small-amplitude oscillatory shear measurements were carried out at low strains and a frequency range of 0.001-1 rad/s. Zero-shear-rate viscosities at a temperature range of 70 °C to 130 °C were estimated by extrapolation of data

Table 3.1. Molecular Characteristics of polymers used in this study.

Sample code	N_{PF}[a]	N_{PC}[b]	M_w/M_n
PF_{26}	26	-	1.05[c]
PF_{50}	50	-	(1.05)[d]
PF_{75}	75	-	
PF_{90}-*b*-hPC	85	300	(1.05)[e]
PF_{90}-*b*-dPC	90	300	

[a] Number-average repeat unit of PF block was estimated using EA. [b] Number-average repeat unit of PC block was estimated using ^{1}H NMR. [c] Polydispersity measured using MALDI. [d] Due to the lack of useful method, polydispersities are assumed same with known polydispersity (1.05) of PF_{26}. [e] Average between M_w/M_n of PF and PC homopolymers.

Table 3.5. Neutron SLDs, X-ray SLDs, and gravimetric densities.[a]

Component	ρ_n [10^{-6} Å^{-2}]	ρ_x [10^{-6} Å^{-2}]	ρ_g [g/ml]
PF	3.24	14.2	1.70
hPC	1.61	12.1	1.32
dPC[b]	4.73	12.1	1.37

[a] Values are estimated from the same method described in Chapter 2. [b] Neutron and X-ray SLDs of dPC are estimated with the density of dPC and the deuterium substitution of 9.5 hydrogens (characterized from ^{1}H NMR analysis). The density of dPC is calculated assuming the same molecular volume of dPC with that of hPC.

within the low frequency region. This temperature range is far above T_g of PF (55 °C).

Small-Angle Neutron Scattering (SANS). 1 w/v % polymer solutions with with either protonated block copolymers (PF-*b*-hPC) or deuterated block copolymers (PF-*b*-dPC) for SANS and time-resolved SANS (TR-SANS) experiments were individually prepared by dissolving the polymers in the isotopic mixture of h-THF (49 vol %) and d-THF (51 vol %). The composition of the isotopic mixture was determined to be matched with a mean value of hPC and dPC in terms of neutron scattering length density (SLD) (Table 3.2). The polymer solutions were annealed overnight at 60 °C in tightly sealed vials to bring the block copolymer micelles into the equilibrium state. The polymer solutions were then cooled down and syringe filtered before use. Additionally, 1 w/v % of "pre-mixed" polymer solutions of PF-*b*-hPC and PF-*b*-dPC with mass ratio of 1:1 were prepared by the same method previously described.

SANS experiments individually performed on QUOKKA beamline at Australian Center for Neutron Scattering, Australian Nuclear Science and Technology Organization (Australia). Polymers of which core PF blocks consist of 90 repeat units (N_{PF} = 90) (i.e., PF90-hPC and PF90-dPC) were examined with instrument configuration of a wavelength λ = 6 Å, a wavelength spread ($\Delta\lambda/\lambda$) of 0.12, a SDD of 11.5 m was adapted. Samples were loaded in the 2 mm demountable cells and placed in a temperature-controlled heating block, which could maintain the desired temperature within ±1 °C. For each temperature, the scattering intensities of the h-, d-, and premixed micelle solutions were first collected for 30 min to define the initial and saturated states of the isotopic micelle mixture. Then, PF-*b*-hPC and PF-*b*-dPC solutions were injected in a test vial, mixed by shaking for 10 s, and immediately transferred to the cells and placed in the heating block for TR-SANS experiments.

Subsequently, scattering intensities with a time resolution of 5 min were collected by a 2-D detector during 2-3 h of the whole measurements. The 2-D scattering images were azimuthally averaged, reduced to an absolute scale, and background subtracted using the package provided by QUOKKA based on IGOR Pro.

Analysis of TR-SANS Data. For given set of scattering length densities (SLDs) and structural properties of micellar solutions, it is able to quantitatively express the extent of chain exchange through the relaxation function, $R(t)$, which is obtained from the time-dependent scattering intensities. We introduce here the exact formalism of $R(t)$ and various coupled quantities for the blend of different isotopes PF-hPC and PF-dPC dissolved in a selective solvent. The scattering model is based on Federsen *et al.*,[1] and we adopted many ideas from several literatures to treat the time-dependency and binary mixture problems.[2-3] The scattering intensity of single-species micellar solutions (I_i, where i denotes either protonated (H) or deuterated (D) version of PF-PC block copolymers) is expressed via modification of eq 2.8,

$$\begin{aligned} I_i &= (N_{\mathrm{p},i}/V)\{P_{\mathrm{mic},i}(q) + [S(q) - 1]A_{\mathrm{mic},i}(q)^2\} \\ &= V^{-1}\{N_{\mathrm{p},i}P_{\mathrm{mic},i}(q) + [(S(q) - 1)/N_{\mathrm{p},i}][N_{\mathrm{p},i}A_{\mathrm{mic},i}(q)]^2\} \end{aligned} \tag{3.1}$$

where N_p is the number of particles (i.e., micelles) in the system and V is the volume of the system, and every other notation is consistent with the Chapter 2.[4] Here, $P_{\mathrm{mic},i}(q)$ is the scattering form factor (eq 2.4) and $A_{\mathrm{mic},i}(q)$ is the form factor amplitude of the radial scattering length distribution (eq 2.9) of micelle i. It is convenient to rewrite the expression of $P_\mathrm{mic}(q)$ for further derivation:

$$P_\mathrm{mic}(q) = A_\mathrm{mic}(q)^2 + N_\mathrm{agg}\beta_\mathrm{corona}^2[P_\mathrm{corona}(q) - A_\mathrm{corona}(q)]. \tag{3.2}$$

In the absence of chain exchange, binary mixture solutions of PF-hPC and PF-dPC micelles which share the identical structures could be developed in a similar fashion with eq 3.1,

$$I_{mix} = V^{-1}\{N_{p,H}P_{mic,H}(q) + N_{p,D}P_{mic,D}(q) + [(S(q) - 1)/N_p][N_{p,H}A_{mic,H}(q) + N_{p,D}A_{mic,D}(q)]^2\} \quad (3.3)$$

where $N_p = N_{p,H} + N_{p,D}$. Fortunately, this complicated expression could be simplified greatly by imposing several conditions. First, if the contents of PF-hPC and PF-dPC dissolved in the mixture are equal ($N_{p,H} = N_{p,D} = N_p/2$), then eq 3.3 is reduced to

$$\begin{aligned} I_{mix} &= V^{-1}\{(N_p/2)[P_{mic,H}(q) + P_{mic,D}(q)] \\ &\quad + [(S(q) - 1)/N_p]\,(N_p^2/4)\,[A_{mic,H}(q) + A_{mic,D}(q)]^2\} \\ &= (N_p/V)\{[P_{mic,H}(q) + P_{mic,D}(q)]/2 + (S(q) - 1)[(A_{mic,H}(q) + \\ &\quad A_{mic,D}(q))/2]^2\}. \end{aligned} \quad (3.4)$$

Second, if the SLD of solvent is matched to the average of hPC and dPC, then $\beta_{hPC} = -\beta_{dPC}$. Therefore,

$$\begin{aligned} P_{mic,H}(q) + P_{mic,D}(q) &= A_{mic,H}(q)^2 + A_{mic,D}(q)^2 \\ &\quad + 2N_{agg}\beta_{hPC}^2[P_{corona}(q) - A_{corona}(q)], \\ A_{mic,H}(q) + A_{mic,D}(q) &= N_{agg}[\beta_{hPF}A_{corona}(q) + \beta_{dPF}A_{corona}(q)] \\ &= 2N_{agg}\beta_{core}A_{core}(q), \\ A_{mic,H}(q)^2 + A_{mic,D}(q)^2 &= 2N_{agg}^2[(\beta_{core}A_{core}(q))^2 + (\beta_{hPC}A_{corona}(q))^2], \end{aligned}$$

then, eq 3.4 is further reduced to

$$I_{mix} = (N_p/V)\,N_{agg}^2[(\beta_{core}A_{core}(q))^2S(q) + (\beta_{hPC}A_{corona}(q))^2] + C(q), \quad (3.5)$$

where $C(q) = (N_p/V)\,N_{agg}\beta_{hPC}^2[P_{corona}(q) - A_{corona}(q)]$.

Indeed, eq 3.5 is not only capable of describing the mixture without exchange, but also the mixture where some exchange has been undergone. If the chains were exchanged, the contrast between the "mixed" corona and the solvent would decrease. Therefore, we can express the time-dependence through $\beta_{hPC}(t)$, which is hereafter regarded as the averaged-out corona contrast of PF-hPC micelle after mixing time t. The only time-dependent term from eq 3.5 is then $\beta_{hPC}(t)$, hence the time-dependent SANS intensity is

$$I_{mix}(t) = (N_p/V)N_{agg}^2[(\beta_{core}A_{core}(q))^2S(q) + (\beta_{hPC}(t)A_{corona}(q))^2] + C(q). \quad (3.6)$$

Followings are experimentally important corollaries from which the normalized relaxation function for the chain exchange, $R(t)$, is constructed.

$$I_\infty = I_{mix}(t \to \infty) = (N_p/V)\, N_{agg}^2[\beta_{core}A_{core}(q)]^2S(q) + C(q) \quad (3.7)$$

$$I_0 = I_{mix}(t = 0) = (N_p/V)\, N_{agg}^2\{[\beta_{core}A_{core}(q)]^2S(q) + [\beta_{hPC,0}A_{corona}(q)]^2\} + C(q) \quad (3.8)$$

$$R(t) = \{[I_{mix}(t) - I_\infty]/[I_0 - I_\infty]\}^{1/2} = \beta_{hPC}(t)/\beta_{hPC,0}. \quad (3.9)$$

where $I(t)$ is the scattering intensity of the mixture of PF-*b*-hPC and PF-*b*-dPC (mass ratio of 1:1) at given time of mixing t, I_0 is the initial scattering intensity at $t = 0$ (i.e., the moment at the absence of chain exchange), and I_∞ is the scattering intensity of perfectly mixed state ($t \to \infty$).

In conclusion, eq 3.9 suggests that $R(t)$ is the normalized contrast of the mixed corona of (once) PF-hPC micelle which was originally composed of only hPC corona. Of course, substitution of hPC corona to dPC corona concludes in equivalent results. Thus, $R(t)$ can be interpreted as the proportion of a polymer chain that still remains at the parent micelle after time t, statistically averaged throughout whole sample, which is naturally a decaying function of t.

The time-series data obtained from TR-SANS experiment were analyzed in terms of $R(t)$ using eq 3.9. Since the direct measurement of I_0 could be interrupted by possible chain exchange during initial homogenization step ($0 < t < 5$ min), eq 3.8 was used for evaluation of I_0 with parameters such as N_{agg} and $A_{corona}(q)$ obtained from the micelle model fitting. A sample of $I_0(q)$ evaluation was compared with the experimental curve obtained from the initial beam exposure of the isotopic mixture at the lowest temperature (i.e., 30 °C) where minimal chain exchange occurred. Figure 3.2 suggests that our derivation using eq 3.8 indeed agrees with what was measured in real SANS experiments. Notably, the error turned out to be negligible at the lower q range ($q < 0.01$ Å^{-}

[1]), therefore the data within this range was collected for the calculation of $R(t)$. The scattering intensity of the "pre-mixed" sample is used for I_∞, which assumes perfect mixing of PF-*b*-hPC and PF-*b*-dPC during the annealing step.

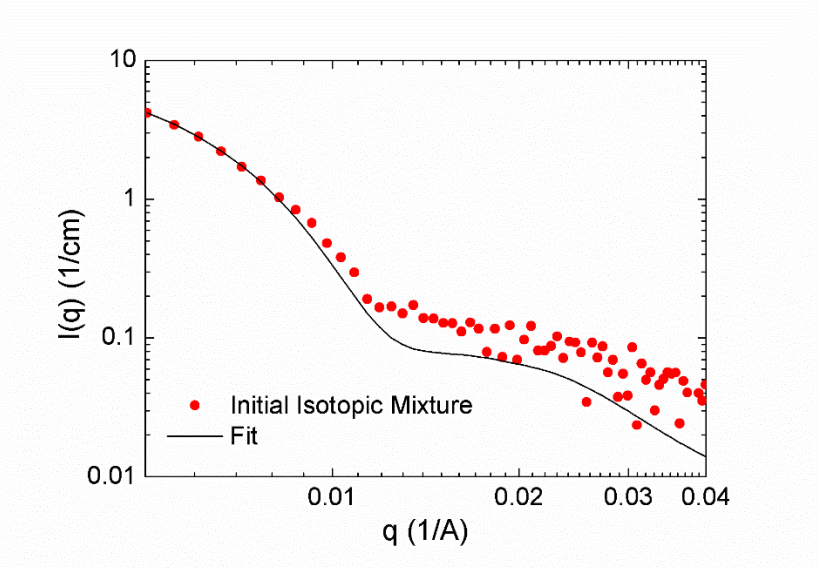

Figure 3.2. SANS intensity curve from the isotopic mixture of PF_{90}-*b*-hPC and PF_{90}-*b*-dPC, measured immediately after macroscopic mixing at 30 °C. Beam exposure time was 5 min. The solid line was calculated using eq 3.8.

3.3. Results and Discussion

3.3.1. Relaxation dynamics of bottlebrush polymer PF

Bottlebrush polymers are known to relax much faster than their linear analogues of similar MW, and recent rheological studies highlighted common dynamic characteristics of bottlebrush polymers. Since the lengthy side-chains forces the backbone conformation to be stretched to reduce their steric hindrance, bottlebrush polymers tend to have fewer entanglements and behave as Rouse chains at more extended MW regime.[54] Moreover, as the steric hindrance between side-chains at different backbones pulls adjacent backbone chains apart, a pronounced increase in the fractional free volume (f) with increasing side-chain length (N_{sc}) was found in bottlebrush polymers with short side-chains ($3 \leq N_{sc} \leq 6$), which in turn followed by the depression of T_g and the flow activation energy (E_{flow}).[50] These features altogether direct to acceleration of chain relaxation, which can be characterized as significant reduction of the terminal relaxation time (τ) which is relevant to the chain exchange process between self-assembled domains.[33]

However, it was found that the Rouse model is not satisfactory when the overall conformation of bottlebrush polymer deviates from the cylindrical chain into the star-like chain (e.g., when side-chain is longer than the backbone).[49] Therefore, we chose poly(5-(perfluorooctyl)norbornene) (PF) having rather short side-chain ($-C_8F_{17}$) as model bottlebrush polymer to guarantee the cylindrical conformation and analyze the dynamics with regard to the Rouse model.[35] Since the fluoroalkyl side-chain dominates the molecular structure of PF (82 wt % of total polymer), it is reasonable to compare its relaxation properties with fluorocarbon polymers such as Teflon®.

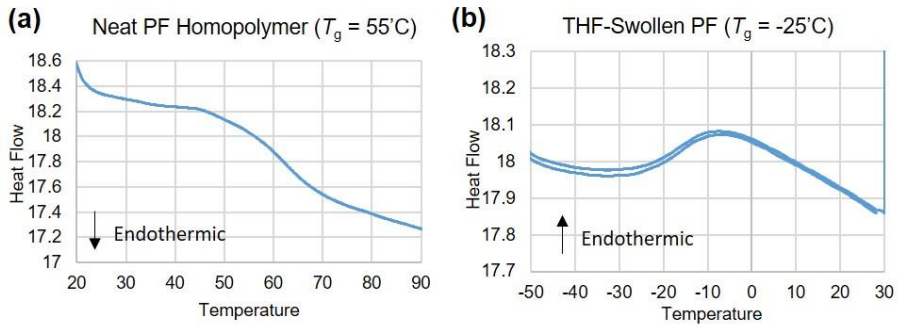

Figure 3.3. DSC thermogram of PF homopolymer (N = 500) measured with neat sample (a) and after saturation of THF vapor (b).

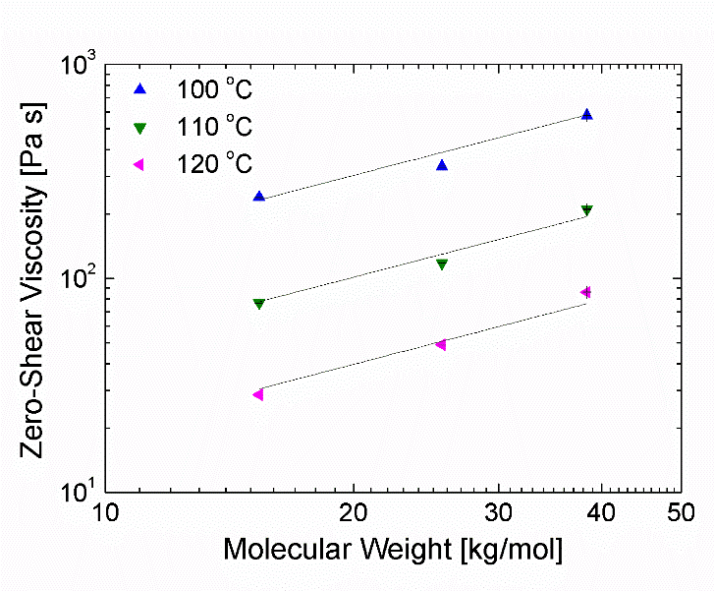

Figure 3.4. Zero-shear viscosity (η_0) vs molecular weight of PF homopolymers (M_{PF}), measured at three different temperatures. The solid lines indicate linear scaling, i.e., $\eta_0 \sim M_{PF}$.

Hereafter, we focus on the relaxation dynamics of melt PF bottlebrush polymer. Rheological measurements were made with pristine PF polymer at temperature (T) above T_g (T - $T_g \geq 15$ K), where T_g = 55 °C was estimated using differential scanning calorimetry (DSC) (Fig. 3.3a). Unlike chemically similar semi-fluorinated polymers such as poly(perfluorooctylethyl methacrylate),[55] DSC thermogram shows that PF does not form liquid crystalline mesophase, which removes possible complication in further kinetic analysis. Zero-shear-rate viscosities (η_0) of PF at different temperatures well above T_g shows linear dependence on MW at the experiment range, which comply with the Rouse model in the absence of entanglement (Fig. 3.4). Thus, the critical entanglement MW (M_c) of PF should be higher than 40 kg/mol, much higher than reported M_c = 12.5 kg/mol of linear tetrafluoroethylene-hexafluoropropylene copolymers (FEP).[56] Furthermore, temperature dependence of η_0 is fitted to the William-Landel-Ferry (WLF) equation, which is

$$\log a_T = \log (\eta_0(T)/\eta_{0,ref}) = C_0 - C_{1,g}(T - T_g)/(C_{2,g} + T - T_g) \quad (3.10)$$

where a_T is the shift factor, $\eta_{0,ref}$ is the zero-shear-rate viscosity measured at the reference temperature of 90 °C, $C_0 = \log (\eta_{0,ref}/\eta_{0,g})$, and the subscript g denotes variables at T_g. Figure 3.5 shows great quality of the fit giving the numerical constants $C_{1,g}$ = 8.83 and $C_{2,g}$ = 71.2 K, from which the fractional free volume and the flow activation energy at T_g (f_g and $E_{flow,g}$, respectively) are determined as $f_g \simeq \ln 10 \times C_{1,g} = 0.049$ and $E_{flow,g} = \ln 10 \times (C_{1,g}/C_{2,g})RT_g^2$ = 255 kJ/mol, where R is the ideal gas constant. It is noticeable that f_g of PF has much higher than FEP (f_g = 0.027) or the "universal" value for the linear polymers (0.025).[56, 57] The abundance of free volume in PF endowed by the bottlebrush architecture further leads to the lowering of T_g and $E_{flow,g}$ than FEP (T_g = 96 °C and $E_{flow,g}$ = 614 kJ/mol, respectively).[56] Remarkably, Pulamagatta *et al.* also observed similar T_g depression of 55 K upon tethering perfluoroalkyl

side-chain at the polynorbornene backbone.[58] Thus, these dynamic characteristics are common nature of bottlebrush polymers as mentioned, which will lead to significantly faster "internal" relaxation of the PF block in self-assembled domains compared to the linear analogs.

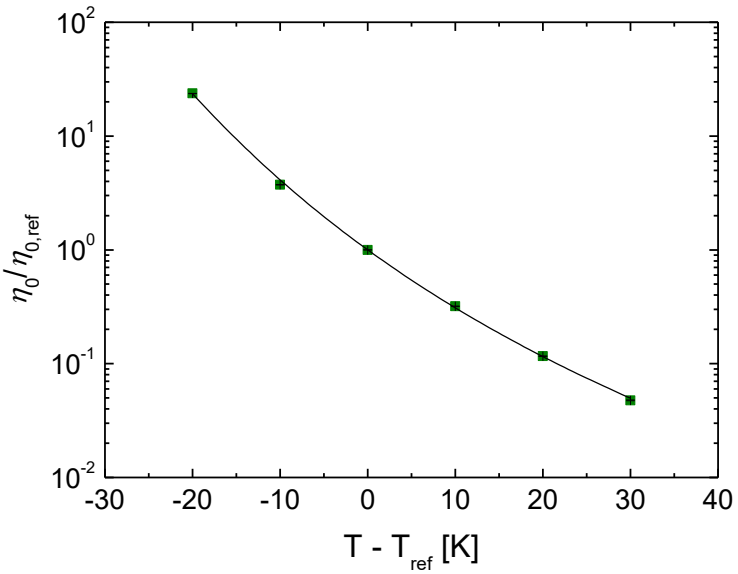

Figure 3.5. Shift factor, $a_T = \eta_0(T)/\eta_{0,ref}$, vs temperature ($T$) with respect to the reference temperature (T_{ref} = 90 °C) for PF melts. The solid line is the best fit to the WLF model (eq 3.10).

3.3.2. Dynamics of chain exchange in block copolymer micelles with bottlebrush core block

Studies on self-assembly kinetics of block copolymers in selective solvents can be broadly divided as the part of equilibrium dynamics and the other part, i.e., non-equilibrium kinetics including the growth, fusion and fission, and dissociation of the self-assembled aggregates. Herein, we describe the chain exchange dynamics of PF-*b*-PC (bottlebrush-linear) block copolymers at quasi-equilibrium, which means that the time-dependent change in aggregate structure is negligible during the experiment. To ensure such condition, we prepared a pair of differently labeled block copolymers with either proton (h) or deuterium (d), namely, PF-*b*-hPC and PF-*b*-dPC. The structural equivalence of spherical micelles assembled from either polymer was previously confirmed using small-angle X-ray scattering (SAXS).[35]

From the previous work, it was also found that a considerable amount of solvent THF swells the PF core (volume fraction of solvent in the core, $\phi_{solv} \simeq 0.2$), despite that THF is bad solvent for PF. Thus, the plasticizing effect of infiltrated solvent should be considered to analyze the internal relaxation of the core block. From the DSC thermogram of PF saturated with THF vapor we characterized effective T_g ($T_{g,eff}$) of $T_{g,eff} = -25$ °C, which is 80 K lower than T_g of neat PF (Fig. 3.3b). Such large depression of T_g was already observed in some block copolymer micelle systems[41, 59] and is thought to occur generally in weakly segregating block copolymer solutions.

The dynamics of chain exchange can be roughly decoupled into two independent contributions, the internal relaxation which is characterized by τ and the energy penalty for the pull-out of chain from the parent domain (i.e., the core) characterized by the extraction activation energy, E_{ext}.[33] We use the Rouse time (τ_R) as the appropriate choice of τ for kinetic analysis, since the

molecular weight of PF core block (M_{PF}) in this study is 46 kg/mol, which is expected to be lower than M_c ($\gg$ 40 kg/mol). Since the chain extraction is exponentially slowed down by $E_{ext} \sim \chi N_{core}$, the lifetime of chain extraction $\sim \tau_R \exp(E_{ext}/k_BT)$ is a stiff function of N_{core}, where N_{core} is N of the insoluble "core" block (or, the "minor" block in case of the bulk self-assembly) and k_B the Boltzmann constant. Thus, N_{core} effect overwhelms other contributions such as the crowding effect of corona chains and the intrinsic viscosity of polymer micelles.[60, 61] Due to the lack of chain exchange data from the fluorocarbon-based self-assembly, our data will be compared to one of few existing experiments which report values of E_{ext} corresponding to ours.

For the complete and quantitative understanding of the chain exchange process in PF-*b*-PC micelles, we conducted time-resolved small-angle neutron scattering (TR-SANS) experiments following the previously established method.[62] Scattering length densities (SLDs) of each component were first measured from a series of SANS with contrast variation of the solvent SLDs (Table 3.2). Then, isotopic mixtures of PF-*b*-hPC and PF-*b*-dPC in solvent media of zero-average SLD contrast (i.e., SLD of media was matched to the average of hPC and dPC.) were macroscopically homogenized for few seconds and then inserted in a sample stage at preset temperature. SANS data were collected consecutively with time resolution of 5 min and transformed to the relaxation function, $R(t)$, via eq 1. $R(t)$ is the proportion of a polymer chain that remains "unextracted" at the parent micelle after mixing time t, hence in the ideal case of perfectly uniform chain length it is expressed as the single exponential decay function of t with the lifetime corresponding to the chain extraction.[63] However, polydispersity in the chain length reshapes $R(t)$ curves displayed in Figure 3.6 into linear-log relationships which have been typically encountered in block copolymer systems.[33, 64]

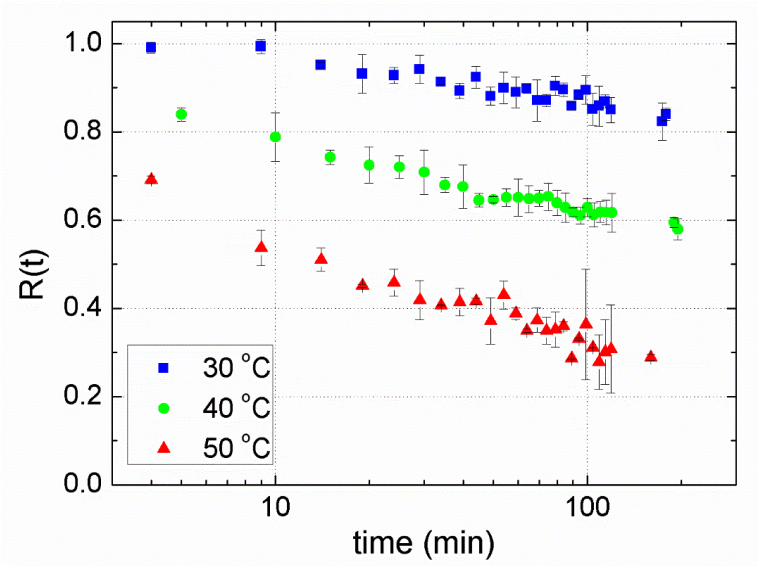

Figure 3.6. Relaxation function, $R(t)$, calculated from TR-SANS experiments using mixtures of PF90-hPC and PF90-dPC micelles at three different temperatures.

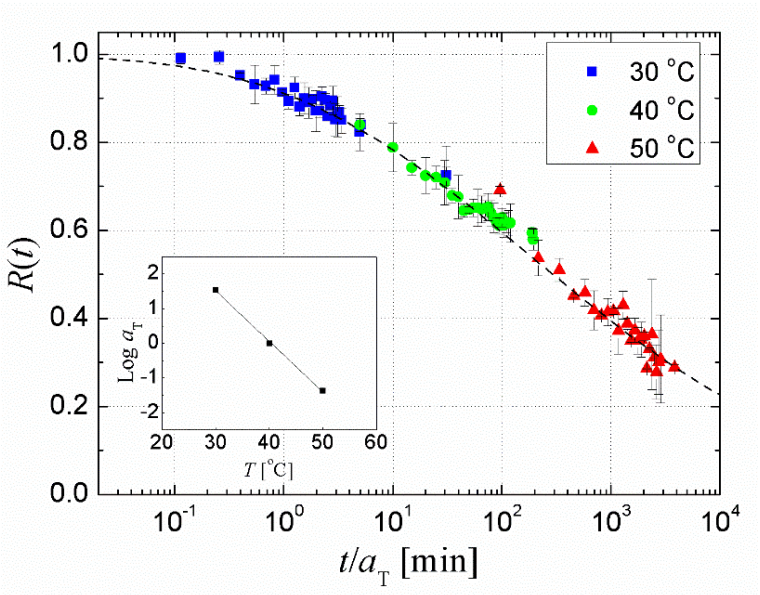

Figure 3.7. Time-temperature superposed relaxation function from PF90-PC with the reference temperature, T_{ref} = 40 ºC. a_T is the shift factor to T_{ref}, and the linearity of log(a_T) over T was shown in the inset. The dashed line was calculated with fixed polydispersity of the core block, M_w/M_n = 1.05.

It is not surprising that the chain relaxation is active at temperatures below T_g of neat PF (55 °C) since the penetrated solvent plasticized the core block as mentioned. The lowering of $R(t)$ with increasing T is clearly shown, implying that the internal core block relaxation is accelerated at higher T. As a result, $R(t)$ asymptotically approaches 0 after $t \sim 10^3$ min at 50 °C which demonstrates rapid equilibration of micelles.

These $R(t)$ curves at different temperatures also nicely overlap after lateral shifting, which allowed time-temperature superposition for the reference temperature (T_{ref}) of 40 °C (Fig. 3.7). However, the obtained apparent shift factors were not the same as those measured in the PF melts, and this discrepancy is also attributed to the presence of plasticizing solvent in the core. Then, the time-temperature superposed data is analyzed with an established model which incorporates the polydispersity of core block:

$$R(t, N_{\text{core}}) = \int_0^\infty P(N)K(t,N)dN \tag{3.10}$$

where $P(N)$ is the distribution function of PF core block repeat units with has the number average $N_n = N_{core}$, and $K(t, N)$ is the time correlation function for a PF block with length N. We adopted Schulz-Zimm distribution of core block chain length,

$$P(N_i) = \frac{z^{z+1}}{\Gamma(z+1)} \frac{N_i^{z-1}}{N_n^z} \exp\left(-\frac{zN_i}{N_n}\right), \tag{3.11}$$

where $z = [(N_w/N_n) - 1]^{-1}$ and Γ is the gamma function, and applied the Rouse dynamics and N^1-scaled energy barrier to describe the independent kinetic modes in micellar exchange,

$$K(t,N) = \exp\left[-\frac{t}{\tau_R} exp(-\varepsilon_{\text{ext}})\right], \tag{3.12}$$

Table 3.3. TR-SANS fitting results

Sample code	$M_{n,core}$ [kg/mol][b]	$T_{g,eff}$ [°C][c]	T_{ref} [°C][d]	$T_{ref} - T_{g,eff}$ [°C]	$\zeta_{ref} \times 10^8$ [N s/m][e]	N_w/N_n[f]	α [-][f]	ε_{ext} [-][f]
PF90-PC	44.8	-25 (16)[g]	40	65 (24)[g]	1.07	1.05	0.39	17.6
PS-PEP-2[a]	44.6	70	125	55	1.71	1.04	0.042	17.3

[a] Ref. [1] [b] Arithmetic mean of core blocks from protonated and deuterated block copolymers. [c] Effective T_g of the core block at the swollen state by solvent. [d] Reference temperature for time-temperature superposition. [e] Effective ζ of the core block at T_{ref} at the swollen state by solvent. [f] Fit parameters. [g] Corrected values using T_g of linear fluorocarbon polymer FEP from ref. [15].

where τ_R is given by $\tau_R(N) = (N^2b^2\zeta)/(6\pi^2k_BT)$,[65] and the dimensionless activation energy, ε_{ext}, was assumed $\varepsilon_{ext}(N) = \alpha[\chi - 0.5]N$ with the $O(1)$ prefactor α.[47, 66] Considering the T_g depression of 80 K, the monomeric friction coefficient ζ of swollen PF core at T_{ref} = 40 °C is calibrated to ζ at 120 °C for neat PF,[67] which is in turn estimated using the relationship for Rouse chain, $\zeta = 36m_o\eta_0/\rho N_A N b^2$, where m_o is the molecular weight of repeat unit, ρ the density of PF, N_A the Avogadro constant, and b the segment length, and previously obtained WLF relation (eq. 2).

Time-temperature superposed data was fit by the model with two fitting parameters, ε_{ext} and the polydispersity (N_w/N_n), where the results are summarized in Table 3.3. It was turned out that ε_{ext} of the present system is considerable (ε_{ext} = 17.6) and the fitting parameter α = 0.39 is located within previously reported range of $0.19 \leq \alpha \leq 0.6$,[33, 68]. The polydispersity of PF core block, included as another fitting parameter, is in excellent agreement with our independent characterization using PF homopolymer (N_w/N_n = 1.05), thereby suggesting a good reliability of the results. Judged by the set of parameters (M_{core} and ε_{ext}) listed in Table 3.3, poly(styrene-*b*-ethylene-*alt*-propylene) (PS-PEP) in liquid hydrocarbon serves as corresponding linear counterpart for the present study which uses bottlebrush core block.[33] Although T_{ref} of two experiments greatly differ by 85 K, the relaxation spectra of two examples coincide in striking resemblance, which is predominantly attributed to the lowering effect of bottlebrush architecture on T_g of PF.

For the fair comparison, the PF-*b*-PC data can be rescaled to T_{ref} = 71 °C to match $T_{ref} - T_{g,eff}$ = 55 K, where the correction for $T_{g,eff}$ of PF is made ($T_{g,eff}$ = 16 °C) to account for the lowering effect of bottlebrush, then by using shift factor obtained via eq. 2 it can be shown that the chain exchange of PF core

block is roughly 40 times faster than PS core block, completely owing to the accelerated internal relaxation. Thus, within the framework of Rouse dynamics, it is revealed that bottlebrush architecture in the core block can boost up the rate of chain exchange in several orders if all other things are equal.

3.4. Summary

In the present study, We presented relaxation dynamics of bottlebrush polymer PF with densely grafted fluoroalkyl side-chains in melts and in non-solvent where PF segregates to form the core of spherical micelles. Especially, molecular exchange dynamics between self-assembled domains of bottlebrush core block is thoroughly characterized using contrast-matched TR-SANS techniques for the first time. Thermal and rheological analyses inform that PF has typical characteristics of bottlebrush polymers such as the increase in M_e and f_g, which turns into the lowering of T_g and $E_{flow,g}$, as compared to the linear fluorocarbon polymers. Relaxation functions, $R(t)$, for the mixture of isotopically labeled PF-*b*-PC block copolymers at three different temperatures allow accurate and quantitative interpretation of the chain exchange kinetics based on the Rouse model. From the comparison with the linear block copolymer (PS-PEP) having similar activation energy of core block extraction, our result suggests that introducing bottlebrush architecture at the core block brings about 40 times faster chain exchange due to the acceleration of internal relaxation. This finding supports the current concept of using bottlebrush block copolymers for self-assembly of larger domains, and it is expected that further optimization on the side-chain length would realize the rapid self-assembly of ultra-high MW block copolymers.

Chapter 4.* Nanocomposite Formation through Interactions Between Block Copolymer Micelles and Crystallizing Minerals

4.1. Introduction

Superior physical properties of biominerals, which is essential for the survival of life, stem from hybrid nanostructures of minerals and proteins.[69] For instance, nanostructure of bone is made of collagen fibrils and hydroxyapatite nanocrystals, and is assembled with the help of phosphorylated non-collagenous proteins (NCPs) *in vivo*.[70, 71] Strongly charged NCPs, which have few 10-100 kDa, are known to inhibit crystal growth outside the fibril and ultimately guide co-assembly of collagen-hydroxyapatite complex.[72-74] Another important example of biominerals, nacre, consist of aragonite plates interlayered with anionic proteins and chitin.[75] Numerous studies on biomineralization have focused on the role of polyelectrolyte mimicking such charged proteins, including the ability of crystal morphing or growth inhibition.[76-78] However, much less have been known about the dynamics of the interaction between polyelectrolyte and minerals, such as the adsorption of

* This chapter is based on paper from S. Kim, J. Choi, M. Lee, S.-H. Choi, and K. Char, , *Chem. Mater.* (2018), **30**, 4048-4055.

polyelectrolyte onto the surfaces, which could affect the kinetic pathway of crystallization and consequently the nanostructures of polymer/inorganic hybrids.

Earlier investigations on bio-inspired hybrid assemblies have focused on the interference of linear charged polymers (i.e., polyelectrolytes, PEs) on the crystal growth.[79-82],[76, 83, 84] Since the electrostatic interaction between the crystal surface and PEs are enhanced with increasing charged fraction (i.e., the degree of ionization) of PEs, the adsorption of highly charged PEs often retards or even inhibits the growth of crystals by blocking the growth site on the crystal surface. In addition, the retardation of the crystal growth becomes more significant when the PEs are interacting with polar crystal surface that can possess alternating net surface charges. However, kinetic studies have mainly dealt with the macroscopic relationship between the adsorbed amount of PEs and the rate of ion consumption, which cannot differentiate the surface-specificity of the crystal growth.[85-87] In addition, the effect of PE molecular weight on the crystal growth is still controversial because both increasing and decreasing trends have been reported for the adsorbed amount of PEs with the molecular weight under the same mass concentration.[86-88]

Recently, the focus of such bio-inspired hybrids has been expanded from systems with linear PEs to the ones with charged particulate materials. The occlusion of organic particles into the crystals can provide enhanced toughness as nature does.[15, 89] Kim *et al.* documented the occlusion of submicron-sized polymeric beads and block copolymer micelles of which sizes are tens of nanometers within calcite crystals.[15, 90, 91] The growth inhibition of nanocrystals was also demonstrated by the dense adsorption of charged nanoparticles on the growing surface.[92] These reports suggest that the particulate materials can influence on the crystal growth by the adsorption and

growth retardation process.[93] However, the effect of material architecture including linear and particulate materials have not yet been systematically reported.

In this study, we investigated the effect of material architecture including linear or particulate macromolecules (e.g., chain length and particle size) on the growth retardation and the structural complexity of crystals by evaluating the kinetic factors as well as the thermodynamic factors. We employed linear poly(acrylic acid) (PAA) with different molecular weight and nano-sized spherical block copolymer micelles (BCMs) with various pairs of block weights assembled from polystyrene-*block*-poly(acrylic acid) (PS-*b*-PAA). These molecules and self-assembled particles have similar sizes with NCPs or globular proteins involved in biomineralization. Calcium sulfate hemihydrate ($CaSO_4 \cdot 0.5H_2O$) was used for model crystallizing material because of its well-defined columnar habit and its potentials for biomedical applications.[94-96] Unlike systems with slow crystal growth where the adsorption of polymers on the crystal surface is readily equilibrated, for the systems of sufficiently fast crystal growth such as evaporation-driven crystallization, the growth retardation is mainly governed by the diffusion process. Owing to the convective transportation of crystals toward boundary of the evaporating droplet, we could safely isolate crystals without interference of Ostwald ripening, which enabled precise and quantified analysis of the effect of PAA or BCM diffusion. The growth retardation for given PAA concentrations was found to be diminished when the diffusion of PAA is slow relative to the rate of crystal growth. The same diffusion-limited adsorption behavior was also found from the occlusion of adsorbing BCMs and the growing crystals. We believe that this study is the first systematic work for the kinetics of adsorption-

induced growth inhibition of polymers—spanning from linear chain to spherical particles—on the growing crystals.

4.2. Experimental Section

Materials. Calcium sulfate in hemihydrate form ($CaSO_4 \cdot 0.5H_2O$) was purchased from Sigma-Aldrich and used as received.

As linear homopolymers, four poly(acrylic acid)s (PAAs) with different molecular weight were purchased from Sigma-Aldrich (PAA2K and PAA12K), Polymer Source (PAA5K), and Polysciences (PAA50K). The PAAs were protonated and desalted by dialysis in HCl buffer followed by lyophilization, and further characterized by FT-IR (Frontier, Perkin-Elmer) to confirm the absence of PAA ionization (Figure 4.1).[97]

For the particulate polymer/inorganic system, three poly(styrene-*b*-acrylic acid)s (PS-*b*-PAA) with different pairs of molecular weights were prepared (see Table 4.1). Two were purchased from Polymer Source and used as received. (i.e., SAA19K and SAA84K). SAA73K was prepared by the hydrolysis of poly(styrene-*b*-*tert*-butyl acrylate) (Polymer Source).[98]

Table 4.1. Molecular Characteristics of PAA homopolymers and PS-*b*-PAA Diblock Copolymers

Sample code	PS *M* (kg/mol)	PAA *M* (kg/mol)	M_w/M_n
PAA2K	-	2.0[b]	1.36
PAA5K	-	5.0[b]	1.15
PAA12K	-	11.5[b]	1.33
PAA50K	-	50[b]	1.33
SAA19K	15[a]	4.3[a]	1.15
SAA84K	70.5[a]	13[a]	1.10
SAA73K	45[a]	28[a]	1.09

[a] Number-averaged molecular weights. [b] Weight-averaged molecular weights

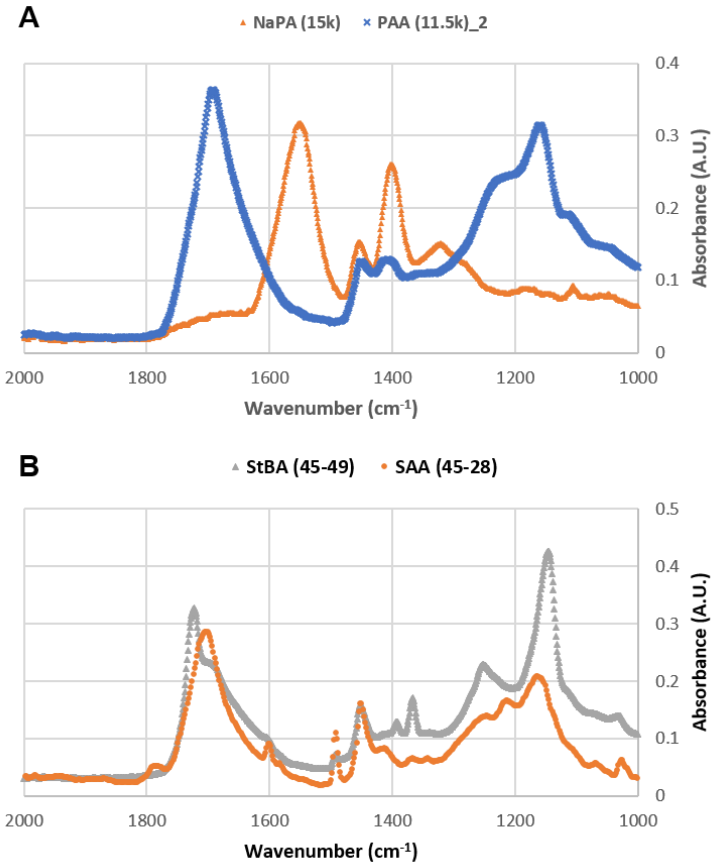

Figure 4.1. FT-IR characterization of (A) sodium polyacrylate (NaPA) before and after protonation, and (B) poly(styrene-*b*-tert-butyl acrylate) (StBA) before and after hydrolysis. Note the shift of main carbonyl peak from 1570 cm^{-1} to 1700 cm^{-1} in NaPA, and the reduction of double peaks within 1350-1400 cm^{-1} which is responsible for the methyl group of PtBA block.

Preparation and characterization of Block Copolymer Micelles (BCMs). 10 mg/mL of PS-*b*-PAAs were dissolved in N,N-dimethylformamide (DMF, Sigma-Aldrich) and subsequently micellized by the slow addition of 18 MΩ Milli-Q water for 1 h while vigorously stirred.[99] Then PS-*b*-PAA block copolymer solutions in water/DMF (50/50 v/v) were dialyzed several times with excess deionized water to remove DMF completely. Hydrodynamic radii of the BCMs dispersed in water were characterized by dynamic light scattering (DLS, Zetasizer Nano ZS90, Malvern). For DLS, the concentration of BCMs was fixed at 1.0 mg/mL.

Preparation and characterization of crystals. Precursor solutions were made by dissolving 0.2 mmol/L $CaSO_4$ and varied concentrations of either PAAs or PS-*b*-PAA BCMs in water/DMF solvent mixture (80/20 v/v). In addition, HCl or NaOH were added, if necessary, to tune pH of the solutions, and thus PAA ionization.

For the crystal preparation, a 0.1 mL droplet of the solution was cast on a UVO-cleaned silicon wafer (1.5 × 1.5 cm^2) and the solvent was evaporated at a target temperature. During evaporation, $CaSO_4$•$0.5H_2O$ crystals were nucleated and transported to the contact line of the droplet, due to the evaporation-induced coffee-ring flow. After complete solvent evaporation, the wafer was rinsed in DMF to remove impurities such as NaCl crystals, since $CaSO_4$•$0.5H_2O$ is not soluble in DMF.

The obtained crystals were characterized by field-emission scanning electron microscopy (FE-SEM; JSM-6701F, JEOL). SEM experiments were conducted with 10kV electron beam after Pt coating (20 mA, 90 sec) over the crystals deposited on the SiO_2 substrate. In addition, the focused ion beam (FIB; Auriga, Carl Zeiss) was used to obtain cross-sections of selected crystals. Ga-ion beam was implemented to produce the cross-section of the sample by

milling. The prepared cross-section was then characterized by SEM combined with the FIB apparatus.

The crystallinity and exposed crystal planes were analyzed by X-ray diffraction (XRD; New D8-Advance, Bruker) and selected area electron diffraction (SAED; JEM-2100 TEM, JEOL). XRD experiments were conducted with 40kV Cu Kα X-ray beam, in coupled theta-2theta (θ-2θ) mode. The specimens (crystals deposited on 1.5 × 1.5 cm^2 SiO_2 substrate) were mounted and diffraction patterns within $2\theta = 10\text{-}36^o$ range was scanned. This range was sufficient to discern the crystal phase of the sample, since two main peaks ($2\theta = 14.77^o$, 29.74^o) of $CaSO_4 \bullet 0.5H_2O$ (hemihydrate) were both detected. TEM experiments were conducted with 200kV electron beam illuminated on the sample crystals which were transferred onto lacey carbon film. Brightfield images and selected area electron diffraction (SAED) were collected in conventional TEM mode. Also, The organic content of occluded BCMs within crystals were characterized by energy-dispersive X-ray spectroscopy (EDS; X-MAX 80T, Oxford, installed in JEM-2100 TEM, JEOL). EDS experiments were performed in scanning-TEM (STEM) mode.

The solubilities of $CaSO_4 \bullet 0.5H_2O$ at various water/DMF compositions were characterized by colorimetric EDTA titration with Eriochrome Black T as an indicator.[100]

Estimation of the onset point of crystallization induced by the solvent evaporation. The onset point of crystallization was estimated by combination of in-situ droplet contact angle measurement and calculation of the change of solvent composition during evaporation of water/DMF mixture solvent. The principle is characterization of the pinning of the droplet which is induced by initiation of the crystallization. Since $CaSO_4 \bullet 0.5H_2O$ crystals formed at the contact line prohibit the recession of the evaporating droplet, the droplet is

"pinned" whereafter crystallization begins. The pinned droplet continues evaporation, thereby the contact angle of droplet starts to decrease. From in-situ monitoring of contact angle from an evaporating droplet, we could characterize the onset point of crystallization (Figure 4.2a). Also in-situ monitoring gives the information of droplet dimensions, from which the remaining volume of the droplet is determined. This is based on the spherical cap model of sessile droplet, which tells that $V = \pi h(3a^2 + h^2)/6$ where $V(t)$ is the volume, a is the radius, and h is the height of the droplet. In the present study, the onset point was found to be where 66% of the initial solvent was evaporated (by volume). We related the reduction of the droplet volume and the change of solvent composition by the effusion rate law. In a simple word, the rate of effusion is proportional to the vapor pressure (ΔP) and $m^{-1/2}$ where m is the mass of the molecule. Thereby we could construct the rate of volume reduction for each component (i.e., water or DMF) with the equations

$$-\frac{\mathrm{d}V_w}{\mathrm{d}t} \sim \frac{\Delta P_w \mathrm{A}}{m_w^{\frac{1}{2}}}\varphi_w \quad (4.1a), \quad -\frac{\mathrm{d}V_{DMF}}{\mathrm{d}t} \sim \frac{\Delta P_{DMF} A}{m_{DMF}^{\frac{1}{2}}}\varphi_{DMF} \quad (4.1b)$$

,

where $V_w(t) = \varphi_w V$, $V_{DMF}(t) = \varphi_{DMF} V$, $\varphi_w(t)$ and $\varphi_{DMF}(t)$ are the volume fraction of water and DMF in the mixed solvent, respectively. Variable t could be further reduced, and the correlation between V_w and V_{DMF} is expressed by

$$\frac{\mathrm{d}\ln V_\mathrm{w}}{\mathrm{d}\ln V_\mathrm{DMF}} = \frac{\Delta P_w}{\Delta P_{DMF}}\sqrt{\frac{m_\mathrm{DMF}}{m_w}} \quad (4.2)$$

which quantitatively describes the change of solvent composition during evaporation (Figure 4.2b). Here, the proportion of evaporation (i.e., 66% by volume) corresponds to $\varphi_w = 0.5$, which is the onset point of crystallization in terms of the solvent composition.

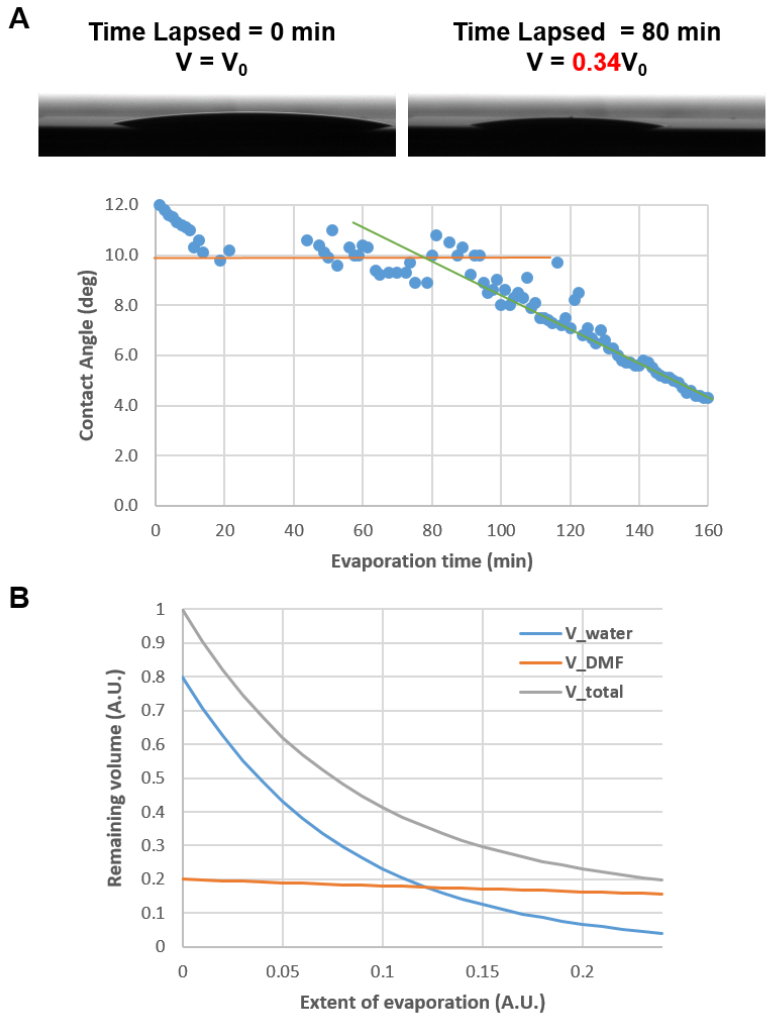

Figure 4.2. Estimation of the onset point of crystallization induced by the solvent evaporation. (A) Snapshots from optical *in-situ* monitoring of an evaporating droplet, and time evolution of the contact angles during evaporation. Initiation of the droplet pinning was determined as the intersection of constant contact angle mode (orange) and pinned mode (green). Lines are guide to an eye. (B) Change of the droplet composition during evaporation calculated from eq 4.2.

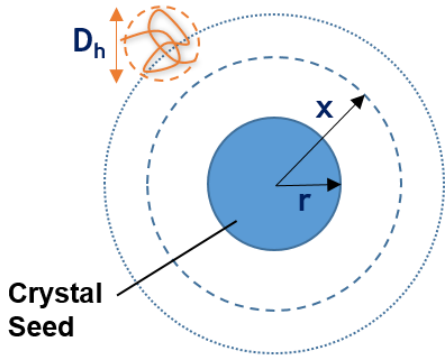

Figure 4.3. Schematic representation of geometry for a growing isotropic crystal seed of radius *r* and a diffusing polymeric molecule with hydrodynamic diameter D_h.

Derivation of diffusion-limited adsorption models for PAA and PS-*b*-PAA BCMs. Following argument on diffusion-limited crystal growth by Sugimoto, the radial flux of ions (J) toward a spherical crystal nucleus can be expressed as $J = 4\pi D r_{nucl} c_0$, where, D is diffusivity of ion, r_{nucl} is radius of nucleus and c_0 is the bulk concentration of ion far from the nucleus (Figure 4.3).[2] Even though the model describes 'adsorption' of ions, it allows equivalent description of the adsorption of polymers. We slightly modified this expression to take into account differing sizes of individual chain, defining the areal flux of PAA cross-section, $I_A = J \times \pi R_h^2 = 4\pi^2 r_{nucl} n_p D R_h^2$, where n_p is the concentration of polymer chain. Here, R_h and D, both characteristics of the polymers, are assumed to have scaling relation with the molecular weight M ($R_h \sim M^v$ and $D \sim (k_b T/\eta) R_h^{-1}$). The scaling exponent v needs to be determined carefully in the present system since polyelectrolyte conformation in less polar solvent tends to be different from that in water. In this work we estimated $v = 0.414$ for PAA chains using dynamic light scattering (DLS). The assumption

simplifies molecular weight dependence of the flux, $I_A \sim n_p(k_bT/\eta)M^v$. We further defined the critical PAA concentration as the mass concentration ($C_{crit,PAA} = n_{crit,PAA}M$) for breakdown of the crystallinity (see section 3.2 of main text), and assumed that the flux I_A* at which the breakdown occurs is solely determined by the competition with growth rate of crystal surface, and therefore irrelevant of the PAA molecular weight. Putting all things together and considering only the characteristics of polymer, we conclude that $I_A^* \sim n_{crit,PAA}(k_bT/\eta)M^v \sim (k_bT/\eta)C_{crit,PAA}M^{v-1}$, and therefore $C_{crit,PAA} \sim (\eta/k_bT)M^{1-v} \sim M^{0.6}$.

In the case of the block copolymer micelle (BCM) adsorption, the characteristics were simply presented with the Stokes-Einstein equation ($D \sim R_h^{-1}$) where R_h is hydrodynamic radius of the BCMs. We directly applied the abovementioned model to take into account differing R_h, defining the areal flux of the BCM cross-section, $I_A = J \times \pi R_h^2 = 4\pi^2 r_{nucl} D N_{BCM} R_h^2$, where N_{BCM} is the number concentration of BCMs. Assumption of the Stokes-Einstein equation gives $I_A \sim N_{BCM}R_h$. We defined the critical BCM concentration ($N_{crit,BCM}$) as the number concentration for the frustration of the hexagonal facets (see section 3.3 of main text), and further assumed that the frustration occurs at the areal flux I_A*, which is solely determined by the competition with growth rate of crystal surface, in the same manner as the growth inhibition of PAA. Thus, $I_A^* \sim (N_{crit,BCM})R_h$, which produces $N_{crit,BCM} \sim R_h^{-1}$.

4.3. Results

4.3.1. Nucleation and growth of $CaSO_4$•0.5H_2O crystals in evaporating droplets

In this study, mineral $CaSO_4$ was selected as the model crystallization system. Bulk $CaSO_4$ were dissolved in the solvent mixtures of water and DMF in the presence of macromolecular additives, such as PAA and PS-*b*-PAA BCMs. Crystallization of $CaSO_4$ was driven by the evaporation of the water/DMF mixture solutions, where the rates of crystal growth could be controlled easily and reproducibly. Figure 4.4 shows the schematic process of solvent evaporation from a droplet of precursor solution cast on SiO_2 substrates at 30°C. The solvent evaporation generated radially diverging flow (i.e., "coffee-ring flow") toward the contact line when the droplet was pinned, and therefore the nucleated crystals were transported toward the contact line.[101] After the complete solvent removal, crystals were deposited periodically as shown in Figure 4.4b due to the repeated pinning and continuous recession of the droplet.[102] The resulting crystals had uniform shape and sizes due to the absence of Ostwald ripening, since any molecular transport to the crystal was terminated after the contact line receded over the deposited crystals.

The crystal structure was confirmed from XRD analysis to be $CaSO_4$•0.5H_2O (hemihydrate) although $CaSO_4$•2H_2O (dihydrate, or gypsum) phase is thermodynamically more stable. This is because the kinetics of phase transformation from metastable hemihydrate to gypsum was suppressed due to the facts including low contact angle of the droplet and high non-aqueous solvent (i.e., DMF) content.[103, 104] The characteristic hexagonal column shape of prepared $CaSO_4$•0.5H_2O crystals in the absence of interfering macromolecular additives was observed from SEM (Figure 4.4c). The onset of

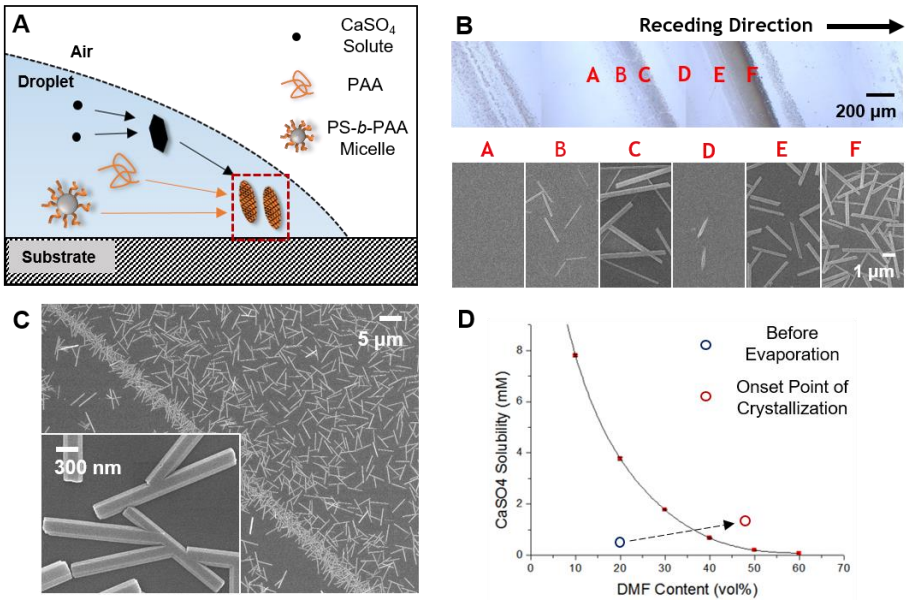

Figure 4.4. Schematic illustration of the evaporation process for the crystallization of $CaSO_4$. (A) A droplet of aqueous/DMF $CaSO_4$ solution containing either PAA or PS-*b*-PAA BCMs is cast on a substrate and let evaporated. (B) The crystals formed are transported to the contact line by the coffee-ring flow and deposited on a substrate through the recession of solution. (C) The characteristic lines of deposited crystals due to the periodic recession of droplet. (D) Both of $CaSO_4$ concentration and DMF fraction increase as the droplet is evaporated (an arrow from the blue circle). After the concentration of $CaSO_4$ exceeds the solubility limit, the solution undergoes the metastable period followed by the onset of crystallization, near DMF ~ 50 vol% (red circle).

evaporation-induced crystallization is sketched in the $CaSO_4$ solubility diagram constructed from EDTA titration method as a function of DMF content (Figure 4.4d). The vapor pressures of water and DMF at 30°C are 31.8 torr and 5.5 torr, respectively. Thus, as the evaporation proceeds, both the concentration of $CaSO_4$ and the DMF content in the solvent mixture increase, which leads to the nucleation and growth of the crystals.

Optical monitoring of the remaining droplet volume enabled rough estimation of the onset point, which was 50 vol% of DMF content for the evaporation initiated from 0.2 mmol/L $CaSO_4$ at DMF 20 vol%. After the initiation of crystallization, the system consumed free $CaSO_4$ ions at the expense of crystallization until the concentration of free $CaSO_4$ reached the equilibrium solubility. Thereafter, the system followed the solubility curve, so the reduction of remaining free ions was compensated with the growth of crystals.

4.3.2. Anisotropic adsorption and growth retardation of PAA

Poly(acrylic acid) (PAA), a negatively charged weak polyelectrolyte, was introduced during $CaSO_4$ crystallization. The aspect ratio of $CaSO_4 \cdot 0.5H_2O$ hexagonal columns was significantly reduced as the amount of added PAA was increased (Figure 4.5). In the absence of PAA, the growth along columnar *c*-axis is much faster than others since the polar {001} plane consists of alternating cation (Ca^{2+}) and anion (SO_4^{2-}) layers (Figure 4.6). As PAA has negative charges, the adsorption of PAA on $CaSO_4 \cdot 0.5H_2O$ crystals is the strongest on {001} plane when the surface exposes cations. The observed reduction of aspect ratio of the crystals suggests that PAA is predominantly

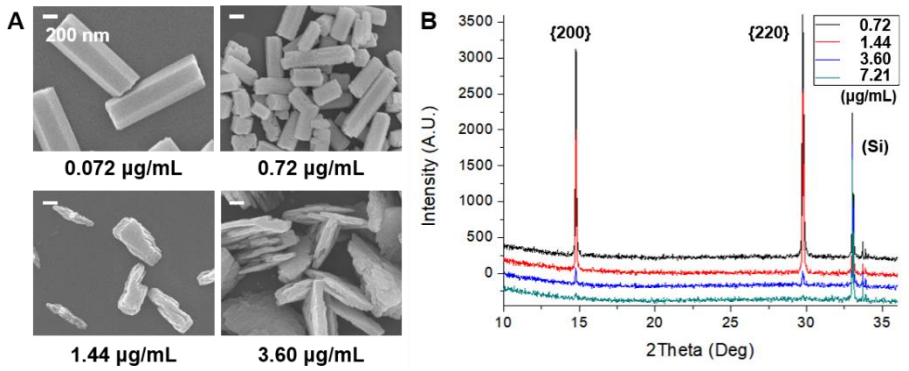

Figure 4.5. (A) Transition of crystal forms induced by the adsorption and growth interference of PAA2K in the crystallization of $CaSO_4$ hemihydrate. The amount of added PAA was varied, while the concentration of $CaSO_4$ was maintained at 0.2 mmol/L. (B) Corresponding X-ray diffraction patterns. The crystalline peaks sharply disappear at a PAA concentration of 7.21 µg/mL, where the crystals cannot develop their {200} and {220} hexagonal side facets. Background diffractions (ca. 33^0) from Si substrates are noted.

adsorbed at the cationic layer of {001} surface. Negatively charged PAA can interact with and adsorb onto such polar surfaces, and therefore hinder the growth of the specific plane.

The effect of PAA on the retardation of crystal growth was further characterized by XRD (Figure 4.5B). When the PAA2K concentration exceeds a certain critical level (ca. 7.2 µg/mL), crystalline peaks of {200} and {220} planes disappear, as these planes are responsible for the diffraction from the side faces of hexagonal column. (Note that selected area electron diffraction (SAED) data are shown in Figure 4.7) The decline of crystalline peaks was consistent with the reduction of the aspect ratio. Hence, we defined the critical PAA concentrations ($C_{crit,PAA}$) as the concentration where the crystallinity of {200} disappears.

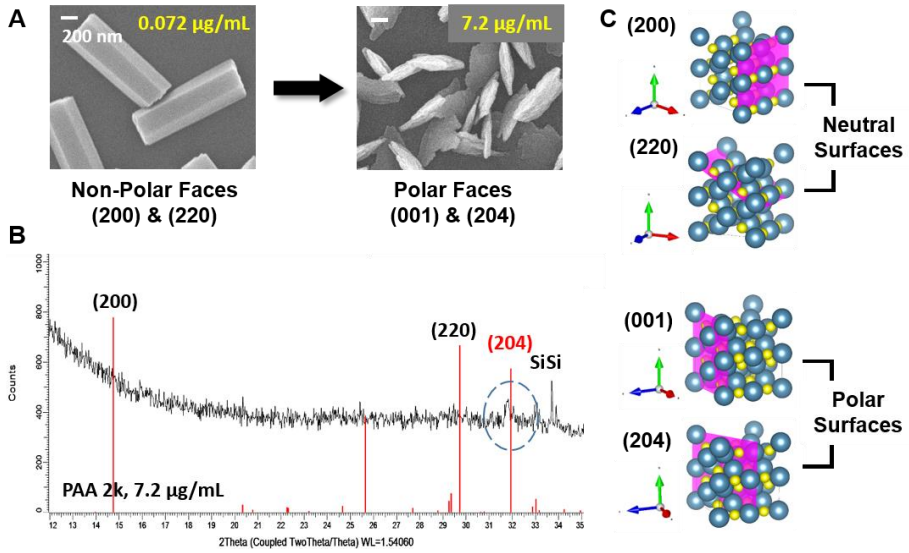

Figure 4.6. Shape modification effect of PAA due to the anisotropic growth retardation. (A) As the amount of added PAA is increased, the growth along polar [001] axis was severely retarded, while the growth along non-polar directions was relatively intact. Consequently, the dominant faces were converted from non-polar sides of hexagonal column to polar top and bottom. (B) Diffraction from polar {204} planes, a signature of growth retardation along the polar direction, was revealed from thin film X-ray diffraction on a Si substrate. It is noted that diffractions from the {200} and {220} planes, which were very intense in the absence of PAA, have disappeared. Red lines indicate typical diffraction peaks from $CaSO_4$ hemihydrate. (C) Detailed section of crystal planes (200), (220), (001), and (204) of $CaSO_4$ hemihydrate constructed by crystallography software VESTA. Calcium ion (Ca^{2+}) is denoted yellow, while sulfur atom of sulfate ion (SO_4^{2-}) is denoted blue.

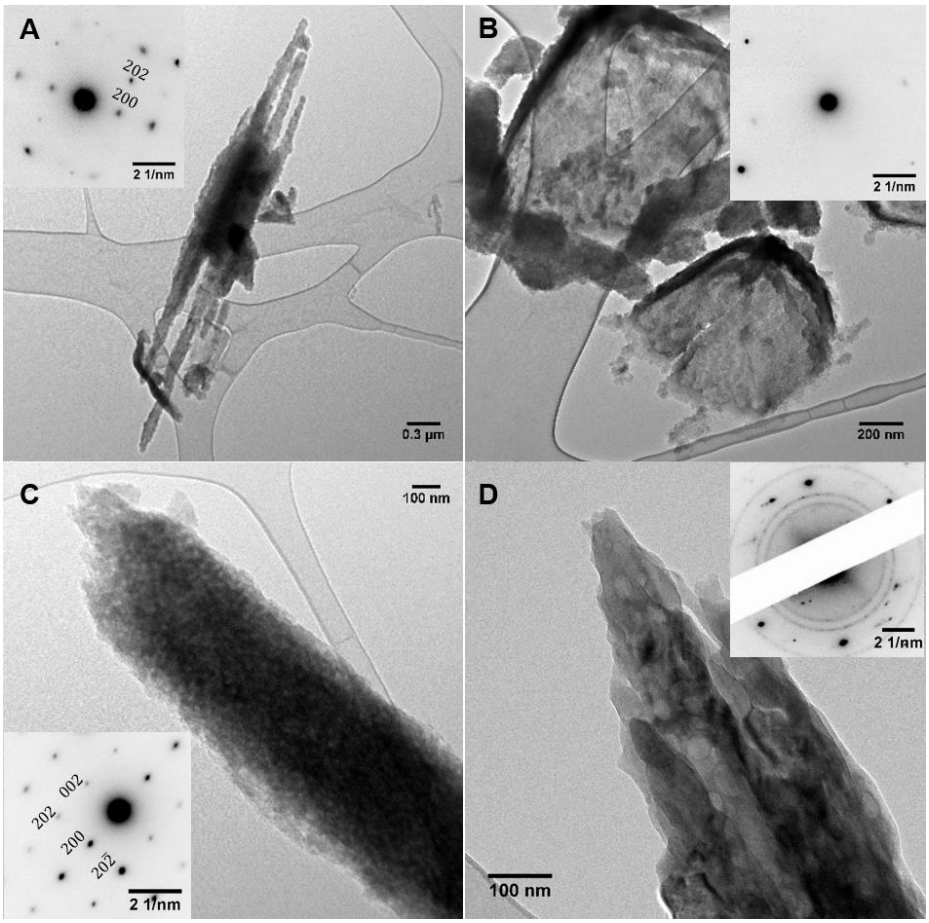

Figure 4.7. TEM images and corresponding selected area electron diffraction of $CaSO_4$ hemihydrate crystals in the presence of polymeric additives. (A, B) PAA5K additives with concentrations of 3.6 and 7.2 µg/mL, respectively. (C, D) SAA19K additives with number concentrations of 0.07 and 0.35 µmol/L, respectively. Above the critical polymer concentration, both PAA and SAA BCM inhibit the growth along *c*-axis, which is verified by the extinction of {200} diffraction. This is consistent with the XRD data.

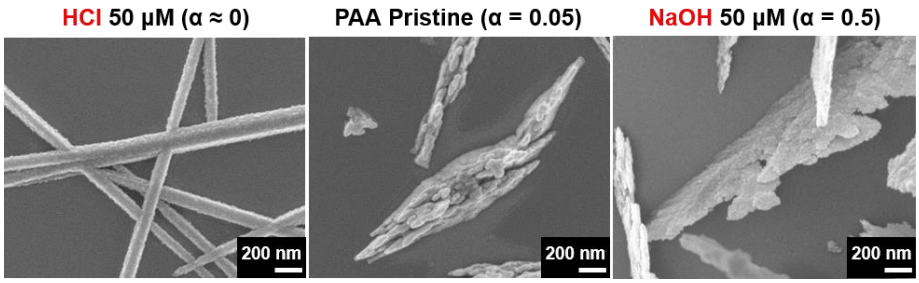

Figure 4.8. Effect of the degree of ionization (α) of PAA2K on the interference of $CaSO_4$ hemihydrate crystallization at a PAA concentration of 7.21 μg/mL. Series of α values were calculated for the solution at the onset point of crystallization (50 vol% of DMF).

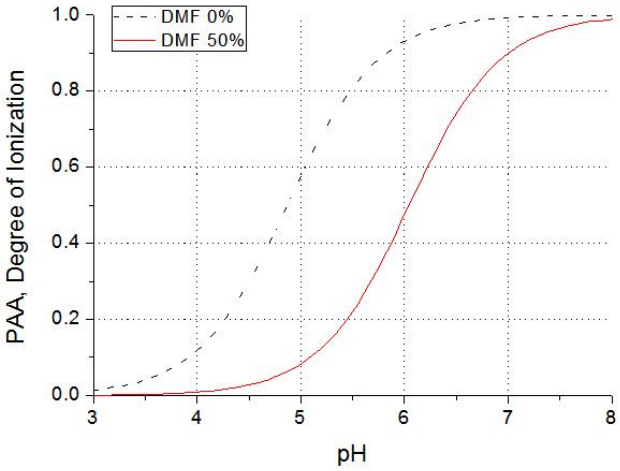

Figure 4.9. The pK_a of PAA in the water/DMF mixed solvents is higher than that in the aqueous solution ($pK_a \sim 4.5$) since the dissociation of carboxylic acid is more difficult in less polar media. Due to the lack of information for pK_a of PAA in the mixed solvents, pK_a of analogous propionic acid (~ 5.8) were taken for the construction of degree of ionization curves.[3] The dotted line represents the degree of ionization (α) of PAA in aqueous solution, and the red line represents α in a water/DMF mixed solvent (50/50 v/v). Change of the activity of water was considered for the calculation of acid-base equilibrium in the mixed solvents.

The adsorption of PAA is based on electrostatic interaction, thereby can be controlled with the degree of ionization (α) of PAA. As a result, in Figure 4.8, the crystal shape largely depends on the α of PAA, which was tuned by pH of solvent (Figure 4.9). Without added salts, PAA at the onset point (i.e., 50 vol% of DMF) has a small fraction of charge ($\alpha \approx 0.05$) but it is sufficient to induce the preferential adsorption of PAA on the polar surfaces and the subsequent shape transition. The shape of crystals is much closer to thin sheets exposing PAA-adsorbed polar planes when $\alpha \approx 0.5$ (0.5 equiv. NaOH of acrylate repeating unit was added). In contrast, the addition of 0.5 equiv. HCl almost eliminates dissociated fraction of PAA ($\alpha \approx 0$), thereby shuts off the adsorption and consequent growth retarding effect of PAA.

Furthermore, the effect of molecular weight of PAA (M) on the crystal shape transition was studied. The increase in the molecular weight of PAA weakens the effect of adsorption and shape transition (Figure 4.10 and Figure 4.11). Compared with the case of PAA2K, the crystals formed in the presence of PAA12K and PAA50K show less perturbed columnar shape. $C_{crit,PAA}$ as a function of molecular weight between 2 kg/mol to 50 kg/mol was carefully measured using XRD as shown in Figure 4.10B. We found the scaling relationship between $C_{crit,PAA}$ and the molecular weight of PAA as $C_{crit,PAA} \sim M^{1-\nu}$, where ν is the Flory-Huggins exponent which was determined by DLS experiments ($R_h \sim M^{\nu}$). Herein ν was found to be 0.414, since the Ca^{2+} ions present in the solution bound to and weakly condensed the charged PAA (Figure 4.12). This scaling relationship will be discussed in detail in the following sections.

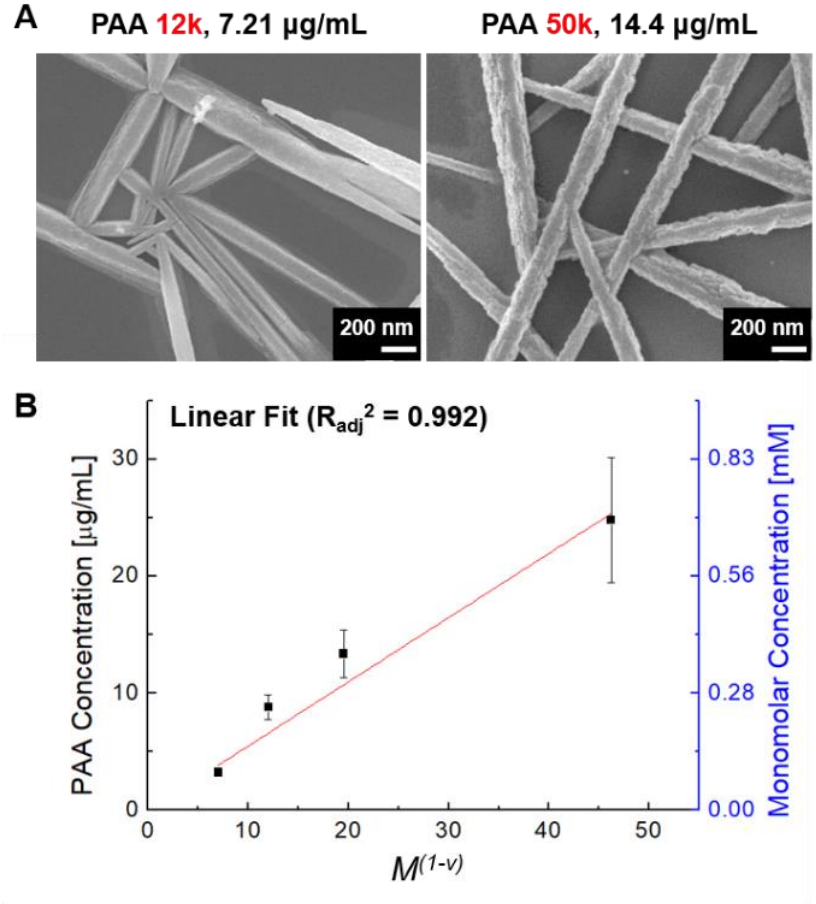

Figure 4.10. Effect of the PAA molecular weight on the interference of $CaSO_4$ hemihydrate crystallization. (A) PAA12K and PAA50K did not effectively interfere the crystallization of $CaSO_4$ hemihydrate when compared with shorter PAAs, e.g., PAA2K. (B) Critical PAA concentrations ($C_{crit,PAA}$) at which the crystalline peaks disappear showed linear dependence with $M^{1-\nu}$, where M is the molecular weight of PAA, and ν is the Flory-Huggins exponent.

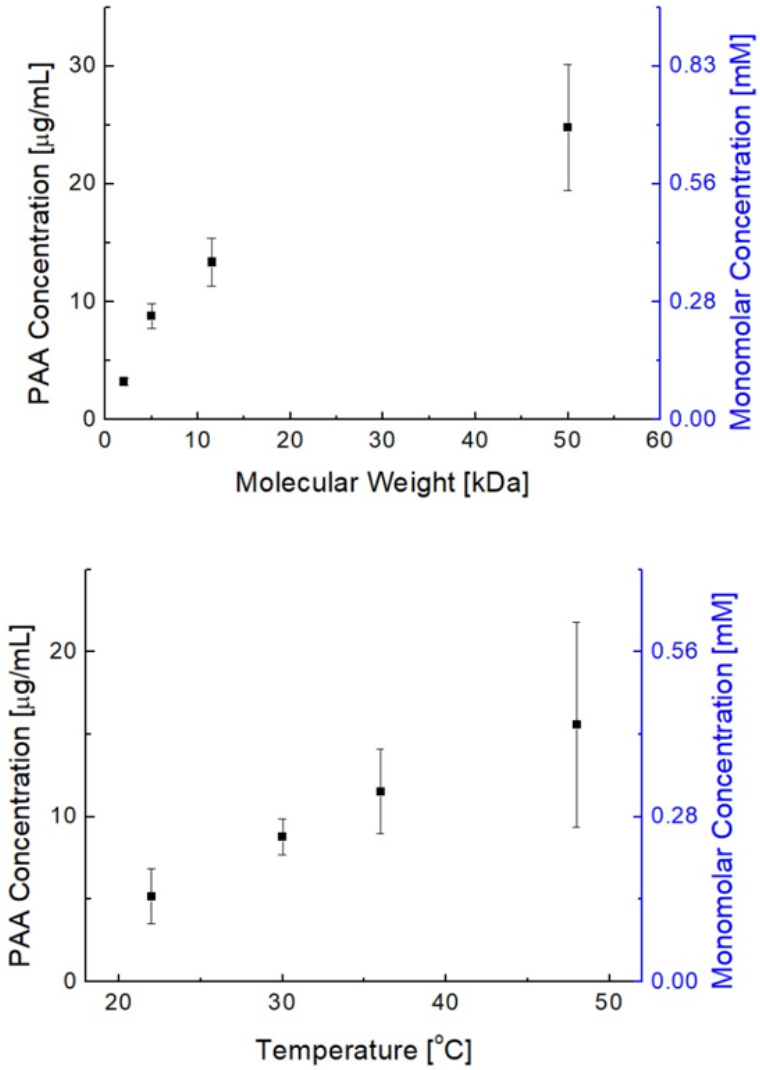

Figure 4.11. The critical PAA concentration as a function of PAA molecular weight at 30 ºC and evaporation temperature with PAA5k.

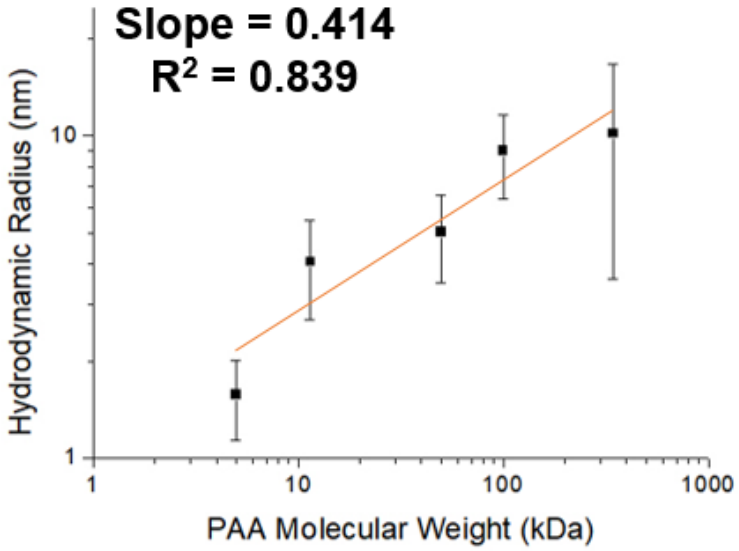

Figure 4.12. Log-log plot of the hydrodynamic radius (R_h) versus PAA molecular weights. R_h with 5 different molecular weights were measured by the dynamic light scattering. Solvent was matched with the appropriate condition of the solution at the onset point of $CaSO_4$ hemihydrate crystallization (i.e., the water/DMF mixed solvent (50/50 v/v)). Also, the amount of Ca^{2+} ion relative to the amount of PAA repeating unit was matched (i.e., the molar ratio of Ca^{2+}/PAA repeating unit = 0.2). For this condition, R_h was found to scale as $R_h \sim M^{\nu}$ (ν = 0.414), which suggests that the PAA chain has more compact conformation than the ideal chain (ν = 0.5). This is due to the condensation of divalent counterion, Ca^{2+}, at the charged sites of PAA.

Lastly, we varied the rate of crystal growth and measured $C_{crit,PAA}$. The rate of crystal growth was tuned by varying the evaporation rate, recalling that the growth of crystal was subject to the progression of evaporation. Experimentally, temperature of the evaporating droplet was adjusted with a heating apparatus while the ambient condition (22°C and 40% of relative humidity) was kept constant, so that evaporation was faster at higher temperature. Both the transition of the crystal shape and the corresponding disappearance of the XRD peaks showed that the growth inhibition was accelerated by lowering the evaporation temperature (Figure 4.11 and Figure 4.13). Therefore, $C_{crit,PAA}$ was found to increase with the evaporation temperature (T). To take into account the temperature dependence of both the change of evaporation rate and PAA diffusion coefficient, $C_{crit,PAA}$ was also plotted against temperature-dependent characteristic parameter $\eta\Delta P/T$, where η is the solvent viscosity, and ΔP is the vapor pressure difference between liquid water and ambient air, which is proportional to the rate of evaporation (Table 4.2). This characteristic parameter was found to be linearly correlated with $C_{crit,PAA}$ with good accuracy, which will be discussed further in the following section 4.1.

Table 4.2. Properties of solvents used in this study at various temperatures

Temperature (°C)	Vapor pressure of liquid water (torr)	Viscosity of mixed solvent, water/DMF (50/50 v/v) (mPa·s)
22	20	2.636
30	32	2.051
36	44	1.759
48	80	1.295

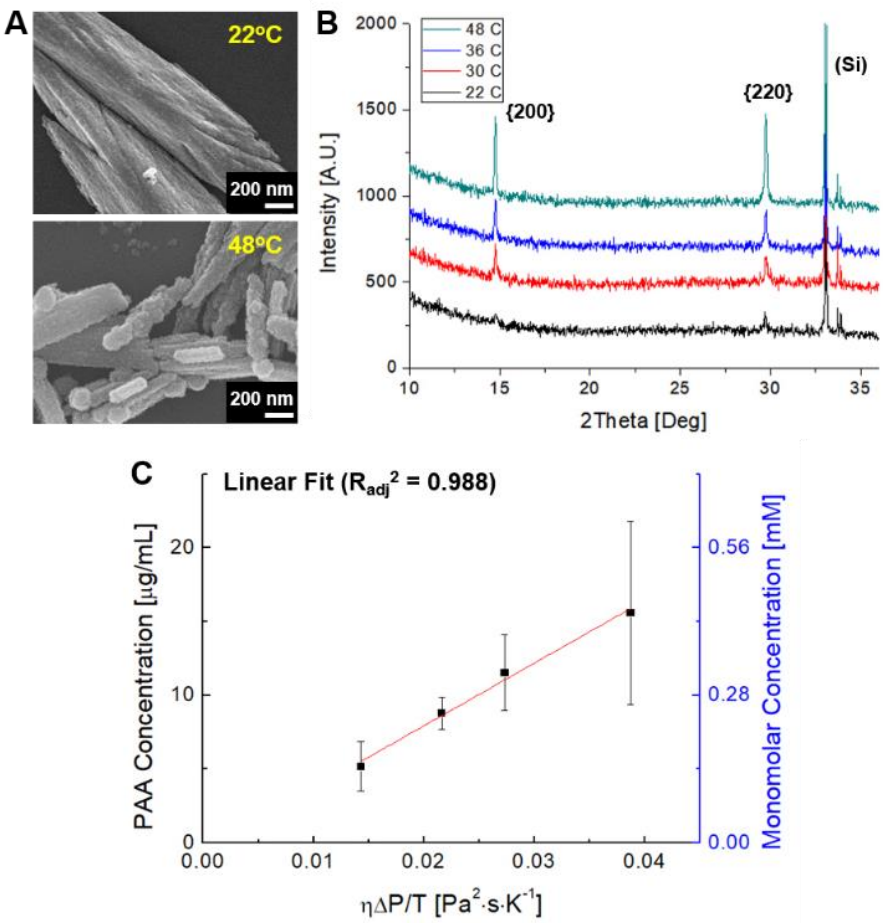

Figure 4.13. Effect of the evaporation rate on the interference of $CaSO_4$ hemihydrate crystallization by polymeric additives. (A, B) SEM and XRD analysis showed that the interference of PAA in $CaSO_4$ crystallization was stronger at lower temperature (i.e., slowly evaporating droplet). The evaporation rate was the decisive factor for the rate of crystal growth. All the samples contained 14.4 μg/mL of PAA5K. (C) Critical PAA concentrations plotted against the product of solvent viscosity (η), vapor pressure difference between liquid water and ambient air (ΔP), and inverse temperature ($1/T$). The linear fit was forced to zero.

4.3.3. Adsorption and occlusion of PS-*b*-PAA BCMs

As a counterpart of linear PAA, PS-*b*-PAA block copolymer micelles (BCMs) were used to investigate the particulate polymer/inorganic crystal hybrid system. PS-*b*-PAA BCMs are spherical, self-assembled nanoparticles with PAA brushes emanating from the PS cores. Since the PAA brushes are negatively charged, the BCMs strongly adsorb towards the polar planes of the crystals. Homogeneous incorporation of BCMs throughout the whole crystalline phase was directly observed using the SEM image of a cross-sectioned crystal (Figure 4.14), indicating that the growing crystal front encompasses the adsorbed BCMs, and eventually occludes (or encapsulates) the BCMs.[13] SEM and EDS analysis showed that both the occlusion density of BCMs and the void fraction inside the columnar crystal increase as the BCM concentration (Figure 4.14A and Figure 4.15). Consequently, the structure of individual crystal was perturbed from a single-crystalline column to a connected network of small nanocrystallites.

XRD and SAED experiments revealed consistent trend of vanishing {200} crystalline features as the amount of BCMs was increased (Figure 4.7 and Figure 4.14B). The reduction in crystallinity is an evident signature of increased defect density inside the crystals. Likewise to the case of the PAA adsorption, we defined the critical BCM number concentration ($N_{crit,BCM}$) at which the inherent crystalline peaks completely vanished. It is noted that the columnar crystal form did not change regardless of the extent of the BCM occlusion. The aspect ratios of the columnar $CaSO_4 \bullet 0.5H_2O$ crystals prepared in the presence of either PAA single chains or PS-*b*-PAA BCMs were compared (Figure 4.16). For the PAA adsorption, the aspect ratio was rapidly reduced as the PAA concentration approached the critical point. On the contrary, for the BCM incorporation, the aspect ratio was poised well above unity for the full range of

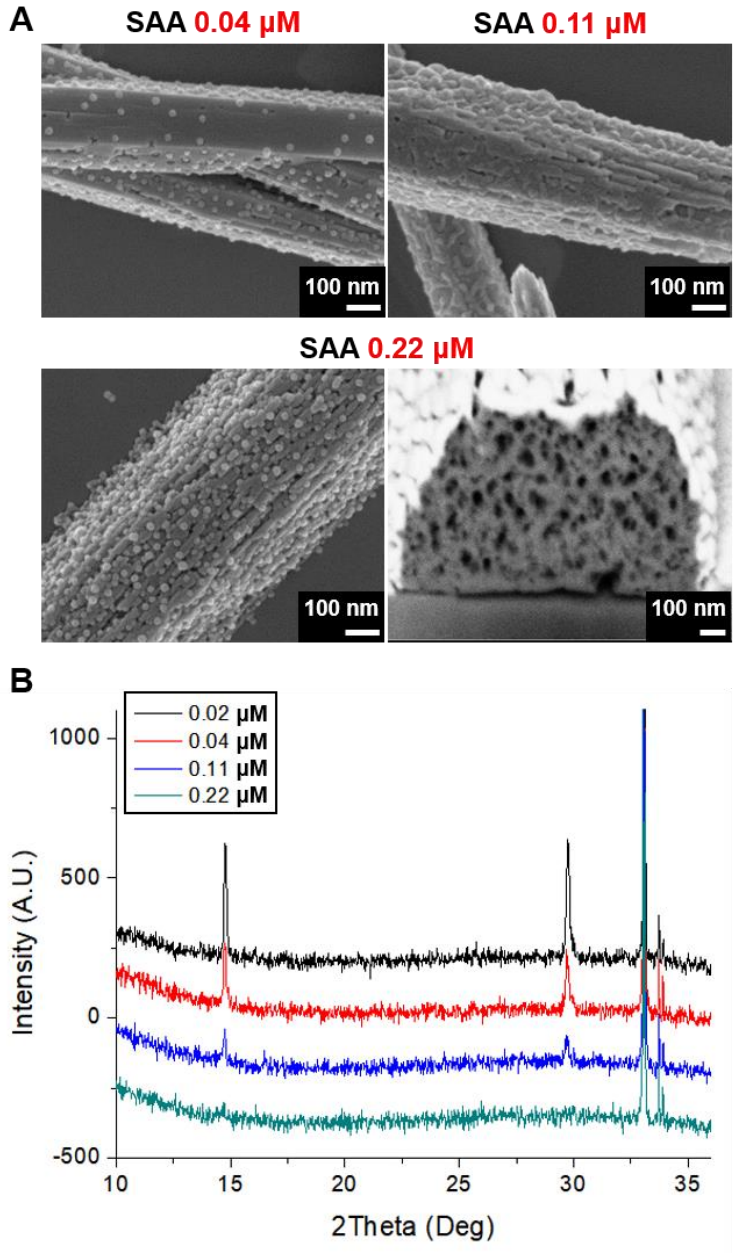

Figure 4.14. (A) $CaSO_4 \cdot 0.5H_2O$ crystallized in the presence of SAA84K BCMs with different number concentrations. Cross-section image revealed dense and homogeneous distribution of incorporated BCMs and concomitant voids within crystal prepared in the presence of SAA84K 0.22 μmol/L. (B) Corresponding XRD diffraction patterns.

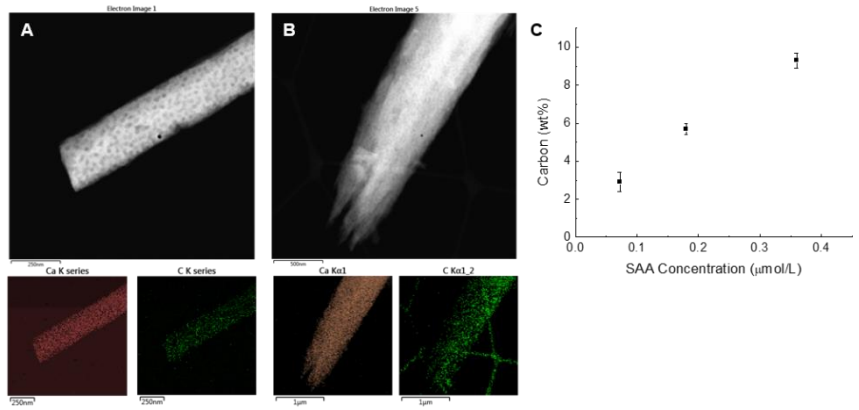

Figure 4.15. (A, B) STEM images and corresponding energy-dispersive X-ray spectroscopy (EDS) of $CaSO_4$ hemihydrate crystals in the presence of 0.07 and 0.18 μmol/L SAA19K, respectively. (C) Organic content displayed in terms of carbon weight% from the crystals obtained from different SAA19K concentrations.

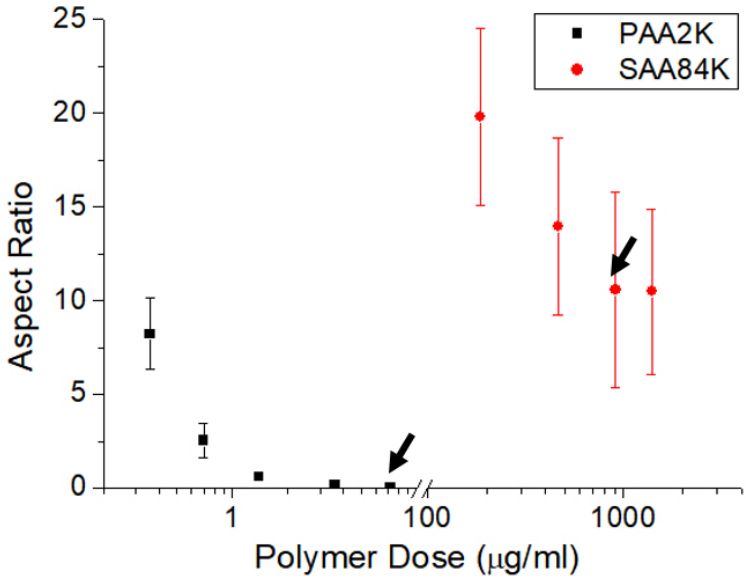

Figure 4.16. Aspect ratios of $CaSO_4$•$0.5H_2O$ crystals prepared in the presence of either PAA2K or SAA84K BCMs with different mass concentrations. Data obtained from the SEM image analysis. Arrows indicate the critical points where the inherent $CaSO_4$•$0.5H_2O$ crystalline peaks completely vanished.

BCM concentration investigated. The incorporation of BCMs did not induce the anisotropic growth retardation even above $N_{crit,BCM}$.

Figure 4.17 shows trend of $N_{crit,BCM}$ as a function of hydrodynamic radius (R_h) of BCMs measured by DLS. Detailed characteristics of BCMs such as core and hydrodynamic radii are shown in Figure 4.18. In summary, the core radii of BCMs were kept constant, while hydrodynamic radii increase using higher molecular weight of PAA block. For a given number concentration of BCMs, the incorporation of BCMs within the crystal was enhanced with the increasing order of R_h (Figure 4.19). It is interesting to note that the experimental results follow the general trend that $N_{crit,BCM}$ is inversely proportional to R_h as shown in Figure 4.17. This will be discussed in detail in the following section.

In addition, the degree of ionization (α) of PAA block for PS-*b*-PAA BCMs drastically affected the occlusion behavior, in the same manner with the adsorption of PAA single chains. When the ionization of PAA was suppressed by the addition of 0.5 equiv. HCl ($\alpha \approx 0$), Neither adsorption nor occlusion of BCMs was observed (Figure 4.20). This also signifies the electrostatic nature of the interactions between PS-*b*-PAA BCMs and the crystal surfaces, which shows good agreement with the results obtained from PAA addition.

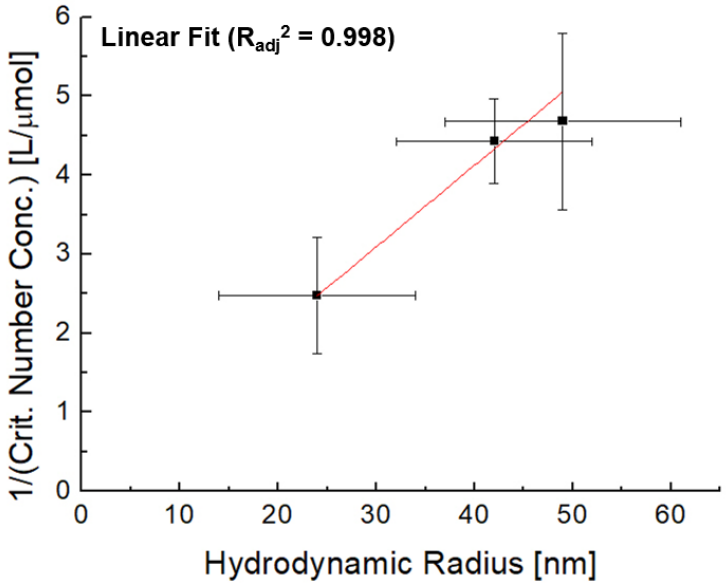

Figure 4.17. The reciprocal of critical BCM number concentrations ($1/N_{crit,BCM}$) for different hydrodynamic radii (R_h). The linear fit was forced to zero.

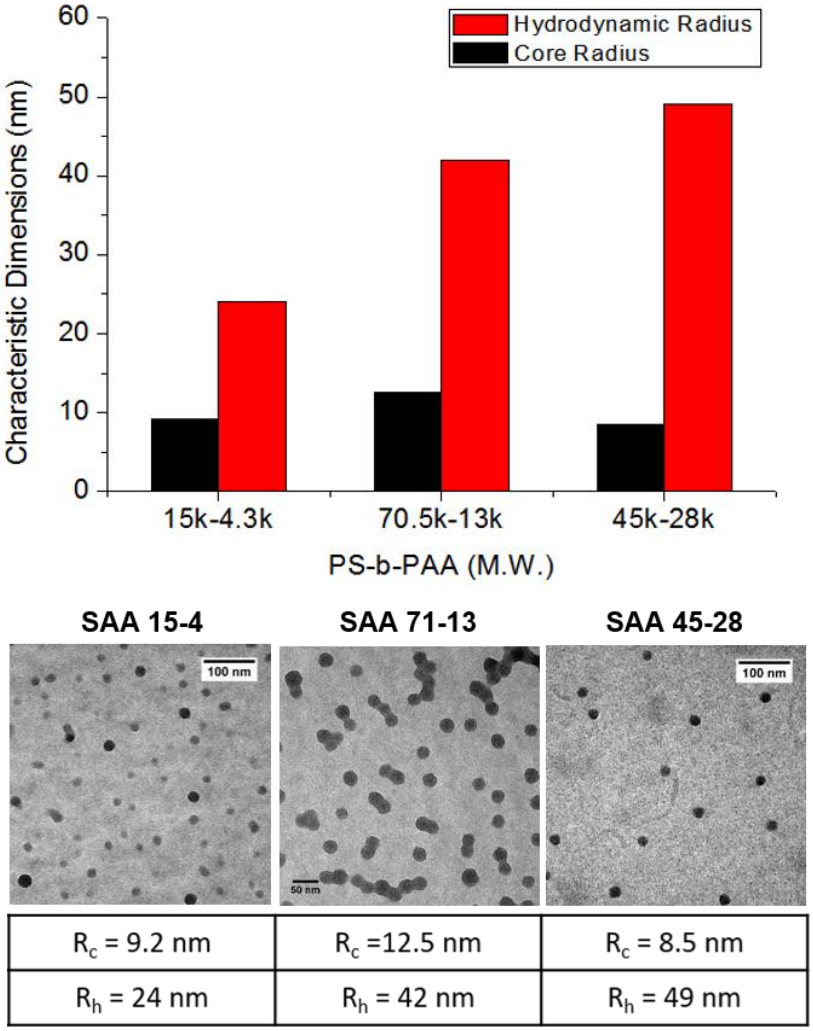

Figure 4.18. Characterization of PS-*b*-PAA BCMs. Averaged core radii (R_c) of the BCMs were determined by TEM images and hydrodynamic radii (R_h) were determined by DLS. Below diagram indicates BCMs used in this study with their PAA degrees of polymerization (DP, N_{PAA}) and core diameters. It is clear that R_h strongly depends on N_{PAA} than the size of core, which represent that stretching of PAA brush dominates R_h. Hence, R_h of the BCMs was varied while the core size was remained relatively constant.

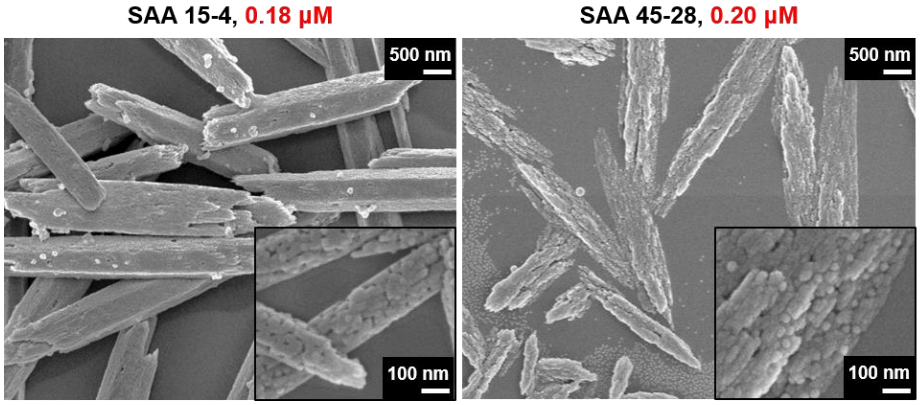

Figure 4.19. The effect of R_h of BCMs on the occlusion of the BCMs and the frustration of $CaSO_4$•$0.5H_2O$ crystallinity. (Left) SAA19K (PS_{15k}-*b*-$PAA_{4.3k}$) BCMs have the smallest R_h (~ 24 nm), thereby showing the least frustration. Contrary, SAA73K (PS_{45k}-*b*-PAA_{28k}) BCMs with the largest R_h (~ 49 nm) and showed the greatest frustration. It is noted that SAA84K ($PS_{70.5k}$-b-PAA_{13k}) BCMs have intermediate R_h (~ 42 nm), thereby the result showed an intermediate level of frustration (Figure 6 in the main text). Herein, the concentrations are BCM number-based.

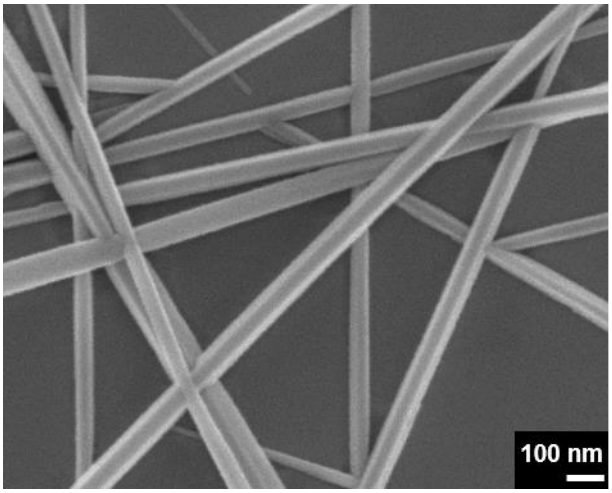

Figure 4.20. $CaSO_4 \cdot 0.5H_2O$ crystallized in the presence of SAA84K ($PS_{70.5k}$-b-PAA_{13k}) BCMs in 1 mM HCl (0.5 equiv. to the added amount PAA). 0.22 μmol/L of BCM concentration, the value same with the critical BCM concentration (i.e., the concentration where the inherent $CaSO_4 \cdot 0.5H_2O$ crystalline peaks were completely vanished) in the absence of HCl, was applied. The added HCl turned off the electrostatic interactions of BCMs with the crystal surface. As a result, the crystal habit was identical with the one prepared from the precursor solution containing only $CaSO_4$. The degrees of ionization (α) were $\alpha \approx 0$ in 1 mM HCl and $\alpha = 0.05$ in the absence of HCl.

4.4. Discussion

4.4.1. Mechanisms of diffusion-limited adsorption of PAA and PS-*b*-PAA BCMs for the retardation of crystal growth

In the previous section, we characterized the scaling relationship between $C_{\mathrm{crit,PAA}}$ and M, and $N_{crit,BCM}$ and R_{h}, for the linear polymer and particulate polymer system, respectively. Based on the assumption that the adsorption of negatively charged polyelectrolyte (PE) on the positively charged surface is irreversible (i.e., the desorption of PE is negligible), the fluxes of SO_4^{2-} and the negatively charged PEs heading for the crystal front are competitive. Thus, the crystal growth along *c*-axis can be inhibited when the flux of the PEs exceeds the critical value.[105, 106] We propose that the kinetics of crystal growth is predominantly affected by the diffusion flux of the added PEs. This is supported by the organic contents of BCM-occluded crystals, where the amount of BCM occluded in the crystal complexes increases as the micelle concentration in the initial solution increases and BCM distributes homogeneously in the crystal complexes (Figure 4.15).

Simply, the critical flux of the PEs for the inhibition of the crystal growth is assumed to be constant. The flux of the PEs in solution is proportional to diffusion coefficient, D, and the number concentration (n) of polyelectrolyte. Considering the effective area of one molecule is proportional to R_h^2, the critical flux is proportional to $Dn_{crit}R_h^2$, which is invariant to the characteristics of the PEs. The diffusion of homopolymers or polymer particles in solution is inversely proportional to their hydrodynamic radius, R_{h}, i.e., $D \sim R_{\mathrm{h}}^{-1}$. Since $R_h \sim M^v$ ($v=0.414$) for homopolymers with relatively long chains (Figure 4.9) in the nucleation condition (i.e., 50 vol% DMF), the scaling relationship can be extracted as $n_{crit} \sim D^{-1}R_h^{-2} \sim R_h^{-1}$, and especially $n_{crit,PAA} \sim R_h^{-1} \sim M^{-v}$. Conversion

of the number to the weight concentration gives $C_{crit,PAA} \sim M^{1-\nu}$, which shows good agreement with the experiments (see Figure 4.10). Also, the predicted scaling of $N_{crit,BCM}$ agrees well with the experiments (Figure 4.17).

So far, we discussed the isothermal case. However, various parameters introduced significantly depend on temperature. Firstly, $D \sim (k_bT/\eta R_h)$, where $\eta(T)$ is the viscosity of solvent. Secondly, the evaporation rate, which controls the rate of crystal growth, is proportional to the vapor pressure difference, ΔP, which also depends on temperature. It should be noted that the critical flux for inhibition would be proportional to the rate of crystal growth, since the polyelectrolyte adsorption ($\sim D n_{crit} R_h^2$) and the growth ($\sim \Delta P$) is in competition. Considering only terms relevant with temperature, we could establish a simple scaling relationship $n_{crit} \sim \Delta P(\eta/T)$. The experiments for linear PAA exactly followed this scaling, validating the competition between the crystal growth and the polyelectrolyte-induced growth inhibition (see Figure 4.13). Therefore, the diffusion-limited adsorption model successfully described the adsorption behavior of both linear- and particulate-charged macromolecules.

4.4.2. Effect of structures of macromolecular additives on the retardation of crystal growth

$CaSO_4 \bullet 0.5H_2O$ crystal shape is strikingly dependent on the absorbent such as PAA single chains and BCMs, despite of their chemical equivalence of negatively charged PEs. The strong growth inhibition of PAA on the polar surface resulted in planar or sheet-like crystal forms, while particulate BCMs did not show such growth retardation. Hence, the efficiency of growth retardation should be closely related with certain structural characteristics of macromolecules.

It is likely that the key factor is the size-exclusion, which would prevent adsorbed BCMs from occupying all growth sites on a crystal plane. In a crude assessment, BCMs could be regarded as hard-spheres, and their adsorption is irreversible, thereby the adsorption process could be considered as the random packing of spheres in a plane. The maximum area fraction of adsorption, or the jamming limit, is approximately 0.55, which suggests rather frequent exposure of unscreened surface.[107] Therefore, BCMs cannot inhibit the growth of the polar crystal surface like the single chains, since the size of BCMs is extremely large compared to the size of ions or PAA segments. It is congruent with the fact that BCMs can be occluded, that is, the crystal front can persist its propagation upon the adsorption of BCMs.

4.5. Summary

Natural hybrids utilize the combination of polyelectrolytes (e.g., proteins) and inorganic hard materials to achieve desired functionality (e.g., specific strength). From an engineering point of view, understanding the kinetic mechanism and dynamic factors is crucial for the control and/or scale-up of such hybrid assemblies. We demonstrated the shape modification of and particle incorporation within crystallizing mineral ($CaSO_4 \cdot 0.5H_2O$), enabled by electrostatic interactions of charged macromolecules (PAA) with crystal surfaces. When PAA in the form of linear chains was added in the crystallizing solution, crystals changed its habit from columnar to platelet as the PAA concentration was increased. The observed reduction in the aspect ratio is due to the preferential adsorption of PAA chains to the polar crystal surfaces. When PS-*b*-PAA BCMs were added, there was no change in the columnar habit since BCMs were not capable of the inhibition of crystal growth along the polar axis. Instead, BCMs were occluded within the crystal matrices via the cooperation of BCM adsorption and subsequent crystal growth.

We identified the diffusion-limited adsorption as the mechanism underlying the assembly of linear polyelectrolyte/inorganic hybrids. The consistency of the proposed model and experimentally determined molecular weight- and evaporation rate-dependence on the critical PAA concentration supported our rationale. Furthermore, our understanding of the dynamic adsorption could be further extended to the adsorption of charged macromolecules with other geometry such as spherical BCMs. This work would provide the basis of knowledge for the kinetic control of hybrid assembly in both biological and engineering context.

Conclusions

Self-assembly of block copolymer micelles (BCMs) have received much attention for decades because of its intriguing relationships between the polymer architecture and the resultant micellar structure and its diverse applications. This dissertation presents experimental studies on BCMs with the bottlebrush core block and the BCM-inorganic nanocomposites combined with relevant model analyses with emphasis on characterizing how the structures of BCMs and related composite materials evolve.

In Chapter 1, a brief historical background of self-assemblies of block copolymers in selective solvents is presented. Recently, the classical theories of micelle assembly have been challenged by novel types of block copolymers with complex architecture and/or functional groups. Block copolymers with bottlebrush architecture, for instance, is investigated in the present works in order to re-visit the classical arguments on BCMs and deal with their unprecedented fast relaxation. In addition, many important approaches on the utilization of BCMs have been proposed, including the bio-mimetic tough composites which is also dealt in the present study.

In Chapter 2, we present the structural impact of the bottlebrush architecture at the segregating core block on BCMs. Enhanced chain stiffness of the bottlebrush core block, owing to the steric hindrance between adjacent side-chains, induces strong stretching of chains within the core domain, leading to larger core dimensions. However, such stiffness effect is nearly omitted in the classical scaling theory, which brings significant mismatches between the

experimental scaling laws and the prediction based on the flexible core block. We could resolve the mismatches by relieving the assumption of $\nu = 0.5$ to the general case of $0.5 \leq \nu \leq 1$ and re-formulating the classical scaling theories, where ν is the Flory exponent in melts. Therefore, an accurate prediction of the correlation between the stiffness of bottlebrush core block and the micelle dimensions (i.e., the core radius and the corona thickness) is now established.

It is known that bottlebrush polymers also have faster relaxation dynamics, however, actual measurement of dynamics in self-assembled bottlebrush block copolymers has not made so far. In Chaper 3, the impact of bottlebrush architecture at the core block on the chain exchange dynamics between self-assembled domains is investigated for the first time. The bottlebrush nature of model PF polymers, such as the lack of chain entanglement and the abundance of free volume, is confirmed and further linked to the fast chain exchange within BCMs, measured using time-resolved small-angle neutron scattering (TR-SANS) technique. Kinetic comparison suggests that the bottlebrush architecture at the core block could bring several orders faster exchange dynamics than flexible core block. The works in Chapters 2–3 altogether rationalize the use of bottlebrush block copolymer with high molecular weight for rapid self-assembly of large domains, that has been proposed previsouly.

Chapter 4 demonstrates the development of BCM-inorganic nanocomposites via occlusion of the BCMs within growing crystalline material. The mechanical properties including the fracture toughness of such bio-mimetic composites rely on the spatial distribution of organic molecules and/or particles with inorganic phases, which in turn depends on the parameters of assembly process. In addition, it is important to recognize the dynamical features of occlusion-driven composites, that is, the growth of mineral phase and the adsorption of BCMs mutually affect the occlusion density in

competitive ways. Hence, we formulated a dynamic model describing such competition, through which the structural properties of BCMs (e.g., hydrodynamic radius) are linked to their effectiveness in occlusion. Multiple analyses using PS-*b*-PAA BCMs or PAA homopolymers, which interacts with $CaSO_4$ mineral through electrostatic interaction, confirm the reliability of such model.

Throughout the whole dissertation, the structures of BCMs assembled in different systems are precisely characterized and correlated to the intrinsic polymer structure and/or the hybrids formed with inorganic material. The necessary condition for establishing such correlation is that BCMs must have uniform structures, which is only viable after sufficient chain exchanges. Therefore, both the equilibrium of micellar systems and the dynamics realizing such equilibrium should be carefully considered for the control of BCMs, as the present study on the bottlebrush block copolymer BCMs serves as a good example. Then, it is expected that utilization of BCMs as cheap, functional, and conveniently produced building blocks will have great potentials in designing sophisticated hybrids or hierarcical self-assemblies.

Bibliography

[1] J.-F. Lutz, *Sequence-controlled polymers : synthesis, self-assembly, and properties* (ACS symposium series, no. 1170). Washington, DC: American Chemical Society, 2014.

[2] I. W. Hamley, *The physics of block copolymers* (Oxford science publications). Oxford ; New York: Oxford University Press, 1998.

[3] E. B. Zhulina and O. V. Borisov, *Macromolecules* 2012, **45**, 4429-4440.

[4] I. W. Hamley, *Block copolymers in solution : fundamentals and applications*. Chichester, England Hoboken, NJ: Wiley, 2005.

[5] P.-G. De Gennes, *Solid State Phys., Suppl.* 1978, **14**, 1-18.

[6] M. Daoud and J. P. Cotton, *Journal De Physique* 1982, **43**, 531-538.

[7] A. Halperin, *Macromolecules* 1987, **20**, 2943-2946.

[8] E. B. Zhulina, M. Adam, I. LaRue, S. S. Sheiko, and M. Rubinstein, *Macromolecules* 2005, **38**, 5330-5351.

[9] R. Nagarajan and K. Ganesh, *Journal of Chemical Physics* 1989, **90**, 5843-5856.

[10] R. Verduzco, X. Y. Li, S. L. Peseka, and G. E. Stein, *Chemical Society Reviews* 2015, **44**, 2405-2420.

[11] T. P. Lodge, M. A. Hillmyer, Z. L. Zhou, and Y. Talmon, *Macromolecules* 2004, **37**, 6680-6682.

[12] W. F. Edmonds, Z. B. Li, M. A. Hillmyer, and T. P. Lodge, *Macromolecules* 2006, **39**, 4526-4530.

[13] K. R. Cho *et al.*, *Nature Communications* 2016, **7**.

[14] D. C. Pozzo and L. M. Walker, *Colloids and Surfaces A: Physicochemical and Engineering Aspects* 2007, **294**, 117-129.

[15] Y. Y. Kim *et al.*, *Nat Mater* 2011, **10**, 890-6.

[16] G. M. Miyake, R. A. Weitekamp, V. A. Piunova, and R. H. Grubbs, *Journal of the American Chemical Society* 2012, **134**, 14249-14254.

[17] D. P. Song, C. Li, W. H. Li, and J. J. Watkins, *Acs Nano* 2016, **10**, 1216-1223.

[18] A. Subbotin, M. Saariaho, O. Ikkala, and G. ten Brinke, *Macromolecules* 2000, **33**, 3447-3452.

[19] H.-P. Hsu, W. Paul, S. Rathgeber, and K. Binder, *Macromolecules* 2010, **43**, 1592-1601.

[20] S. L. Pesek, X. Li, B. Hammouda, K. Hong, and R. Verduzco, *Macromolecules* 2013, **46**, 6998-7005.
[21] W. Y. Gu *et al.*, *Acs Nano* 2013, **7**, 2551-2558.
[22] J. Rzayev, *Macromolecules* 2009, **42**, 2135-2141.
[23] T. P. Lin, A. B. Chang, S. X. Luo, H. Y. Chen, B. Lee, and R. H. Grubbs, *ACS Nano* 2017, **11**, 11632-11641.
[24] M. Pitsikalis, E. Siakali-Kioulafa, and N. Hadjichristidis, *Journal of Polymer Science Part a-Polymer Chemistry* 2004, **42**, 4177-4188.
[25] G. Cheng *et al.*, *Macromolecules* 2008, **41**, 4824-4827.
[26] M. Alaboalirat *et al.*, *Macromolecules* 2018, **52**, 465-476.
[27] M. Zamurovic, S. Christodoulou, A. Vazaios, E. Iatrou, M. Pitsikalis, and N. Hadjichristidis, *Macromolecules* 2007, **40**, 5835-5849.
[28] Z. Li, J. Ma, C. Cheng, K. Zhang, and K. L. Wooley, *Macromolecules* 2010, **43**, 1182-1184.
[29] R. Fenyves, M. Schmutz, I. J. Horner, F. V. Bright, and J. Rzayev, *Journal of the American Chemical Society* 2014, **136**, 7762-7770.
[30] A. N. Semenov, I. A. Nyrkova, and A. R. Khokhlov, *Macromolecules* 1995, **28**, 7491-7500.
[31] V. Castelletto, I. W. Hamley, and J. S. Pedersen, *Journal of Chemical Physics* 2002, **117**, 8124-8129.
[32] A. Halperin and S. Alexander, *Macromolecules* 1989, **22**, 2403-2412.
[33] S. H. Choi, T. P. Lodge, and F. S. Bates, *Phys Rev Lett* 2010, **104**, 047802.
[34] S. Jain and F. S. Bates, *Macromolecules* 2004, **37**, 1511-1523.
[35] S. Kim, J. Choi, J. H. Kim, S.-H. Choi, and K. Char, 2020.
[36] Y. C. Ma and T. P. Lodge, *Macromolecules* 2016, **49**, 3639-3646.
[37] M. D. Whitmore and J. Noolandi, *Macromolecules* 1985, **18**, 657-665.
[38] G. Hougham, *Fluoropolymers* (Topics in applied chemistry). New York: Kluwer Academic/Plenum, 1999.
[39] P. Lo Nostro and S. H. Chen, *The Journal of Physical Chemistry* 1993, **97**, 6535-6540.
[40] S. J. Dalsin, T. G. Rions-Maehren, M. D. Beam, F. S. Bates, M. A. Hillmyer, and M. W. Matsen, *Acs Nano* 2015, **9**, 12233-12245.
[41] M. E. Seitz, W. R. Burghardt, and K. R. Shull, *Macromolecules* 2009, **42**, 9133-9140.
[42] P. E. Theodorakis, H. P. Hsu, W. Paul, and K. Binder, *J Chem Phys* 2011, **135**, 164903.
[43] J. Noolandi and K. M. Hong, *Macromolecules* 1983, **16**, 1443-1448.

[44] A. W. Qin, M. M. Tian, C. Ramireddy, S. E. Webber, P. Munk, and Z. Tuzar, *Macromolecules* 1994, **27**, 120-126.

[45] S. Forster, M. Zisenis, E. Wenz, and M. Antonietti, *Journal of Chemical Physics* 1996, **104**, 9956-9970.

[46] R. Lund, L. Willner, and D. Richter, *Controlled Polymerization and Polymeric Structures: Flow Microreactor Polymerization, Micelles Kinetics, Polypeptide Ordering, Light Emitting Nanostructures* 2013, **259**, 51-158.

[47] H. Yokoyama and E. J. Kramer, *Macromolecules* 1998, **31**, 7871-7876.

[48] M. Hu, Y. Xia, G. B. McKenna, J. A. Kornfield, and R. H. Grubbs, *Macromolecules* 2011, **44**, 6935-6943.

[49] S. J. Dalsin, M. A. Hillmyer, and F. S. Bates, *ACS Macro Letters* 2014, **3**, 423-427.

[50] C. R. López-Barrón, P. Brant, A. P. R. Eberle, and D. J. Crowther, *Journal of Rheology* 2015, **59**, 865-883.

[51] B. R. Sveinbjornsson, R. A. Weitekamp, G. M. Miyake, Y. Xia, H. A. Atwater, and R. H. Grubbs, *Proceedings of the National Academy of Sciences of the United States of America* 2012, **109**, 14332-14336.

[52] Y. Cho, Y. Kim, T.-L. Choi, J. Lim, and K. Char, *Polymer Chemistry* 2018, **9**, 3536-3542.

[53] J. Lim *et al.*, *Chem Commun (Camb)* 2016, **52**, 2485-8.

[54] I. N. Haugan *et al.*, *Acs Macro Letters* 2018, **7**, 525-530.

[55] K. Honda, M. Morita, H. Otsuka, and A. Takahara, *Macromolecules* 2005, **38**, 5699-5705.

[56] S. Wu, *Macromolecules* 1985, **18**, 2023-2030.

[57] J. D. Ferry, *Viscoelastic properties of polymers*, 3d ed. New York: Wiley, 1980, pp. xxiv, 641 p.

[58] B. Pulamagatta, S. Pankaj, M. Beiner, and W. H. Binder, *Macromolecules* 2011, **44**, 958-965.

[59] D. Schaeffel *et al.*, *Acs Macro Letters* 2014, **3**, 428-432.

[60] S.-H. Choi, F. S. Bates, and T. P. Lodge, *Macromolecules* 2011, **44**, 3594-3604.

[61] T. Zinn, L. Willner, V. Pipich, D. Richter, and R. Lund, *Acs Macro Letters* 2016, **5**, 884-888.

[62] L. Willner, A. Poppe, J. Allgaier, M. Monkenbusch, and D. Richter, *Europhysics Letters* 2001, **55**, 667-673.

[63] T. Zinn, L. Willner, R. Lund, V. Pipich, and D. Richter, *Soft Matter* 2012, **8**, 623-626.

[64] R. Lund, L. Willner, J. Stellbrink, P. Lindner, and D. Richter, *Phys Rev Lett* 2006, **96**, 068302.

[65] P. E. Rouse, *Journal of Chemical Physics* 1953, **21**, 1272-1280.
[66] K. A. Cavicchi and T. P. Lodge, *Macromolecules* 2003, **36**, 7158-7164.
[67] K. A. Mauritz, R. F. Storey, and S. E. George, *Macromolecules* 1990, **23**, 441-450.
[68] Y. Ma and T. P. Lodge, *Macromolecules* 2016, **49**, 9542-9552.
[69] U. G. Wegst, H. Bai, E. Saiz, A. P. Tomsia, and R. O. Ritchie, *Nat Mater* 2015, **14**, 23-36.
[70] A. Veis and J. R. Dorvee, *Calcif Tissue Int* 2013, **93**, 307-15.
[71] A. Linde and T. Lundgren, *International Journal of Developmental Biology* 1995, **39**, 213-222.
[72] G. He *et al.*, *J Biol Chem* 2005, **280**, 33109-14.
[73] F. Nudelman *et al.*, *Nat Mater* 2010, **9**, 1004-9.
[74] F. Nudelman, A. J. Lausch, N. A. Sommerdijk, and E. D. Sone, *J Struct Biol* 2013, **183**, 258-69.
[75] T. Kato, A. Sugawara, and N. Hosoda, *Advanced Materials* 2002, **14**, 869-877.
[76] S. H. Yu and H. Colfen, *Journal of Materials Chemistry* 2004, **14**, 2124-2147.
[77] T. X. Wang, H. Colfen, and M. Antonietti, *Journal of the American Chemical Society* 2005, **127**, 3246-3247.
[78] B. Yeom and K. Char, *Journal of Crystal Growth* 2016, **443**, 31-37.
[79] M. Oner, O. Dogan, and G. Oner, *Journal of Crystal Growth* 1998, **186**, 427-437.
[80] A. Tsortos and G. H. Nancollas, *J Colloid Interface Sci* 2002, **250**, 159-67.
[81] H. Colfen and S. Mann, *Angewandte Chemie-International Edition* 2003, **42**, 2350-2365.
[82] T. P. Wang, M. Antonietti, and H. Colfen, *Chemistry-a European Journal* 2006, **12**, 5722-5730.
[83] J. W. Shen, C. L. Li, N. F. A. van der Vegt, and C. Peter, *Journal of Physical Chemistry C* 2013, **117**, 6904-6913.
[84] Y. W. Wang and F. C. Meldrum, *Journal of Materials Chemistry* 2012, **22**, 22055-22062.
[85] M. G. Lioliou, C. A. Paraskeva, P. G. Koutsoukos, and A. C. Payatakes, *Journal of Colloid and Interface Science* 2006, **303**, 164-170.
[86] I. D. R. M.C Cafe, *Journal of Colloid and Interface Science* 1982.
[87] M. C. Vanderleeden and G. M. Vanrosmalen, *Journal of Colloid and Interface Science* 1995.
[88] E. Seyrek, J. Hierrezuelo, A. Sadeghpour, I. Szilagyi, and M. Borkovec, *Physical Chemistry Chemical Physics* 2011, **13**, 12716-12719.
[89] S. Weiner and L. Addadi, *Journal of Materials Chemistry* 1997, **7**, 689-702.

[90] Y. Y. Kim, L. Ribeiro, F. Maillot, O. Ward, S. J. Eichhorn, and F. C. Meldrum, *Advanced Materials* 2010, **22**, 2082-+.

[91] Y. Y. Kim *et al.*, *Advanced Functional Materials* 2016, **26**, 1382-1392.

[92] B. Kowalczyk *et al.*, *Nature Materials* 2012, **11**, 227-232.

[93] Y. Ning, L. A. Fielding, T. S. Andrews, D. J. Growney, and S. P. Armes, *Nanoscale* 2015, **7**, 6691-6702.

[94] F. Li *et al.*, *Journal of Crystal Growth* 2013, **374**, 31-36.

[95] Q. S. Chen, G. M. Jiang, C. Y. Jia, H. Wang, and B. H. Guan, *Crystengcomm* 2015, **17**, 8549-8554.

[96] M. V. Thomas and D. A. Puleo, *Journal of Biomedical Materials Research Part B-Applied Biomaterials* 2009, **88b**, 597-610.

[97] J. Cho, J. K. Hong, K. Char, and F. Caruso, *Journal of the American Chemical Society* 2006, **128**, 9935-9942.

[98] R. Matmour *et al.*, *Macromolecules* 2005, **38**, 5459-5467.

[99] Y. S. Yu and A. Eisenberg, *Journal of the American Chemical Society* 1997, **119**, 8383-8384.

[100] D. C. Harris, *Quantitative chemical analysis*, 8th ed. New York: W.H. Freeman and Co., 2010.

[101] R. D. Deegan, O. Bakajin, T. F. Dupont, G. Huber, S. R. Nagel, and T. A. Witten, *Nature* 1997, **389**, 827-829.

[102] M. Byun, N. B. Bowden, and Z. Q. Lin, *Nano Letters* 2010, **10**, 3111-3117.

[103] N. Shahidzadeh, M. F. L. Schut, J. Desarnaud, M. Prat, and D. Bonn, *Scientific Reports* 2015, **5**.

[104] U. Tritschler, M. Kellermeier, C. Debus, A. Kempter, and H. Colfen, *Crystengcomm* 2015, **17**, 3772-3776.

[105] X. Li, O. Niitsoo, and A. Couzis, *Journal of Colloid and Interface Science* 2014, **420**, 50-56.

[106] I. Szilagyi, G. Trefalt, A. Tiraferri, P. Maroni, and M. Borkovec, *Soft Matter* 2014, **10**, 2479-2502.

[107] J. W. Evans, *Reviews of Modern Physics* 1993, **65**, 1281-1329.

요약 (국문초록)

지난 수십 년간의 기초 연구를 통해 블록공중합체 마이셀(Block copolymer micelle; BCM)의 자기조립에 대한 이해가 증진되어 왔으나, 새롭게 디자인된 블록공중합체를 이용한 최근의 연구 사례들은 기존의 이론으로 설명되지 않는 구조적 및 동역학적 특성을 지니는 BCM 을 선보이고 있다. 한편, 자연계에서 발견되는 단백질-무기질 복합체를 본 따, 우수한 물성을 갖는 조합체나 나노복합체를 구현하기 위해 BCM 을 이용하는 연구 역시 활발히 진행되고 있다. 따라서, BCM 자기조립 현상에 대한 지식과 마이셀 유래 조합체의 형성원리 간의 연관성을 깊이 있게 이해하는 것이 중요하게 되었다. 본 학위논문에서는 블록공중합체의 독특한 분자모티프가 자기조립된 마이셀의 구조와 동역학에 미치는 영향 및 BCM 과 무기질 간의 상호작용에 의한 조합구조의 예시를 다룬다. 이러한 연구들을 관통하여, 정확히 제어된 나노소재를 위해 BCM 의 구조변화에 대한 지식을 활용하는 것의 중요성을 강조하고자 한다.

본 학위논문의 첫 부분에서는 한 쪽 블록에 긴 플루오르알킬 곁사슬이 달린 이중블록공중합체의 마이셀 구조와 완화 동역학을 소개한다. 플루오르알킬 곁가지에 의한 “병솔(Bottlebrush)” 형 사슬구조는 블록에 상당한 사슬 경도(Stiffness)를 수반하며, 블록공중합체 자기조립을 통해 불용성 용매 상에서 구형 마이셀의 내핵을 이룰 때의 플루오르알킬 사슬은 그 경도로 인해 강하게 신장(Stretching)된다. 또한, 플루오르알킬 사슬의 길이에 따른 마이셀의 내핵과 코로나(Corona) 크기의 스케일링 관계식은 고전적인 열역학적 이론에서 벗어난 것으로 관찰되며, 이러한 비전형성은 불용

성 병솔형 블록의 사슬 경도로부터 유래하였다. 병솔형 사슬구조의 사슬 경도로부터 유래하는 또 다른 결과는 사슬 얽힘(Entanglement)이 거의 없고 자유부피(Free volume)가 크다는 점인데, 이로 인해 병솔형 사슬은 선형 사슬에 비해 신속한 동역학적 특성을 보이며 내핵 내부에서의 완화(Relaxation) 역시 빠르다. 따라서, 본 병솔형 블록공중합체 시스템의 평형 이동 시간은 매우 신속하여 짧은 시간 안에 균일한 BCM 을 제작할 수 있다. 단차맞춤(Contrast-matched) 소각 중성자 산란기법을 이용해 완화 동역학을 정량적으로 측정한 결과, 실제로 병솔형 사슬이 내핵을 이루는 BCM 의 사슬 교환이 빠름을 확인하였다. 이를 통해, 병솔형 사슬이 내핵을 이루는 자기조립체는 그 구조적 거동과 완화 동역학이 신축성 있는 선형 블록공중합체의 그것과 매우 상이함을 확인하였다.

두 번째 부분에서는 BCM을 수반한 조합구조의 예시로 BCM과 광물(Mineral) 결정의 자연모사 나노복합체를 소개한다. BCM 은 정전기적 상호작용을 통해 무기질의 표면에 흡착하며, 흡착된 BCM 은 나아가 성장하는 광물 결정 내부에 함입될 수 있고, 이렇게 유기질이 함입된 광물은 함입 밀도에 따라 파쇄강도(Fracture Toughness)가 증강된다. BCM 의 코로나 전하 밀도에 의해 BCM 흡착 세기가 달라지는 한편, BCM 의 브라운확산은 성장 중인 광물 결정과의 충돌빈도에 영향을 미친다. 따라서, pH 와 BCM 의 수동역학적(Hydrodynamic) 크기를 조절함에 따라, 결정은 흡착 밀도가 증가하는 순서대로 (1) 방해받지 않는 상태의 성장과 (2) 성장지점의 부분적인 봉쇄와 그로 인한 함입을 거쳐 (3) 완전한 성장 억제를 겪는다. 이러한 연구 결과는, 정밀한 구조 제어를 거친 BCM 을 다

층적 조합구조를 만들기 위한 단위소재로 활용할 수 있으며, 이를 통해 전례 없는 물성을 지니는 나노소재를 구현할 수 있음을 시사한다.

주요어 : 블록공중합체 마이셀 • 사슬 구조 • 완화 동역학 • 마이셀 흡착 • 마이셀-무기질 조합체

학번 : 2014-21582

감사의 글

지능형 유도조합체 연구단, 그리고 서울대학교 화학생물공학부에서 열정적으로 연구하고 또 성공적으로 박사학위를 마치는 것은 많은 분들의 도움과 지원이 아니었다면 불가능했을 것입니다. 연구실과 학교를 비롯한 수많은 유/무형의 제반 지원이 있었기에 그동안 큰 장벽에 부딪히지 않고 원하는 공부를 할 수 있었다는 것을 잘 알고 있습니다. 도움을 주신 모든 분들과 관계기관에 감사를 표하고 싶으나, 글이 너무 방대해지지 않도록 가장 중요한 도움을 주셨던 분들에 한해 감사의 말을 담습니다.

먼저, 독립적 연구자가 될 수 있도록 6 년 간의 석박사과정 동안 저를 지도해주신 차국헌 교수님께 감사드립니다. 선생님께서 가르쳐주신 지식과 통찰, 그리고 조언을 통해 '연구자됨'을 배웠습니다. 연구를 진행해오며 제가 풀고자 했던 문제의 열쇠를 오래 전 선생님께서 박사과정 때 쓰신 논문에서 찾게 된 어느 날, 저는 현재의 선생님뿐 아니라 과거의 선생님으로부터도 배우고 있다는 사실을 깨달았습니다. 더불어, 지도교수님 만큼이나 풍부한 지도를 해주시고 저를 아껴주신 최수형 교수님께 감사드립니다. 논문을 작성하면서 교수님께로부터 '논문을 쓴다는 것'에 대해 배운 점이 너무나 소중합니다. 이제 졸업을 하지만, 미래에도 두 분께 '학자로서의 삶'에 대해 여전히 배울 것이 많습니다.

알찬 수업으로 지식을 배우는 즐거움을 알게 해주셨고, 이번 제 박사학위 논문심사에도 심사위원으로 흔쾌히 참여해주신 장정식 교수님, 이원보 교수님, 손정곤 박사님께 감사드립니다. 선생님들께서 귀중한 조언을 해주신 덕분에 부끄럽지 않은 학위논문이 될 수 있었습니다. 그리고 연구실에 박사후연구원으로 계셨을 때부터

지금까지 건설적인 논의와 도움, 공동연구의 기회를 주신 임지우 교수님께도 감사드립니다.

석박사과정 기간을 저와 함께 동고동락하며 많은 힘이 되었던 입학 동기 윤찬 형, 영걸 형, 상우, 윤식, 동효에게 감사드립니다. 함께 낮밤을 가리지 않고 치열하게 연구하면서 토론과 격려를 서로 나눴던 제원이에게 큰 고마움을 전하고 싶습니다. 처음 연구실에 들어와 적응하는 동안 연구적인 어려움에 부딪힐 때마다 조언을 아끼지 않고 주신 의태 형을 비롯한 연구실 선배들께 감사드립니다.

그리고 짧은 기간이나마 인턴으로 연구실에 들어와 함께 일했던 승현, 지윤, 지현, 태근, 승욱에게도 감사를 전합니다. 연구실에서는 제가 선배로서 가르치는 입장이었지만, 언제나 여러분들로부터 거꾸로 배우는 것이 가르치는 것보다 많았습니다. 그 외의 연구단의 모든 선후배 동료와 공동연구로 인연을 맺은 분들을 각각 호명하며 감사의 마음을 표하고 싶으나, 지면상 제약으로 인해 여기서 줄이는 점 양해 바랍니다.

항상 아낌없이 저를 격려해주며, (연구 외적인) 삶의 소중한 것들을 보게 해주는 솜이에게 깊은 감사를 전합니다. 마지막으로, 생업의 고단함 속에서도 저를 언제나 지지해주시고 사랑해주시는 부모님께는 어떠한 말로도 감사함을 모두 표현할 수 없을 것 같습니다. 어머니 아버지, 사랑합니다. 언급한 모든 분들에 대한 감사함을 평생토록 잊지 않으며, 정직과 학문적 기여를 신념으로 삼는 연구자의 길을 걸어가겠습니다.

2020 년 7 월, 김세영 드림.